UNIVERSIY OF BASILICATA
MATERA

Doctor of Philosophy (Ph.D.)
In

"Cities and Landscapes: Architecture, Archeology, Cultural Heritage, History and Resources"

Cycle XXXV

THESIS TITLE

"Novel Satellite-Based Methodologies for Multi-Sensor and Multi-Scale Environmental Monitoring to Preserve Natural Capital"

Disciplinary Scientific Sector: ***ICAR/03***

Ph.D. Coordinator
Prof. Antonella Guida

Doctorate
Dr. Farid Faridani Bardaskan

Supervisor
Prof. Rosa Lasaponara

Academic Year 2022/2023

Contents

Preface

Natural capital (NC) through ecosystem process provides ecosystem services that are vital and critical to the functioning of the Earth's life-support system, as (but not only) air and water, fertile soil, pollination, hazard protection. The concept of NC and associated ecosystem services reflects a recognition that environmental systems play a fundamental role not only for providing resources and services but also contributing to economic outputs and social well-being. The biophysical evaluation of the ecosystem then leads directly to the ecological and monetary evaluation since it depends on its state of conservation. Nevertheless, if from one hand, any form of vegetation cover (cropland, grassland, forest, etc.) provides numerous ecosystem services, on the other hand, the estimation of the status and trends of natural capital poses critical challenges due to the diversity of environmental assets, stocks and flows. Moreover, it is widely recognized that today climate change and anthropogenic pressures do alter major geophysical conditions and adversely affect NC and ecosystem services accelerating their depletion. NC assets are limited and vulnerable and irreversibility environmental changes may make it impossible to replace the natural capital assets that must be preserved, and this requires its constant assessment and systematic monitoring.

A recent report by the European Environmental Agency (EEA) underlined the importance of Earth Observation (EO) data for the monitoring and accounting of the natural capital to support political decisions especially for the most critical environment conditions. In this field, the potential of Remote Sensing (RS) and EO technologies, and the advancement of satellite data acquisition and processing systems, has been understood and used by researchers to create research and/or public benefit work.

The use of EO-based indicators is particularly relevant for environmental monitoring because RS-derived data have been shown to be useful across many fields, at different temporal and spatial scales from global down to a local level using open data and tools from NASA and ESA acquired systematically and available a for the whole globe. Moreover, the fast increasing developments of the Earth Observation (EO) and Information and Communication Technologies (ICT), including cloud-based resources, strongly facilitate and support the massive increase of the use of satellite data for change detection and vegetation monitoring including risk analyses. Cloud-based computing system provides ready-to-use and up-to-date datasets along with impressive computing power without having the need to download and locally store large amounts of data.

Google Earth Engine (GEE) represents a useful tool for the scientific community in applications aimed at prevention and registration of risk, and at damage and impact assessment, through the Remote Sensing techniques. GEE is an open source tool made available by Google through registration. It is a portal that allows to consult and work simultaneously with dozens and dozens of different datasets for a collection of over forty years of data on a global scale. GEE is a powerful high-performance computing tool, it is accessed and controlled through a web-based accessible application programming interface (API) and there is an associated web-based interactive development environment (IDE) that allows quick prototyping and visualization of results. Available datasets include satellite data acquired by several missions, such as: i. MODIS (Moderate Resolution Imaging Spectrometer); ii. ALOS (Advanced Land Observing Satellite); iii. Landsat series; iv. Sentinels etc. These are complemented by other useful/ancillary data, such as: i. DTMs (Digital Terrain Models); ii. shapefiles; iii. meteorological data; iv. Land Cover etc. GEE, in addition to making operations with several types of sensors extremely easy, allows the same way and time to work with petabytes of data and has changed the concept of work and analysis in the field of Remote Sensing, and to the big-data approach to the issues. GEE in recent years (2011 to date) has been widely and successfully used in many of the disciplines involving Remote Sensing (RS) and Earth Observation (EO) techniques due to its potential.

The number of papers about GEE in recent years has increased exponentially on several fields, such as: i. Forest and Vegetation; ii. Land use and Land Cover; iii. Hydrology; iv. Ecosystems and Sustainability; v. Agriculture; vi. Geoscience; vii. Cloud Computing; viii. Climate; ix. Urban Sprawl; x. Disease; xi. Hazards; xii. Cultural Heritage. The use of GEE has allowed multiple tools to be created and shared for free. Some examples can be found on the GEE website.

The following study was conducted aiming at to gather state-of-the-art remote sensing and/or earth observation techniques and to further the knowledge concerned with any aspect of the use of remote sensing and/or big data in the field of geospatial analysis. Google Earth Engine alongside different physical and statistical methods have been herein used to monitor several environmental parameters in several study areas located in Italy and Iran where there were different types of NC assets affected in recent years by natural and anthropogenic events such as fires and floods etc.

Chapter (1): Flood monitoring

Part 1. Estimating flood characteristics using satellite digital elevation models

1.1.1. Introduction

Floods are among the most disastrous events in the world and problems associated with them have increased greatly [1]. As a consequence, there is a need for effective modeling of extremely large spatial scale problems (i.e. large extent, fine grid resolution, or a large number of simulations) to understand the problem and reduce the catastrophic damages [2]. In order to obtain the floodplain maps, the Shallow Water Equations (SWEs) are generally solved via physically based two-dimensional flood models. 2D models with better performance have been developed by reducing the complexity through approximating or neglecting less significant terms of the SWEs (e.g. [3,4]). Even in their reduced complexity, Solving the SWEs is still computationally intensive due to the complex mathematical formulae [5].

Some studies in recent years focused on developing simple 2D flood models using the Cellular Automata (CA), which offers a method for modelling complicated physical systems using simple operations. In comparison with a physically based models, the simplification of a CA model can decrease the computational load [6]. To simulate a flood event by a CA model, it is necessary to divide the studied space into a set of cells with a specific geometric shape, as well as to determine the initial state of water height in each cell. By knowing the previous state of each cell and the state of the cells in its local neighborhood, the water level in that cell at each time step can be determined with a number of transition rules based on simple operators [7].

Dottori and Todini [8,9] developed a CA model based on storage cell models that uses the Manning formula to calculate interfacial discharges. Instead of solving the Manning's equation, Gimire et al. [10] developed the Cellular Automata Dual-DraInagE Simulation (CADDIES) 2D model that estimates the volume transferred between cells using a ranking system. In the next step, Guidolin et al. [5] presented the WCA2D model, which includes a weight-based system to simplify the transition rules of the CADDIES-2D model. Complex computations in the WCA2D model are minimized and this feature makes the WCA2D model suitable for real-time and/or largescale studies. Their results showed that the CADDIES-2D model can simulate flow depth and velocity eight times faster with reasonably good agreement with the standard floodplain maps. The standard flood map refers to the extents of a flood event with a certain return period which has been obtained based on common hydraulic models and field surveys for a small portion of the study area, and helps to calibrate the flood models [11]. Different studies [12-14] have used the CADDIES-2D model and reported good results in improving the 2D simulation of urban and coastal flooding, rapid flood routing, and flood risk assessment.

In less developed countries where sufficient computational power and observational data (hydrologic, hydraulic, topographic etc.) are not available, flood modeling requires even more simplified and less data-demanding methods. Recently, methods which rely on basin morphologic features have received a significant interest due to increased availability of new Digital Elevation Models (DEMs). Fluvial geomorphology is basically shaped by floods and in return the characteristics of the floods are affected by the morphological feature of the rivers [11,15]. Manfreda et al. [16] used this assumption and suggested a modified version of the Topographic Index (TI) developed by Beven and Kirkby [17] to detect flood hazard exposure using a TIm higher than a given threshold (τ). According to Manfreda et al. [18], running the linear binary classification on the morphologic descriptors can effectively detect floodplain areas with simple requirements including a standard flood map over a small section of the basin area.

Depending on the hydro-climatic conditions, river hydraulic regime, topography and in-situ measurements in a basin, several geomorphic indices have been introduced by researchers for the delineation of flood plains around the world [1,18-21]. Considering this extensive research, the classifications done by the Geomorphic Flood Index (GFI) outperforms other geomorphic indices in terms of higher accuracy and lower sensitivity to the input data; specially the return period, the type of DEM and standard flood maps, and the size of sub-basin envisaged for the calibration [21,22].

Samela et al. [22] developed the Geomorphologic Flood Assessment (GFA) tool in QGIS software which delineates the river extents based on the GFI method, DEM and the standard flood risk map of a basin.

This paper presents an innovative procedure for delineating flood maps in places which may lack detailed data and financially cannot support costly methodologies based on geomorphic methods and remote sensing data. The performance of GFI model in estimating flood extent and depth has been calibrated and evaluated with

CADDIES-2D hydraulic model in three basins in Iran with a 100-year return period. Moreover, the GFI model has been improved by introducing a constraint for the maximum hydrologically contributing area of a basin using the novel concept of Intensity-Duration-Frequency-Area (IDFA) curves.

1.1.2. Methodology

In order to calibrate and validate the performance of GFI model in estimating flood plain extent and depth, first the CADDIES-2D hydraulic model should generate the standard flood maps with a 100-year return period. Calibration of GFI model with CADDIES-2D provided a threshold to classify the whole basin into flooded and non-flooded areas. In addition, the novel concept of Intensity-Duration-Frequency-Area (IDFA) curves is introduced to confine the maximum hydrologically contributing area of a basin and improve the performance of GFI model. The flowchart of the presented methodology is illustrated in Figure 1 and different aspects of it are explained in more details, in the following sections.

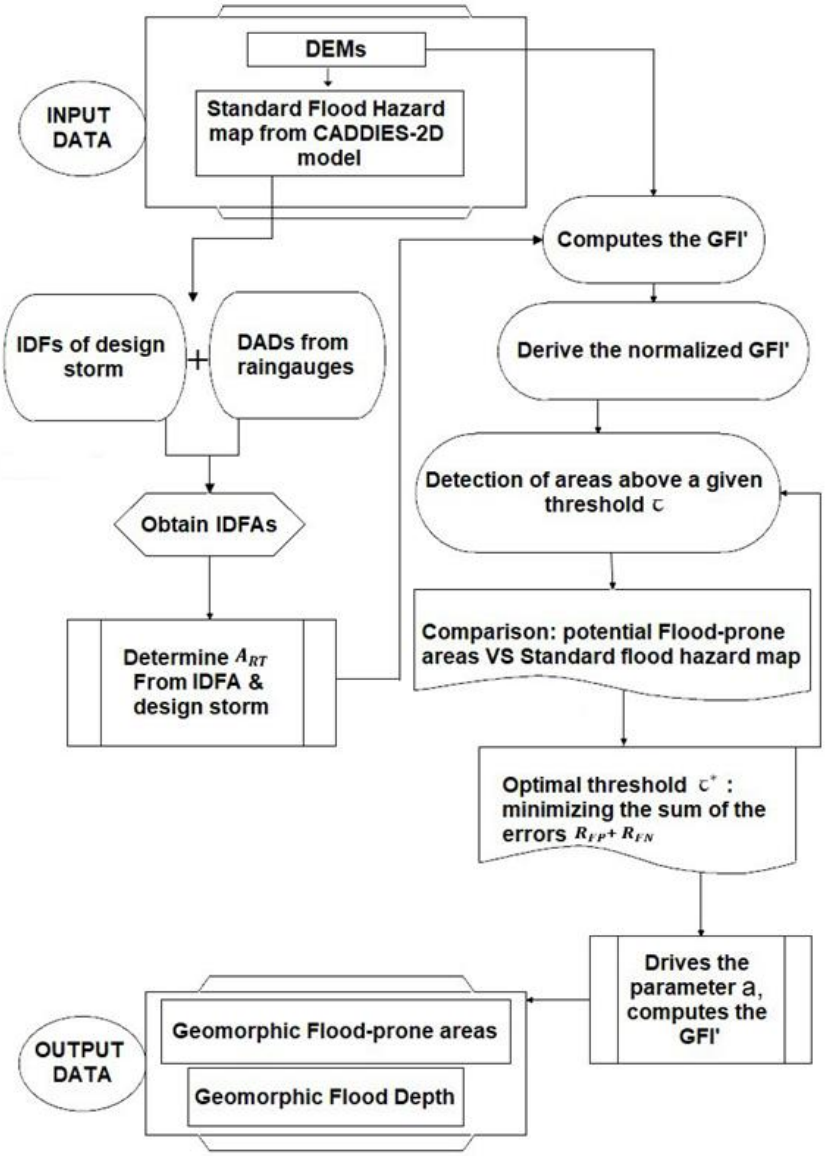

Figure 1. The flowchart of proposed method to simultaneously generate flood extent and depth using geomorphologic indices

1.1.2.1. CADDIES-2D hydraulic model

The Weighted Cellular Automata 2D (WCA2D) version of CADDIES-2D model is utilized to produce the standard flood maps. The WCA2D is a diffusive-like model that neglects inertia and momentum conservation terms which has the following major features [5]:
1. The ratios of water conveyed from central to the downstream neighboring cells (intercellular-volume) are computed using a fast weight-based method;
2. The water volume moved between the central cell and the neighbors is confined by the Manning's and the critical flow equations.
3. The adaptive time step and velocity, both are assessed within a larger updated time step to increase simulation speed and performance.
The WCA2D model is capable of working on grids with different neighborhood types and cells and it can perform parallel computations on a multi-core CPU and graphics card GPU which makes it very fast and suitable for near real time applications. The corresponding application of WCA2D model called CADDIES-caflood is publicly available on the webpage of the Centre for Water Systems at: http://cws.exeter.ac.uk.

1.1.2.2. Geomorphic Flood Index (GFI)

According to Samela et al. [21], the amount of GFI at each study point (green dot in Figure 2-a) is the natural logarithm of water depth (h_r) in the hydrologically nearest waterway point (yellow dot in Figure 2-a) to the elevation difference (H) of those points (green and yellow dots in Figure 2-b)

$$\mathrm{GFI} = \mathrm{Ln}\left(\frac{h_r}{H}\right) \tag{1}$$

Where h_r is calculated as a function of the hydrologically participating area upstream of the point under investigation (A_r) using a power relation developed by Nardi et al. (2006):

$$h_r = aA_r^n \tag{2}$$

Where a and n are the parameters of power function and can be calibrated with the data of hydrometric stations in a region. According to Eq. 1, the locations with GFI values ≥0 are located in the flood prone areas [28].

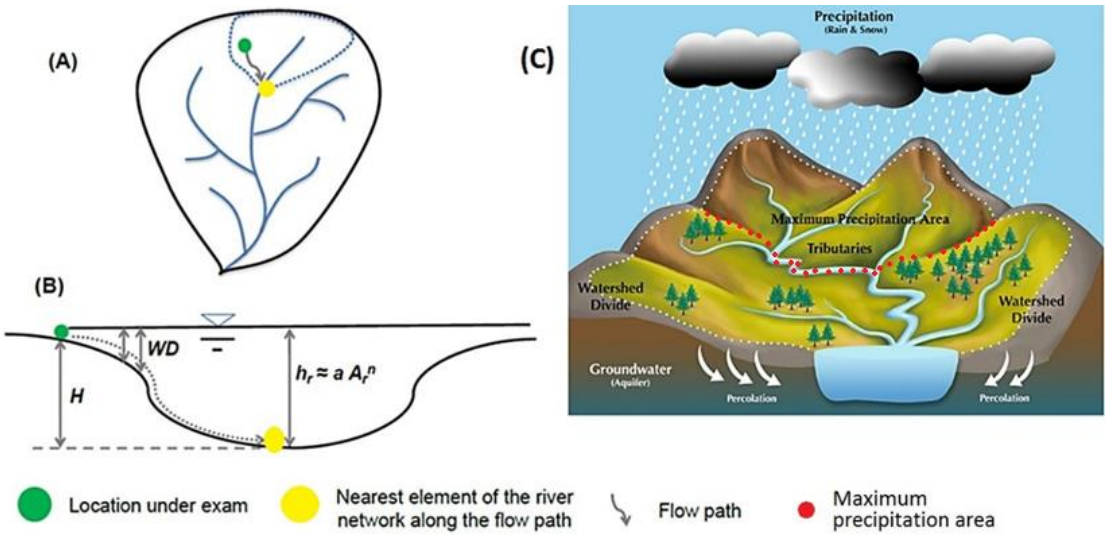

Figure 2. A schematic description of the parameters used to derive the GFI: A) dotted blue line shows the hydrologically contributing area (A_r) of the study location (green circle) B) the water depth (WD) estimated in a hypothetical cross-section (Manfreda et al., 2019); and C) the concept of maximum precipitable area (A_{RT}) delineated by red dotted line which can be smaller than A_r.

Manfreda et al. [28] suggested that GFI can also estimate the maximum inundation depth, assuming that parameter "a" in Eq. 2 does not affect the calibration results of flood prone areas and that can be neglected:

$$GFI' = GFI - \ln(a) = \ln\left(\frac{A_r^n}{H}\right) = \ln\left(\frac{h_r}{aH}\right) \quad (3)$$

Where GFI' acts as a surrogate GFI when hr and H are equal [28]. Given this definition, the linear binary classification is used to divide the range of GFI' values in a basin into flooded and non-flooded classes using a threshold value (τ). The normalized GFI' boundaries (i.e. -1≤τ≤1) should be used and iteratively revised the portion of the basin employed for calibration. For every threshold there is a potential flood-prone area binary map, which is collated to a standard floodplain map (Figure 3). The detailed information about the linear binary classification has been presented in the work of Samela et al. [1], but for computing the optimal normalized threshold, it should be minimizing the sum of the false positive and the false negative values (RFP + RFN), imputing equal weights to the two amounts.

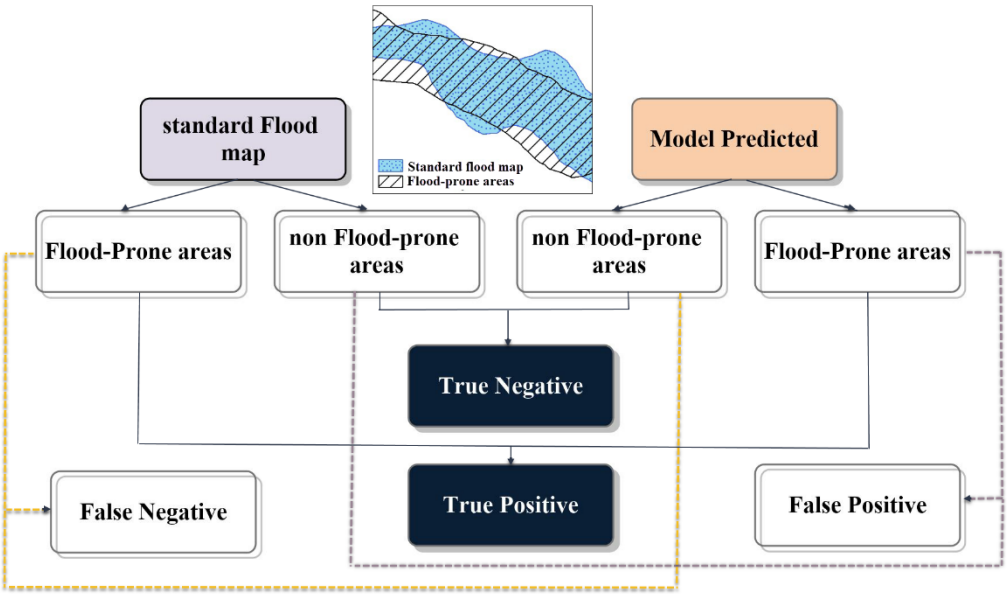

Figure 3. Linear binary classification.

Therefore, the estimated optimal threshold, τ, can be used to derive the parameter a of the scaling function [28]:

$$a = \frac{1}{\exp(\tau)} \quad (4)$$

Thereby, the values of river stage depth h_r in Figure 2-b can be estimated from Eq. (2). Once the water level in the river network is estimated, the next task is to determine the Water Depth (WD) in the adjacent areas. For each point of the basin, the difference between the elevation (H) and the river bed is determined (see Figure 2-b). At this point, the h_r values can be used to estimate the water depth (WD) on a cell by cell basis of the flood-prone areas, as in Eq. 5 [28]:

$$WD = h_r - H \quad (5)$$

In order to implement the GFI, Samela et al. [22] provided Geomorphologic Flood Assessment (GFA) plug-in on QGIS software that can map the basin floodplain from a combination of geomorphological data extracted from the DEM layer, along with floodplain information usually available for part of the basin.

1.1.2.3. Modification of the water depth (h_r)

According to Eq. (2), the contributing area (A_r) of a study point (blue dotted border in Figure 2-a) can get accumulatively larger by moving downstream of a basin resulting in corresponding deeper river depths values

(h_r). However, it should be considered that storms in a region with a certain return period have certain characteristics such as intensity and area of precipitation [29]. This fact is in contradiction with the assumption of GFI and parameter A_r, especially in large basins in arid and semi-arid regions. Therefore, it is suggested to put a limit on A_r and change Eq. 2 as below:

$$h_r \approx \begin{cases} aA_r^n & if A_r < A_{RT} \\ aA_{RT}^n & if A_r \geq A_{RT} \end{cases} \quad (6)$$

Where, A_{RT} is the maximum precipitable area of a storm with a certain return period in the study area. In order to determine A_{RT}, it is suggested here to use the novel concept of Intensity-Duration-Frequency-Area (IDFA) curves of the storms in a study region.

1.1.2.4. Intensity-Duration-Frequency-Area (IDFA) curves

Historical records of rain gauges are necessary to determine rainfall characteristics of a basin. These characteristics are usually studied by developing Intensity-Duration-Frequency (IDF) curves [30] and Depth-Area-Duration (DAD) curves [31]. The IDFs are obtained by fitting a theoretical extreme value distribution (e.g., Gumbel Type I) to the rainfall records to estimate the rainfall events associated with given exceedance probabilities [32]. However, the development of DADs requires isohyet maps obtained from different methods such as: rainfall gradient, simple classic statistical methods, and/or complicated geostatistical methods. Hershfield and Wilson [33] suggested that the spatial pattern of a specific storm (i.e. DAD) follows:

$$\bar{P} = P_{max} e^{-kA^m} \quad (7)$$

Where, $\bar{P}$ (mm) is the average rainfall depth over a specific area A (km^2); P_{max} is the rainfall depth at the center of storm; k and m are constant parameters that can be calibrated from the isohyet maps. While, IDFs provide temporal information about rainfall in a specific location, they do not give any information about rainfall spatial distribution, whereas DADs provide spatial information of a single storm. Therefore, it is suggested here to use a novel concept in hydrometeorology as Intensity-Duration-Frequency-Area (IDFA) curves introduced by Ghahreman [34] which represent all four necessary characteristics of precipitations in a basin. Rain gauge data within and around a basin can reveal rain centers; and regional IDFs ($IDF_{Regional}$) can be driven by interpolation techniques [35]. The average probable precipitation of the design storm with a certain return period ($\bar{P}$) can be calculated by multiplying corresponding duration and intensity values within the $IDF_{Regional}$ curves. P_{max} can then be infused into the DAD of the most intense storm recorded ever in that period. By calculating ($\bar{P}/P_{max}$) ratios for any desired area and applying it to all points on the $IDF_{Regional}$ curves, the area dimension can be added to these curves. Thus, IDFAs can be used to determine the A_{RT} in Eq. (6). 2.1.

1.1.3. Study area

This study focuses on the Frizi, Sarbaz, and Shapour basins in northeast, southeast and south of Iran, respectively (Figure 4). Table 1 provides the meteorological and physiographical characteristics of the study basins. Shapour basin is located in the Fars province with a semi-arid climate, Frizi basin is located on the northern slopes of the Binaloud Mountains in Khorasan Province with a semi-arid cold climate; and Sarbaz basin is located in the southern part of the Sistan and Baluchestan province with hot and dry climate. The areas delineated with dashed lines in figure 4 represent designated areas for the calibration of models which in Shapour basin is a normal fluvial watershed with mountains and plains, and in Frizi and Sarbas basins is an alluvial fan. Alluvial fans are triangular-shaped deposits of water-transported material where there is a rapid change in river slope and tend to be larger and more prominent in arid to semi-arid regions [23].

1.1.4. Input data

1.1.4.1. Digital Elevation Model (DEM)

The Digital Elevation Model (DEM) is a digital map that contains the elevation of all points in a region. The DEM is usually produced and used as a raster structure in GIS software, where the value of each cell is the average height of a small piece of land. The DEM is widely used in physiographic studies and hydrology models, including the production of slope maps, the distribution of elevation changes, and sub-basin extraction [18]. DEM 30m derived from SRTM satellite data is considered as one of the most accurate DEMs among freely available DEMs [20]. Therefore, the DEMs of Frizi, Sarbaz, and Shapour basins were extracted from the USGS EarthExplorer website [24] and used in this part of the study (Figure 4).

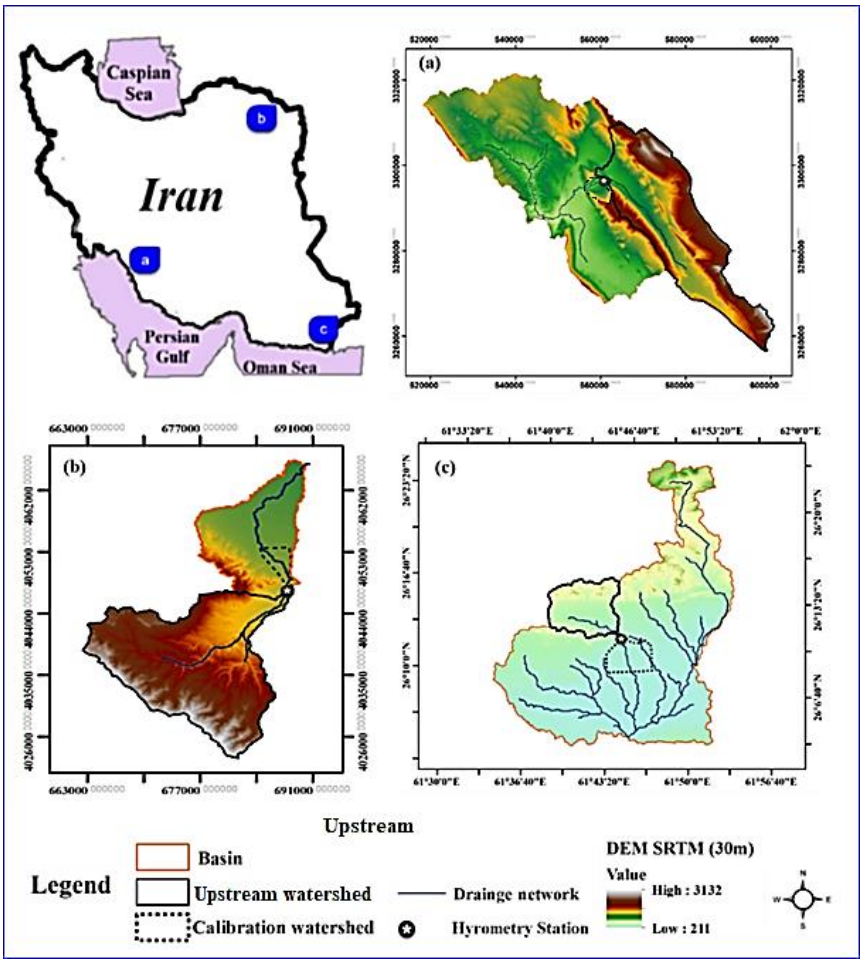

Figure 4. The locations, DEM SRTM 30 m, and alluvial fans of the studied basins: a) Shapour, b) Frizi, and c) Sarbaz, Iran.

Table 1. The characteristics of Shapour basin and two alluvial fans of Frizi and Sarbaz.

	Annual rainfall (mm)	Average temperature (°C)	Relative humidity (%)	Latitude	longitude	Mean elevation (m)	Watershed area (km^2)	Average slope (%)
Sarbaz Basin	90	35	21	N 29° 25’	E 38° 11’	267	628	1.03
	The upstream watershed of calibration area:					505	58.57	12
Frizi alluvial fan	372	15	42	N 20° 36’	E 58° 48’	1193	505	1.04
	The upstream watershed of calibration area:					2060	342.08	21
Shapour alluvial fan	510	23	49	N 29° 25’	E 51° 11’	1311	2031	13.88
	The upstream watershed of calibration area:					1695	718.6	16.8

1.1.4.2. Hydrometric data

The discharge records from hydrometric stations are necessary for generating the design flood hydrographs, which in turn are necessary for delineating the standard flood maps. For the purpose of this part of the study, a design flood with 100-year return period is selected. The maximum discharge of the design flood for the study basins is estimated using the data from hydrometric stations in the basins (Figure 4) and Gumbel probability distribution function. Finally, the design flood hydrographs of the study basins (Figure 5) are derived following the SCS runoff curve number method. The runoff curve number is an empirical parameter used in hydrology for predicting direct runoff or infiltration from rainfall excess developed by the USDA Natural Resources Conservation Service a.k.a. the Soil Conservation Service or SCS [25]. This efficient method is widely used in determining the approximate amount of direct runoff from a rainfall event in a particular area [26,27].

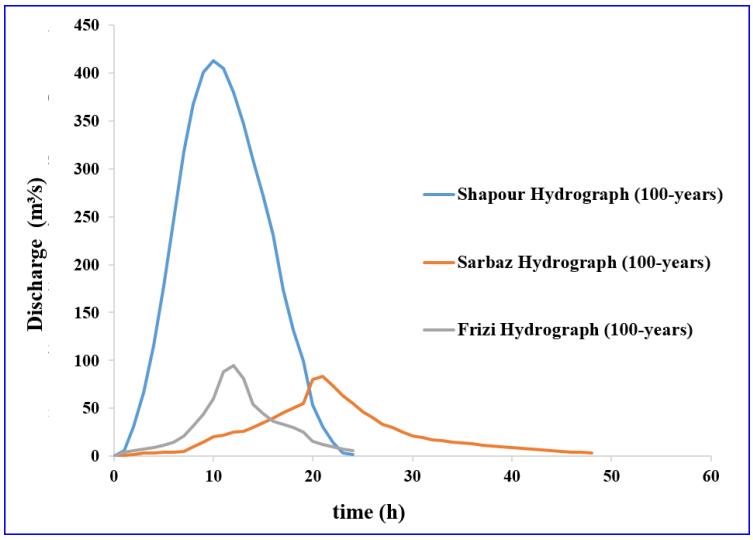

Figure 5. The Hydrographs with 100-years return period for Ferizi, Shapour and Sarbaz basins.

Figure 5 depicts that for a 100-year return period flood, the Shapour basin has a hydrograph with a very high peak discharge whereas Frizi and Sarbaz fans have lower peak discharges due to the lower steepness in the alluvial fans. Figure 5 also shows that Sarbaz basin has the longest concentration time.

1.1.5. Results

The Results and Discussion section should debate the strong points and flaws of the presented figures - for example, composite figures (such as Figures 7, 9, 10) should be commented as internal comparison. Moreover, it is necessary to compare your findings with those of the other authors that used similar analysis methods. This is the discussion needed to highlight the usefulness of your study.

The methodology presented in this paper is implemented following the steps of Figure 3. In order to implement the GFA plug-in which is the corresponding application of GFI model, the required “DEM”, “Filled DEM”, “Flow direction”, and “Flow accumulation” maps of the study area, are obtained from DEM of SRTM (30m) using the “Fill”, “Flow direction” and “Flow accumulation” tools of the Hydrology toolbox in the ArcMap software. In order to achieve to the standard flood maps of the study areas, CADDIES-caflood which is the corresponding application of WCA2D model was utilized. The inputs of the CADDIES-caflood are DEM map (Figure 4) and hydrograph (Figure 5) of the basin; and the outputs are flood depth (m) and velocity (m/s) of the study areas with spatial resolution of 30 m. Figure 6 illustrates the 100-year flood-prone areas (a-c) and water depth results (d-f) of CADDIES-2D model for (1) Sarbaz, (2) Frizi, and (3) Shapour basins, respectively. According to Figure 6- a & b, the avulsion phenomenon in the stream path has been modeled suitably by CADDIES-2D in the Sarbaz and Frizi alluvial fans. Avulsion is the sudden change in the river path during large floods which carry the necessary power to rapidly change the landscape and usually occurs in Alluvial fans [36].

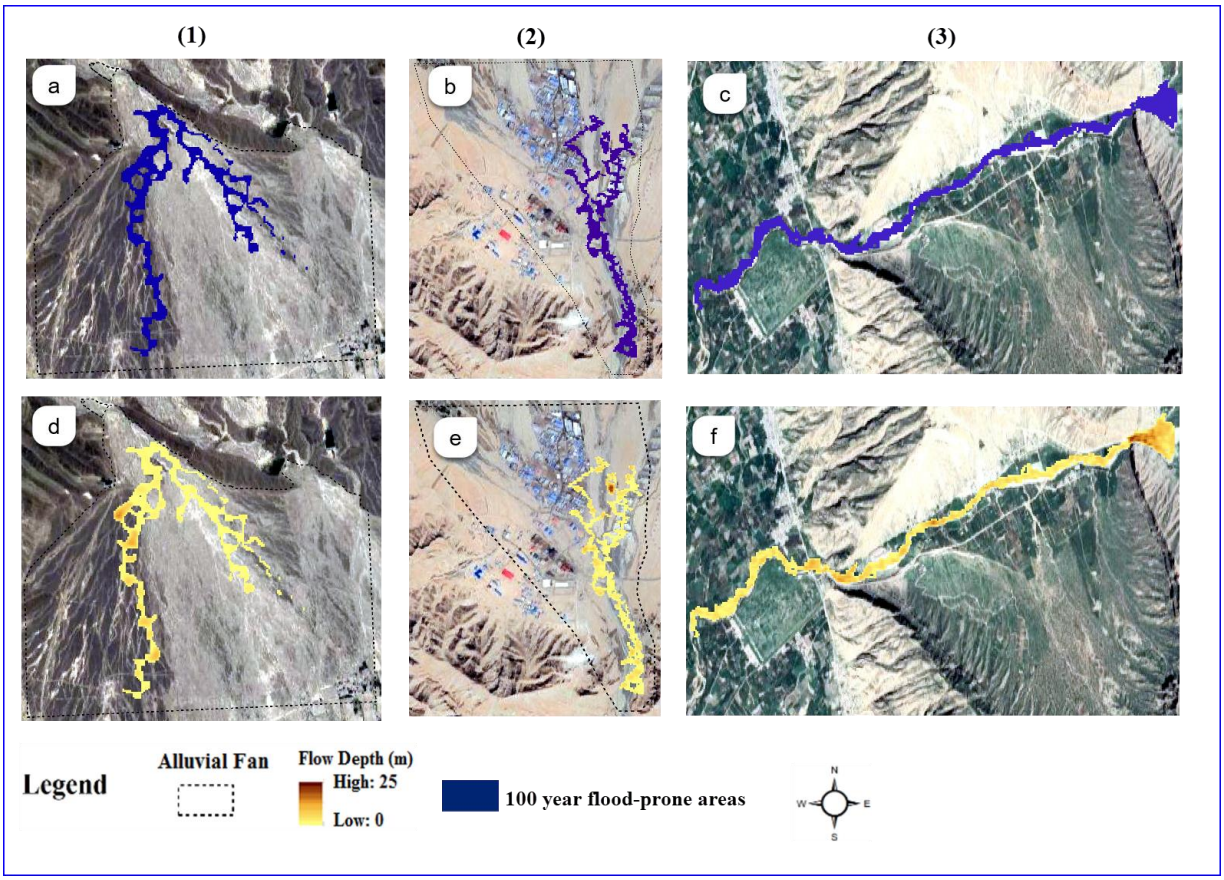

Figure 6. The 100-year standard flood maps (a-c) and flood depth maps (d-f) resulted from CADDIES-2D model for the (1) Sarbaz fan; (2) Frizi fan; and (3) Shapour basin, Iran.

In the next step, the A_{RT} constraint are imposed on h_r (Eq. 6) to prevent the GFA model from producing accumulatively bigger river depth values. In order to calculate A_{RT}, the IDFAs of study areas are plotted in Figure 7 following the section (2.3.4) and information acquired from the most severe storm from rain gauges. Based on Figure 7, the A_{RT} values for a 6-hour design storm with the return period of 100 years are 677, 168, and 210 km^2 for Shapour, Frizi and Sarbaz basins, respectively. Then, the standard flood maps (fig 6 a-c) are used to calibrate the GFI' threshold (τ) in Eq. 3 following the linear binary algorithm. Having all the required inputs, the GFA outputs are the 100-year floodplain of study areas presented in Figure (8), and the performance metrics including the calibrated threshold (τ), type 1 error (R_{FP}), sensitivity (R_{TP}), sum of errors (R_{FP}+ (1-R_{TP})), and model precision (AUC) which are presented in table 2. AUC equal to 1 represents 100% success in detecting flood prone areas with respect to the standard flood map [1]. It should be noted that modifying $h_r$values in the GFI model produced different results which are presented under the name of "Modified GFI" in Figure 8 (c,f,i) and table 2.

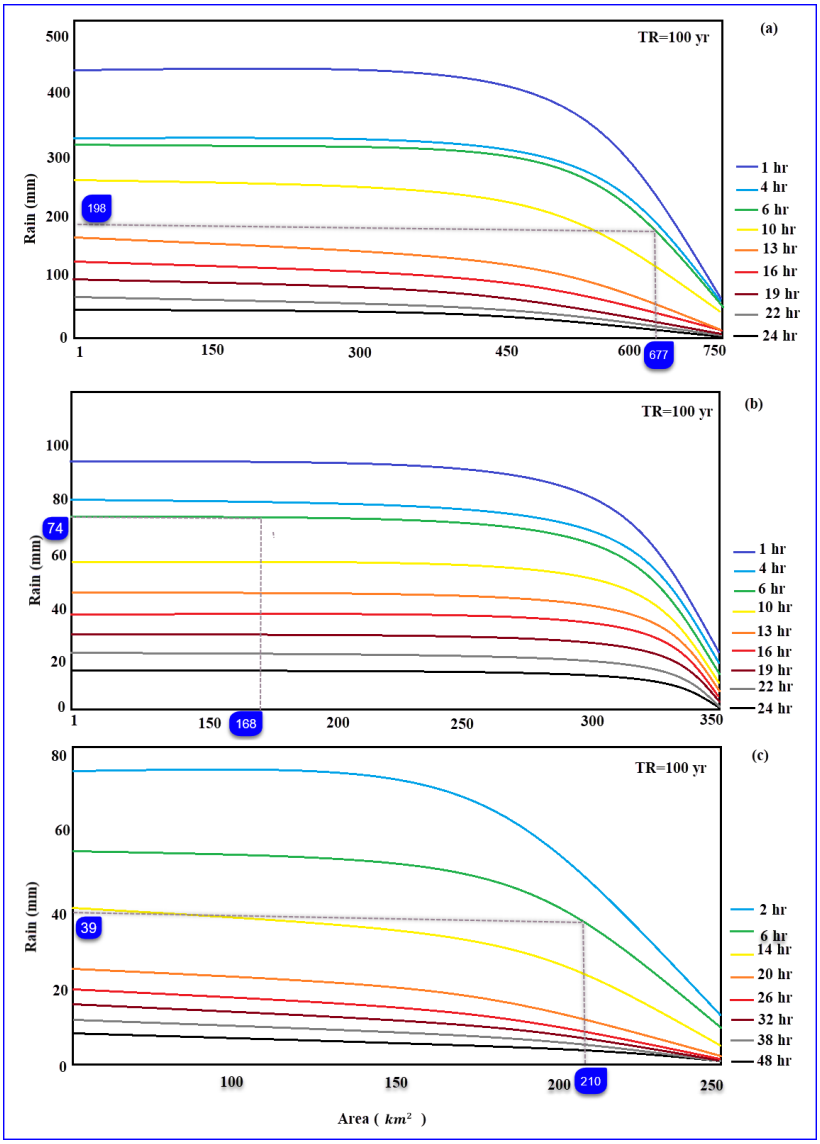

Figure 7. IDFA curves for a) Shapour, b) Frizi, and c) Sarbaz basins.

Table 2. The performance of linear binary classification of GFA model based on the GFI and modified GFI

Basin name		τ^a	$R_{FP}{}^*$	$R_{TP}{}^{**}$	$R_{FP}+(1-R_{TP})^{***}$	AUC^b	Ratio of calibration area (%)
Sarbaz	Modified GFI	-0.25	0.11	0.17	0.94	0.42	2.45
	GFI	-0.24	0.12	0.16	0.95	0.40	
Frizi	Modified GFI	-0.23	0.45	0.58	0.87	0.53	2.12
	GFI	-0.25	0.47	0.55	0.89	0.51	
Shapour	Modified GFI	-0.28	0.10	0.98	0.12	0.96	2.83
	GFI	-0.30	0.11	0.95	0.14	0.93	

[a] optimal threshold value τ, [*] false positive rate R_{FP}, [**]true positive rate R_{TP}, [***]sum of errors $R_{FP} + (1 - R_{TP})$, and [b] area under the curve AUC for basin.

Based on table 2, locations with GFI' values bigger than τ are inside the flood zone. Comparing AUC and $R_{FP}+(1- R_{TP})$ values also reveals that modified GFI has a better performance than GFI in all study basins, and that GFA model generally performs better in identifying flood prone areas in fluvial rivers (Shapour basin) than in alluvial fans (Sarbaz and Frizi). The visual inspection of flood maps in Figure 8 also proves the abovementioned findings.

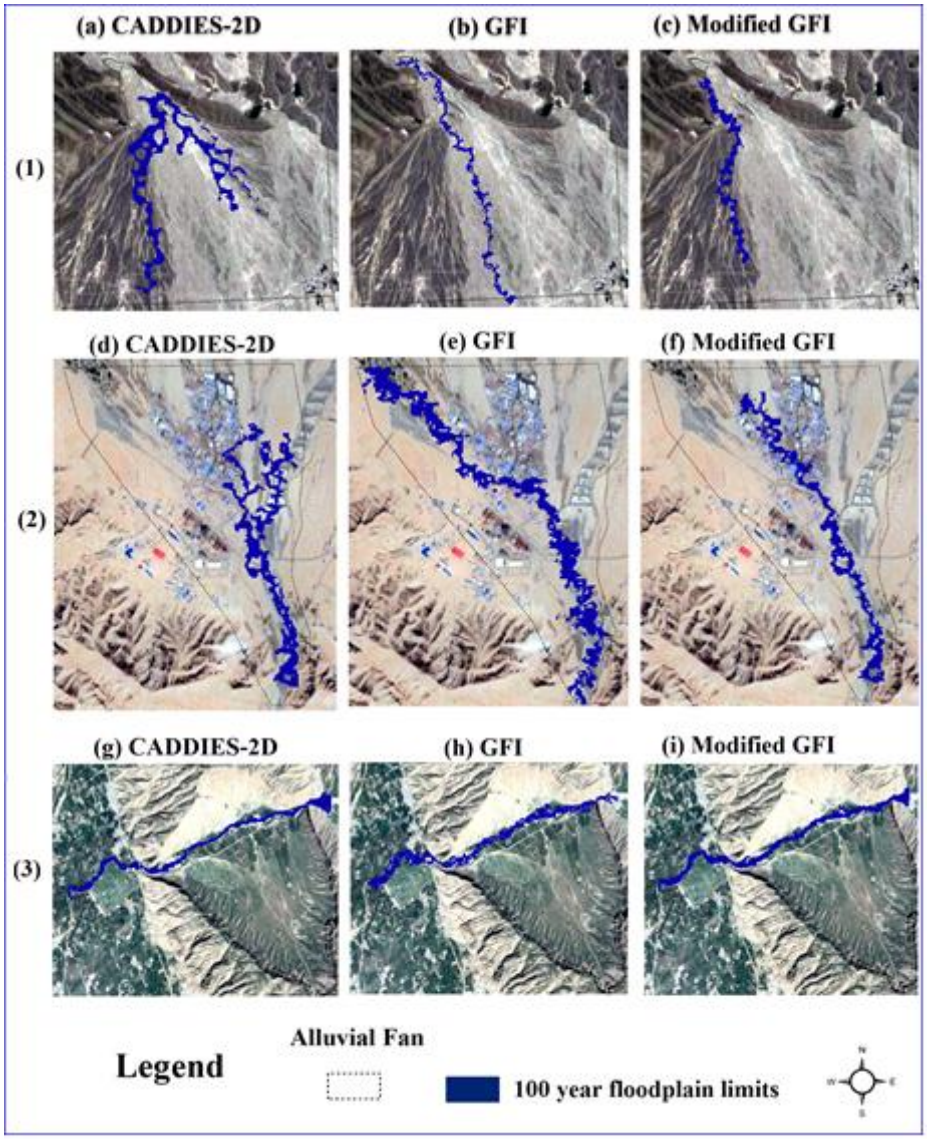

Figure 8. The floodplain limits from CADDIES-2D model (Col. 1), GFI (Col. 2), and modified GFI (Col. 3) for the (1) Sarbaz fan, (2) Frizi fan, and (3) Shapour basin.

In order to achieve the GFI flood depth of each study basin from Eq. 2, the parameter a is calculated from Eq. 4 and τ values in table 2. Once the water level in the river network is estimated, the water depth (WD) in the adjacent areas are estimated from the difference in the elevation (H) between them and the river bed following Eq. 5. The flood depth maps of CADDIES-2D, GFI and modified GFI models for the study areas are presented in Figure 9.

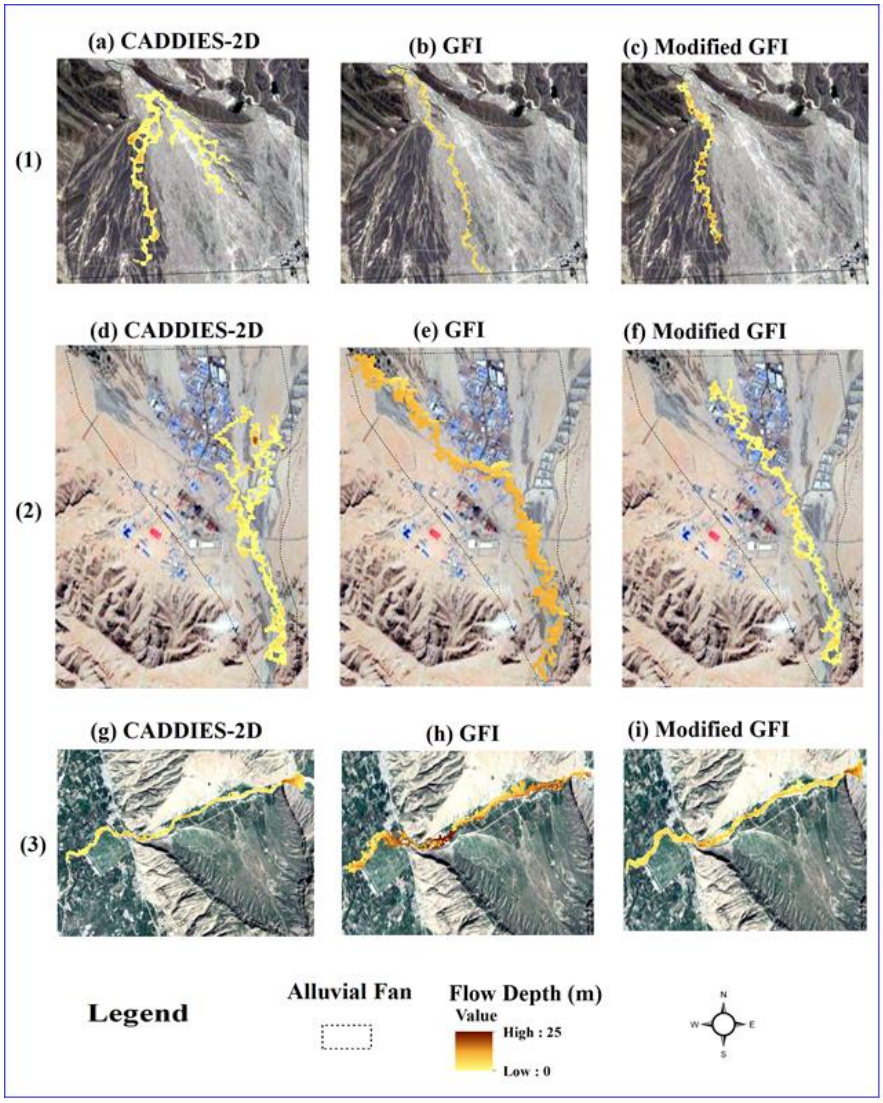

Figure 9. Flow depth results of CADDIES-2D model (Col. 1), GFI (Col. 2), and modified GFI (Col. 3) for (1) Sarbaz fan; (2) Frizi fan; and (3) Shapour basin, Iran.

Figure 9 illustrates that in comparison with the CADDIES-2D flood map, the GFI model is able to capture the general trend in WD variations, though it overestimates the WD in the Frizi and Shapour basins. This problem is mitigated in the results of modified GFI. Finally, the GFI calibrated thresholds (τ) are used in the rest of study areas to achieve complete 100-year floodplain maps (Figure 10). As can be seen in fig 10, the flood prone areas even in the most remote regions of the study basins have been delineated using only DEM maps.

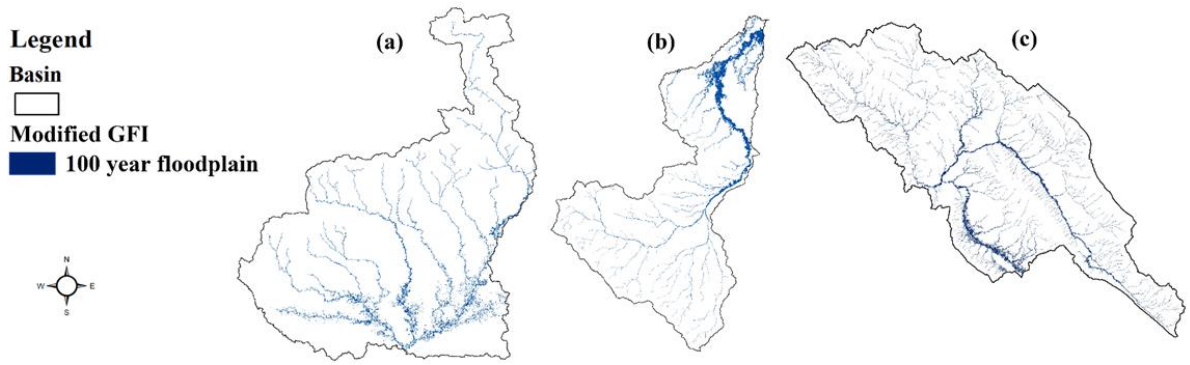

Figure 10. The modified GFI model output of flood prone areas for whole basin in (a) Sarbaz, (b) Frizi, and (C) the Shapour

1.1.6. Conclusion

Conventional hydraulic methods of flood mapping require high computational capacities and multiple data sets, which despite their high accuracy, make them not applicable in the large scale ungauged regions. However, the results of these methods are available at smaller scales which can be generalized to large scales using geomorphological indices. Based on the literature, the GFI morphological flood index and its application GFA tool have the best performance in producing flood extents and also capable of giving a rough estimate of flood depth using only DEM maps and a standard flood map of a small portion of the study area. The work in this paper implements the GFI model and enhances its performance through imposing the constraint of maximum precipitable area (ART) which is estimated through generating Intensity-Duration-Frequency-Area curves. The IDFAs are a novel concept in hydrometeorology which represent all four necessary characteristics of precipitation in a basin. The performance of developed method was demonstrated by application to the Frizi, Sarbaz and Shapour basins in different parts of Iran. The inputs of this method are the DEM-SRTM-30m and the 100-year standard floodplain derived from CADDIES-2D model, which is used to find the optimum threshold (τ) of the binary classification of the GFI values. The results show that the GFA model has a high ability to delineate flood extents in the fluvial and mountainous basins (Shapour basin) while it cannot model the avulsion phenomenon in the alluvial fans (Sarbaz and Frizi basins). In terms of flood depth, despite overestimation, the GFI model is able to capture the general trend in the water depth variations. This problem is reduced by the modified GFI and it produces better flood depth results. Finally, the calibrated thresholds (τ) are used to generalize the GFI results to the whole study areas to achieve complete 100-year floodplain maps. It can be concluded that the GFI model is capable of estimating flood extents and depth in the large-scale ungauged basins with its best performance in the regions with steep slopes (e.g. mountains areas and fluvial rivers), and with more precaution in the flatter regions (e.g. plains and alluvial fans).

1.1.7. References

1. Samela, C.; Troy, T.J.; Manfreda, S. Geomorphic classifiers for flood-prone areas delineation for data-scarce environments. *Advances in Water Resources* **2017**, *102*, 13-28.
2. Guidolin, M.; Duncan, A.; Ghimire, B.; Gibson, M.; Keedwell, E.; Chen, A.S.; Djordjevic, S.; Savic, D. CADDIES: a new framework for rapid development of parallel cellular automata algorithms for flood simulation. **2012**.
3. Hunter, N.M.; Bates, P.D.; Horritt, M.S.; Wilson, M.D. Simple spatially-distributed models for predicting flood inundation: a review. *Geomorphology* **2007**, *90*, 208-225.
4. Yen, B.; Tsai, C.-S. On noninertia wave versus diffusion wave in flood routing. *Journal of Hydrology* **2001**, *244*, 97-104.
5. Guidolin, M.; Chen, A.S.; Ghimire, B.; Keedwell, E.C.; Djordjević, S.; Savić, D.A. A weighted cellular automata 2D inundation model for rapid flood analysis. *Environmental Modelling & Software* **2016**, *84*, 378-394.
6. Wolfram, S. Cellular automata as models of complexity. *Nature* **1984**, *311*, 419-424.
7. Itami, R.M. Simulating spatial dynamics: cellular automata theory. *Landscape and urban planning* **1994**, *30*, 27-47.
8. Dottori, F.; Todini, E. A 2D flood inundation model based on cellular automata approach. In Proceedings of XVIII International Conference on Water Resources CMWR.
9. Dottori, F.; Todini, E. Developments of a flood inundation model based on the cellular automata approach: testing different methods to improve model performance. *Physics and Chemistry of the Earth, Parts A/B/C* **2011**, *36*, 266-280.
10. Ghimire, B.; Chen, A.S.; Guidolin, M.; Keedwell, E.C.; Djordjević, S.; Savić, D.A. Formulation of a fast 2D urban pluvial flood model using a cellular automata approach. *Journal of Hydroinformatics* **2013**, *15*, 676-686.
11. Nardi, F.; Biscarini, C.; Di Francesco, S.; Manciola, P.; Ubertini, L. Comparing a large-scale DEM-based floodplain delineation algorithm with standard flood maps: The Tiber River Basin case study. *Irrigation and Drainage* **2013**, *62*, 11-19.
12. Chen, A.S.; Khoury, M.; Vamvakeridou-Lyroudia, L.; Stewart, D.; Wood, M.; Savic, D.A.; Djordjevic, S. 3D visualisation tool for improving the resilience to urban and coastal flooding in Torbay, UK. *Procedia engineering* **2018**, *212*, 809-815.
13. Wang, Y.; Liu, H.; Zhang, C.; Li, M.; Peng, Y. Urban Flood Simulation and Risk Analysis Based on Cellular Automaton. *Journal of Water Resources Research* *水资源研究* **2018**, *7*, 360-369.
14. Webber, J.L.; Burns, M.J.; Fu, G.; Butler, D.; Fletcher, T.D. Evaluating City Scale Surface Water Management Using a Rapid Assessment Framework in Melbourne, Australia. In Proceedings of International Conference on Urban Drainage Modelling; pp. 920-925.
15. Arnaud-Fassetta, G.; Astrade, L.; Bardou, E.; Corbonnois, J.; Delahaye, D.; Fort, M.; Gautier, E.; Jacob, N.; Peiry, J.-L.; Piégay, H. Fluvial geomorphology and flood-risk management. *Géomorphologie: relief, processus, environnement* **2009**, *15*, 109-128.

16. Manfreda, S.; Di Leo, M.; Sole, A. Detection of flood-prone areas using digital elevation models. *Journal of Hydrologic Engineering* **2011**, *16*, 781-790.
17. Beven, K.J.; Kirkby, M.J. A physically based, variable contributing area model of basin hydrology/Un modèle à base physique de zone d'appel variable de l'hydrologie du bassin versant. *Hydrological Sciences Journal* **1979**, *24*, 43-69.
18. Manfreda, S.; Samela, C.; Sole, A.; Fiorentino, M. Flood-prone areas assessment using linear binary classifiers based on morphological indices. In *Vulnerability, Uncertainty, and Risk: Quantification, Mitigation, and Management*, 2014; pp. 2002-2011.
19. Manfreda, S.; Samela, C.; Gioia, A.; Consoli, G.G.; Iacobellis, V.; Giuzio, L.; Cantisani, A.; Sole, A. Flood-prone areas assessment using linear binary classifiers based on flood maps obtained from 1D and 2D hydraulic models. *Natural Hazards* **2015**, *79*, 735-754.
20. Samela, C.; Manfreda, S.; Paola, F.D.; Giugni, M.; Sole, A.; Fiorentino, M. DEM-based approaches for the delineation of flood-prone areas in an ungauged basin in Africa. *Journal of Hydrologic Engineering* **2016**, *21*, 06015010.
21. Samela, C.; Manfreda, S.; Troy, T.J. Dataset of 100-year flood susceptibility maps for the continental US derived with a geomorphic method. *Data in brief* **2017**, *12*, 203-207.
22. Samela, C.; Albano, R.; Sole, A.; Manfreda, S. A GIS tool for cost-effective delineation of flood-prone areas. *Computers, Environment and Urban Systems* **2018**, *70*, 43-52.
23. Cazanacli, D.; Paola, C.; Parker, G. Experimental steep, braided flow: application to flooding risk on fans. *Journal of Hydraulic Engineering* **2002**, *128*, 322-330.
24. JPL, N. NASA Shuttle Radar Topography Mission Global 1 arc second. Version 3. In *NASA EOSDIS LP DAAC, USGS Earth Resources Observation and Science (EROS) Center*, USA Sioux Falls, South Dakota: 2013.
25. Cronshey, R. *Urban hydrology for small watersheds*; US Dept. of Agriculture, Soil Conservation Service, Engineering Division: 1986.
26. Woodward, D.E.; Hawkins, R.H.; Jiang, R.; Hjelmfelt, J., Allen T; Van Mullem, J.A.; Quan, Q.D. Runoff curve number method: examination of the initial abstraction ratio. In Proceedings of World water & environmental resources congress 2003; pp. 1-10.
27. Zeng, Z.; Tang, G.; Hong, Y.; Zeng, C.; Yang, Y. Development of an NRCS curve number global dataset using the latest geospatial remote sensing data for worldwide hydrologic applications. *Remote Sensing Letters* **2017**, *8*, 528-536.
28. Manfreda, S.; Samela, C. A digital elevation model based method for a rapid estimation of flood inundation depth. *Journal of Flood Risk Management* **2019**, *12*, e12541.
29. Organization, W.M. *Manual for Depth-area-duration Analysis of Storm Precipitation: This Publication is a Part of the Contribution of WMO to the International Hydrological Decade*; World Meteorological Organization: 1969.
30. Pilgrim, D.; Cordery, I.; French, R. Temporal patterns of design rainfall for Sydney. *Civil Engineering Transactions* **1969**, 9-14.
31. Bureau, U.W. Manual for Depth-Area-Duration analysis of storm precipitation. *Cooperative Studies Technical Paper* **1946**, 99.
32. Koutsoyiannis, D.; Kozonis, D.; Manetas, A. A mathematical framework for studying rainfall intensity-duration-frequency relationships. *Journal of Hydrology* **1998**, *206*, 118-135.
33. Hershfield, D.M.; Wilson, W.T. A comparison of extreme rainfall depths from tropical and nontropical storms. *Journal of Geophysical Research* **1960**, *65*, 959-982.
34. Ghahreman, B. Derivation of Intensity-Duration-Frequency-Area (IDFA) Curves for Mashhad City. *Computational Methods in Engineering* **1998**, *17*, 69-81.
35. Myers, V.A.; Zehr, R.M. *A methodology for point-to-area rainfall frequency ratios*; Department of Commerce, National Oceanic and Atmospheric Administration …: 1980; Vol. 55.
36. Mollaei, Z.; Davary, K.; Hasheminia, S.M.; Faridhosseini, A.; Pourmohamad, Y. Enhancing flood hazard estimation methods on alluvial fans using an integrated hydraulic, geological and geomorphological approach. *Natural Hazards and Earth System Sciences* **2018**, *18*, 1159-1171.

Part 2. Flood mapping and monitoring using Google Earth Engine

1.2.1. Introduction

Among the natural disasters, floods cause wide-scale damages to the properties, infrastructures and lives of millions of people around the world. By increasing the risk of floods as a result of climate change, the need for flood monitoring methods based on satellite-based Earth Observation (EO) data is becoming more important [1]. While the commonly used flood risk models have been shown to significantly under-estimate flood risk, the EO based methods provide synoptic, repeated views of potentially flooded regions [2].
Increasing the number of EO satellites has increased the spatio-temporal resolution of available data for studying water surfaces for different purposes such as agriculture, disaster management, and hydrology. Several studies have utilized Visible and Near-Infrared (NIR) images to detect and monitor surface water bodies (e.g. [3-6]) by considering positive values of Normalized Difference Water Index (NDWI) and/or Modification of Normalized Difference Water Index (MNDWI); values higher than an optimum threshold of NIR reflectances; and combining NIR data and the Normalized Difference Vegetation Index (NDVI). However, cloud presence, dense vegetation and turbid surface water are among the limiting factors for applying such methods by making visual barriers or changing the NIR/Red band reflectance ratio [7].
The data acquired from Synthetic Aperture Radar (SAR) sensors can effectively detect smooth water surfaces based on their low backscatter values in comparison with non-water areas [8], regardless of the cloud cover, day and night, with spatial resolution comparable to visible and near-infrared satellite images [7]. Many studies tried to classify water pixels by applying a threshold on backscattered SAR values [6,9-11]. Others tried to identify flooded pixels based on change detection approaches using before, during and after flood SAR imagery [6,12-16]. However, backscattering from flooded vegetation or wind-affected open water surfaces is more complex due to the multiple-bounce scattering, which can be dealt with using both the amplitude (intensity) and phase components of the received microwave energy [17].
While the EO satellites can provide reasonably reliable estimates of large extent floods, their assimilation into hydraulic models or other types of data has been shown to improve flood extent estimates on a near real-time basis [18,19]. For example, digital elevation models (DEMs) can be used to constrain EO-based flood estimates to areas likely to experience flooding [20,21]. SAR data can be combined with the optical EO data and priori surface water datasets to allow for multi-scale flood assessment, an increase in observation density during flooding events, or automated training data selection [8].
The open access policy from operational EO satellites has enabled researchers to monitor land changes in the large scales [22]. The Sentinel-1A and -1B satellites are among such satellites providing global synthetic aperture radar (SAR) data with the nominal 6-day repeat imagery over Europe and nominal 12-day repeat imagery over the rest of the world, which is suitable for regular monitoring of change processes [23]. Considering the limitations of optical data for flood monitoring due to the cloud contamination or revisit time, having access to operational SAR EO data is an important development for disaster monitoring. The pre-processing steps of SAR images still requires expertise and high computational power, even by using the free, open-source pre-processing software distributed by ESA [8].
Cloud computing architectures allow users and developers to access entire EO data archives and reduce the need to download and store huge volumes of data [8,24]. The Google Earth Engine (GEE) is one of those cloud computing platforms which enables the development of global-scale data products using satellite image archives [25]. The GEE has been used at different EO monitoring applications such as: surface water [26-28], forest cover [29,30], cropland and soils [31,32]. One of the geospatial datasets that the GEE houses is a complete and continually updated archive of Sentinel-1 Ground Range Detected (GRD) data. Considering the complexity of SAR preprocessing steps, the provision of such data on the GEE represents a big step forward in applied SAR remote sensing. Additionally, the presence of other data sources, such as the entire global Landsat, Sentinel-2 or DEM SRTM archives, allow for relatively easy integration of diverse EO data sources. For example, the SAR surface water classification could be trained with the Sentinel-2 observations under clear sky conditions and the classification could then be extended to the cloudy areas using the SAR data [8].
The purpose of this part of the study would be to employ the GEE for monitoring two recent flood events in Iran and Italy using Sentinel-1 SAR and Sentinel-2 optical data. In this paper, we investigate the influence of

flooding on Sentinel-1 VV and VH SAR backscatter; Sentinel-2 multispectral water indices; and evaluate the accuracy of flood maps with standard flood maps.

1.2.2. Methodology

1.2.2.1. Flood mapping

Flooded areas can be identified by applying supervised and unsupervised approaches on the Sentinel-1 and Sentinel-2 archives using built-in functions in the GEE [6,36]. For the supervised classification, a standard flood map from an authenticated data source can be used to train the Random Forest classification which exists in the GEE platform [37]. For the unsupervised classification, an optimum threshold can classify Sentinel-1 backscattering difference and Sentinel-2 water spectral index into flooded and non-flooded areas. At the end, results can be improved by excluding areas with higher than 5% slope, less than 4 pixel neighbors, and permanent water bodies [38]. Figure 1 shows the methods and the procedures used for the flood mapping.
In the following, different parts of the methodology have been explained in more details:

- Backscattering variation: Two SAR images (one post-/co-flood and one pre-flood) can be used for change detection analyses [38]. SAR GRD data are radiometrically calibrated which can be averaged through a reducer command in the GEE. Surface changes due to flooding can be detected by calculating the ratio between the post- and the pre-flood images. An empirical threshold can be applied for the classification of flooded areas.
- Multispectral Image Processing: The NDVI, NDWI, and MNDWI indices can be calculated based on normalized differences of NIR-RED, GREEN-SWIR, and RED-SWIR bands of a single Sentinel-2 image [38]. Flooded and non-flooded pixels can be discriminated by an empirical threshold based on a visual approach; we set the threshold that best fits with the EMS maps.
- Supervised classification: this technique can be applied to classify both Sentinel-1 and Sentinel-2 data. The floodplains provided by EMS can be used in training areas selected over a composite band image. Then, a supervised classification of the images can be performed using Random Forest function in the GEE. A random-forest model is an ensemble-learning technique for which a multitude of decision trees is constructed to explain the spatial relationships between the occurrence of floods and the related factors for classification and regression [39].

1.2.2.2. Flood monitoring

A simple and fast flood monitoring system can also be presented within Google Earth Engine platform based on time-series analysis of the water indices obtain from Sentinel-1 and sentinel-2 satellites. Surpassing the studied water index from a threshold can raise the flood alarm in the study area indicating that the study point in the area has been inundated. Figure 2 shows the methods and the procedures used for the flood monitoring.

1.2.2.3. Flood Map Validation and Quality Statistics

The final step of the work is the validation and quality assessment of all the produced flood area maps (semi-automatic and manual). To do this task, we used the flood maps made by official authorities and published online as a benchmark (i.e. Copernicus EMS - Mapping). The theory behind the validation procedure in the GEE is described in the following [38]:

a. Both the produced flooded area maps and the official reference maps are converted into a Boolean raster format (1—flooded or 0—not flooded)
b. The two raster are crossed, and a raster map with four possible values is generated: False negative (FN), false positive (FP), true positive (TP), and true negative (TN). TP represents the areas correctly classified as flooded, TN are the areas correctly classified as not flooded, FN indicates the undetected flooded areas, and FP are the not-flooded areas erroneously classified as inundated.
c. The accuracy of the classification is evaluated by computing the flood-mapping ratio (Equation (1)) and the non-flood ratio (Equation (2)):

$$FR\ (\%) = TP/\ (TP + FN) \quad (1)$$

$$NFR\ (\%) = TN/\ (TN + FP) \quad (2)$$

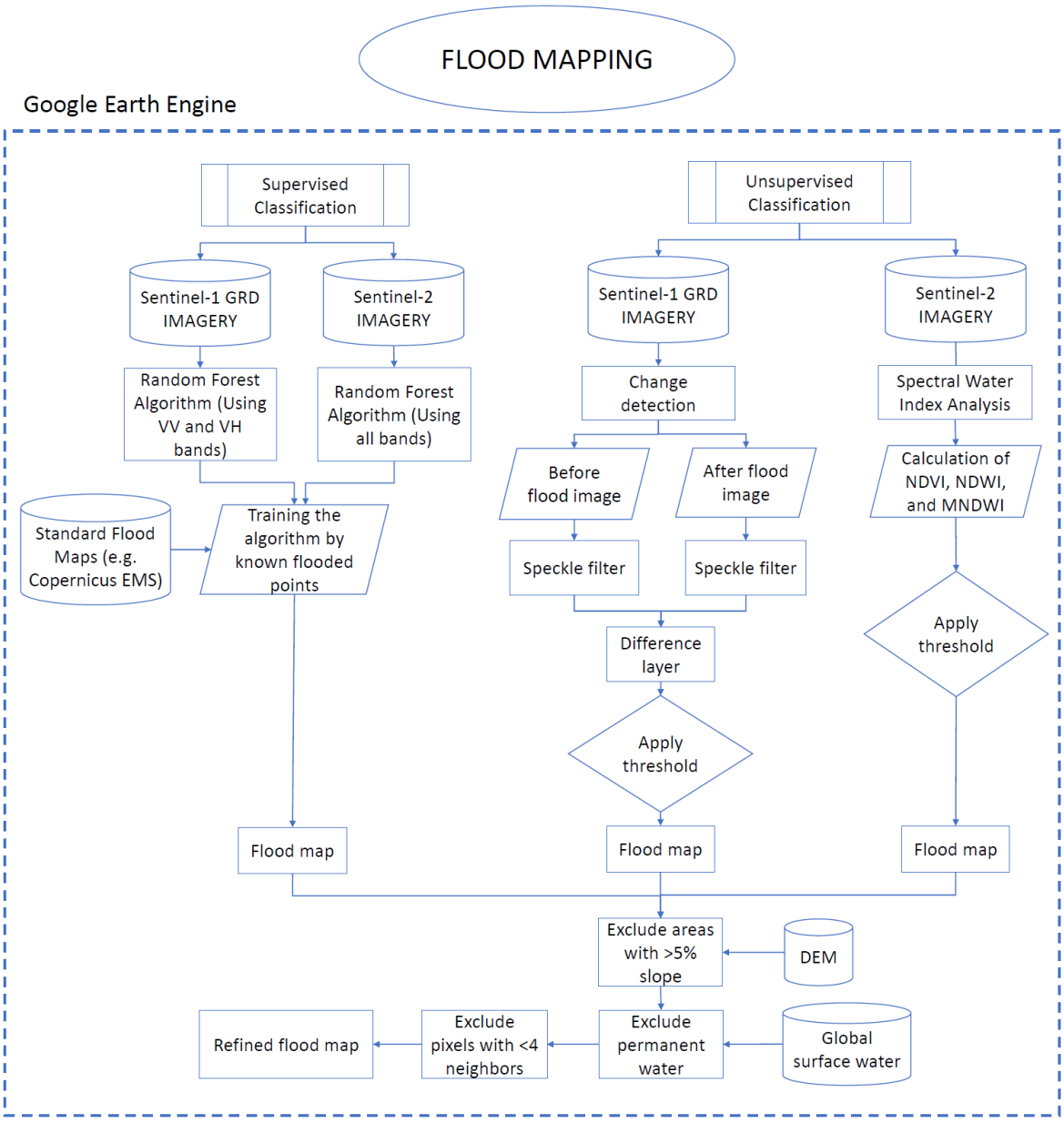

Figure 1. Flood mapping methodology used in this part of the study.

1.2.3. Site and event descriptions

In this part of the study, we focused our evaluation of the method over three events: (1) floods in December 2013 over Metaponto, Italy; (3) floods in March 2019, over Khuzestan, Iran; and (2) floods in October 2020 over Piedmont, Italy. Each of these sites and events are briefly described below.

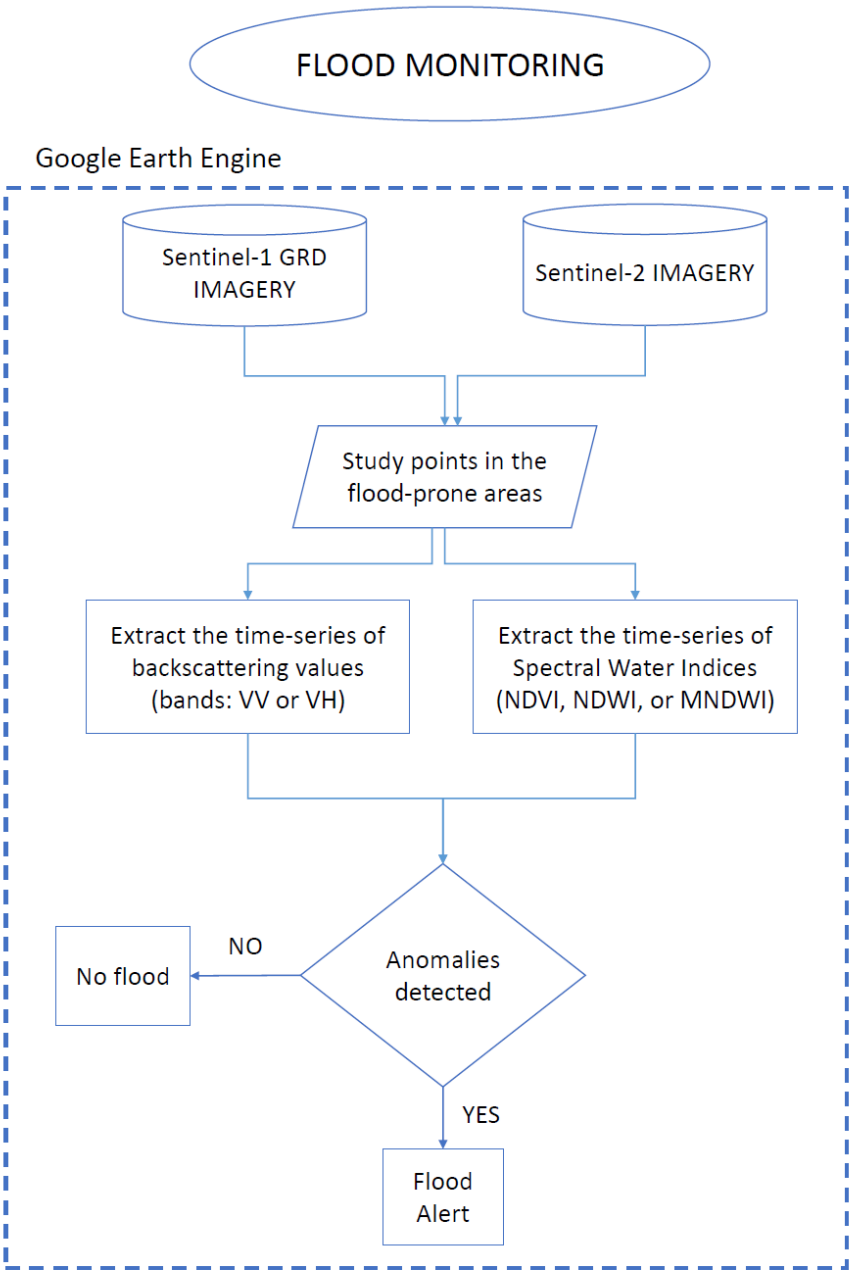

Figure 2. Flood monitoring methodology used for this work

1.2.3.1. Metaponto

The study area is located in southern Italy, in Basilicata, in the Gulf of Taranto, on the Ionian Sea. It is enclosed between the Cavone (south-west) and Bradano (north-east) rivers, up to the Appulo-Lucano Apennines in the north-west and the Ionian Sea in the south-west. The choice was made for the importance of the archaeological remains in the territory of the city of Metaponto, in recent years several times at risk due to natural and anthropogenic events (fires, floods, change of the shoreline). The area covers about 132 km2 and this extension has been considered for the flood analysis (Figure 3). According to Lacava et al. [43], a major flood happened on 1-2 Dec 2013 which involved all of the rivers. Since the flood in 2013 happened before launching the Sentinel 1 and 2, this event was studied by the first cloud free Landsat 8 Operational Land Imager (OLI) and Thermal Infrared (TIRS) Collection 2 Level-2 Science Products 30-meter multispectral data (on 6 December 2013).

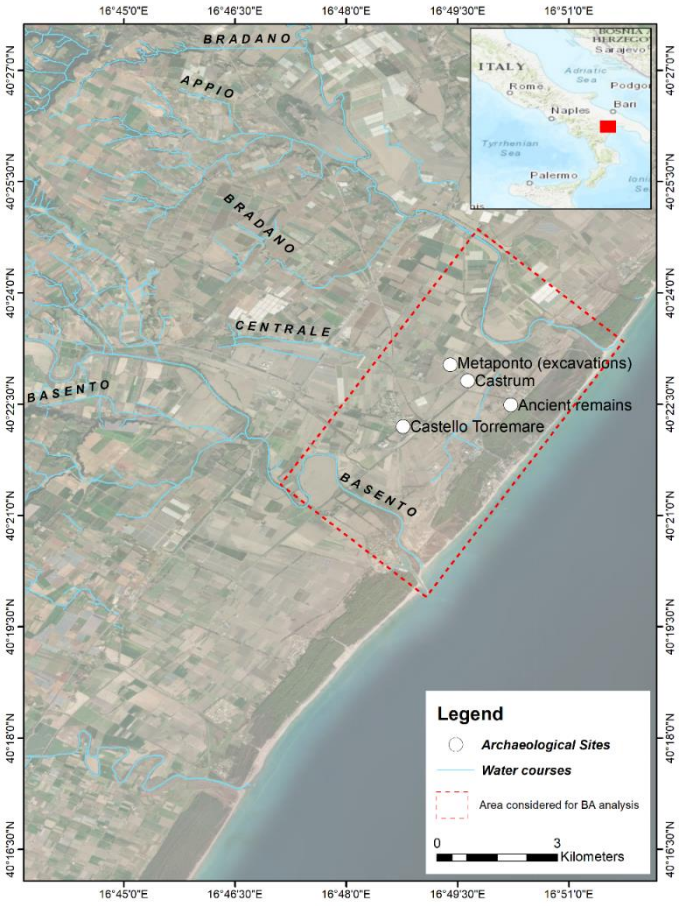

Figure 3. The general view and location of Metaponto Plain, Italy.

1.2.3.2. Shushtar, Khuzestan, Iran

According to the Iranian Water Resource Management Co. (WRM), two major storms happened within one week on 25 Mar 2019 and 1 Apr 2019 (Fig. 4a) over the Grand Karoun Basin located in Khuzestan Porvince, southwest Iran (Fig. 4b). As a consequence, a major flood occurred in this province causing devastative damages to urban and agriculture sectors. Moreover, there are many historical sites in the region dating back to 500 B.C. and most of them located near water resources including the UNESCO heritage site Shushtar Historical Hydraulic System (Fig. 4c).

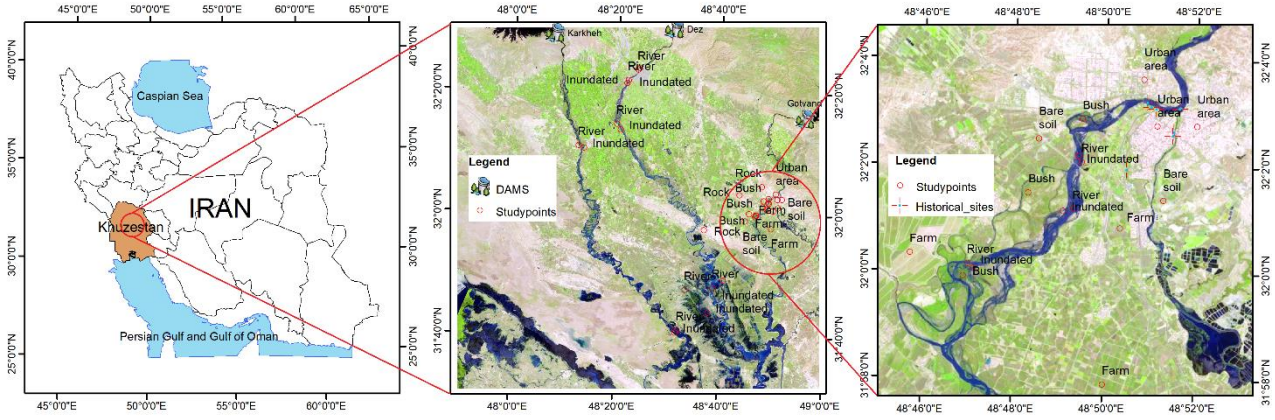

(**a**) (**b**) (**c**)

Figure 4. The general view and location of (**a**) Khuzestan Province in southwest Iran, (**b**) Grand Karoun Basin and upstream Karkheh, Dez and Gotvand dams, (**c**) the study area around the Shushtar City as well as the location of Historical sites and study points.

1.2.3.3. Farigliano, Piedmont, Italy

On the 3rd of October 2020 a storm affected the North of Italy, with heavy rain and strong winds causing great damages in the northern and western part of Piedmont region (Figure 5a) where the amount the heavy rainfall caused the overflow of several rivers and flooding of many areas. Especially, the overflow of the Sesia river caused interruption of roads, the collapse of a bridge and the flooding of several areas [33]. For the purpose of this research, flooding at Farigliano area was investigated (Figure 5b)

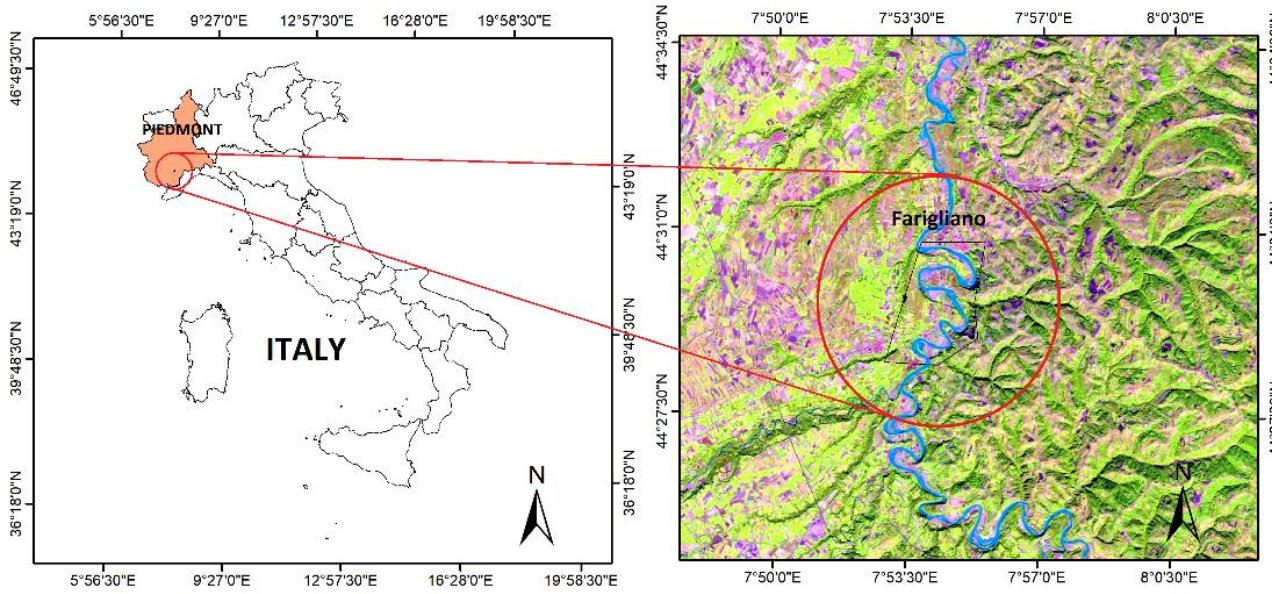

(**a**) (**b**)

Figure 5. The general view and location of (**a**) Piedmont Region in Northwest Italy, (**b**) Sessia River and the town of Farigliano.

1.2.4. Data

Sentinel-1A and Sentinel-1B launched by the ESA Copernicus program in April 2014 and 2016, respectively. Sentinel-1 satellites acquire data in four imaging modes: interferometric wide-swath (IW), strip map (SM) extra wideswath (EW) and wave (WV) mode [23]. SAR sensors illuminate the land surface with a range of view and incidence angles, which makes the radiometric correction necessary for the acquired imaged [34]. The GEE hosts Sentinel-1 Ground Range Detected (GRD) data acquired in EW, IW and SM modes, from which we used the IW acquisition mode for our study. Operational IW imagery are acquired at nominal 6-day intervals over Europe and nominal 12-day intervals over the rest of the Earth's surface, with higher repeat frequencies at higher latitudes and areas where targeted acquisitions are planned [8].

Sentinel-2 constellation with two satellites, S-2A and S-2B, launched in June 2015 and on March 2017, respectively, characterized by a revisit time of 5 days in Europe and 5 to 10 days in the rest of the world. Data are acquired in 12 bands with spatial resolution ranging from 10 to 60 m [35]. For our study, we focused on the RGB, NIR and SWIR bands (10 to 20 m spatial resolution).

The Copernicus Emergency Management Service (EMS) provides free of charge mapping service in cases of natural disasters throughout the world using satellite imagery and other geospatial data [33]. Copernicus EMS - Mapping service produces maps during all phases of the emergency management cycle in two temporal modes: (1) Rapid Mapping consists of the provision of geospatial information within hours or days from the activation; (2) Standardized mapping products are provided: e.g. to ascertain the situation before the event (reference product), to roughly identify and assess the most affected locations (first estimate product), assess the geographical extent of the event (delineation product) or to evaluate the intensity and scope of the damage resulting from the event (grading product) [33].

1.2.5. Results

1.2.5.1. Visual inspection

The RGB Natural Color (Red = Band 4; Green = Band 3; Blue = Band 2) (Fig. 6a), and the RGB Vegetation Analysis (Red = Band 6 SWIR 1; Green = Band 5 NIR; Blue = Band 4 Red) (Figure 5b) of the acquired image were generated to give the overall situation of Metaponto at the date of flood in December 2013. The visual inspection of Fig. 6 shows that great amount of sediment has entered the Gulf of Taranto.

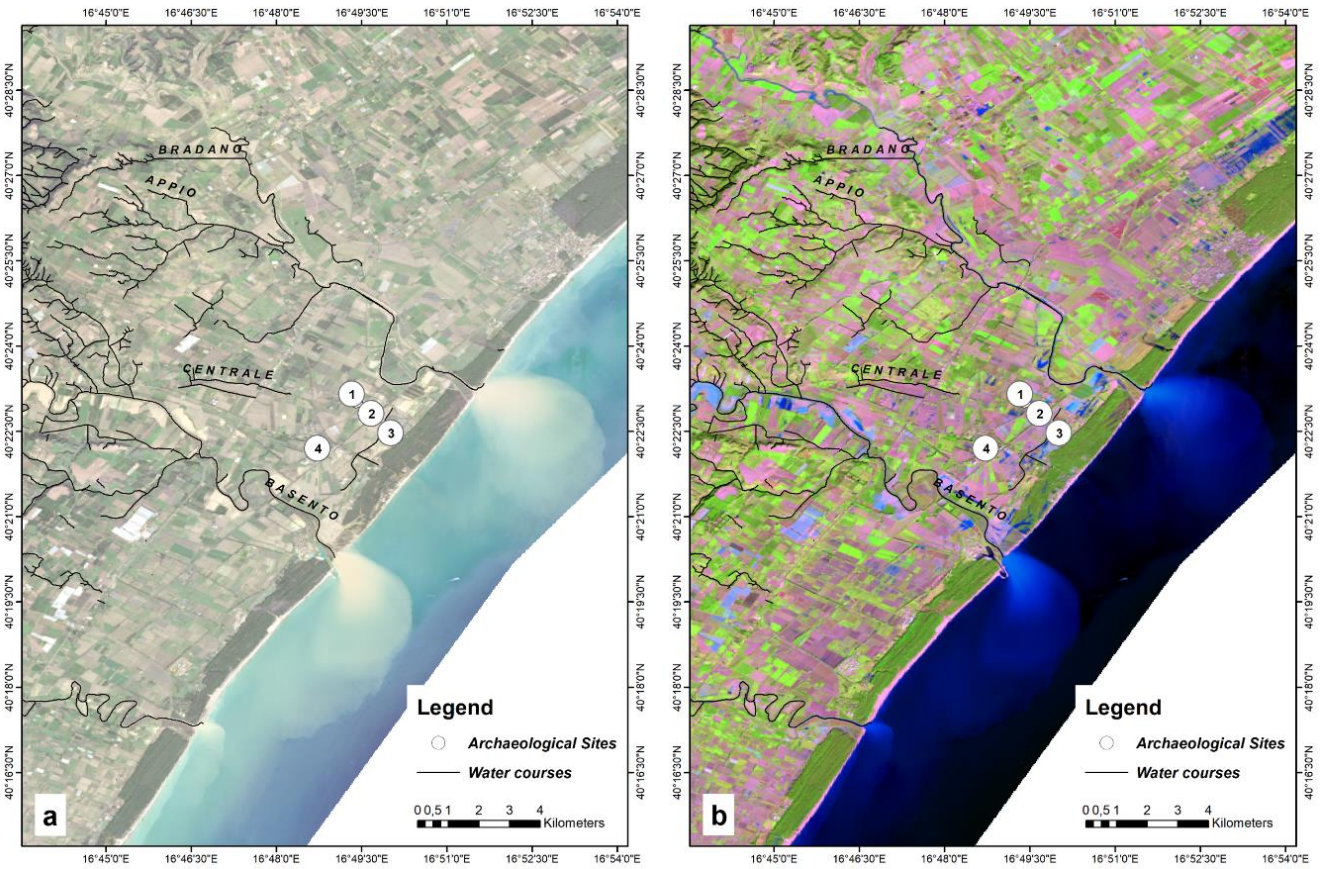

Figure 6. Localization of the Region of Interest. In background the RGB **(a)** Natural Color (Red = Band 4 Red; Green = Band 3 Green; Blue = Band 2 Blue) and **(b)** Vegetation Analysis (Red = Band 6 SWIR 1; Green = Band 5 NIR; Blue = Band 4 Red) of Landsat 8 C2 L2 Imagery data acquired on 6 December 2013. Archaeological Sites: 1. Metaponto excavation; 2. Castrum; 3. Ancient remains; 4. Castello Torremare.

For other study areas, Sentinet-2 natural-look RGB images (Band 4,3,2) of the study areas, with reasonable cloud coverage, were utilized to produce the time-lapse of flood evolution to identify the different stages of events (Fig. 7 and 8 for Shushtar and Farigliano, respectively). The visual inspection of Fig. 7 and 8 indicates that the maximum inundation happened on 2019-Apr-08 and 2010-Oct-03 for flood events in Shustar and Farigliano, respectively.

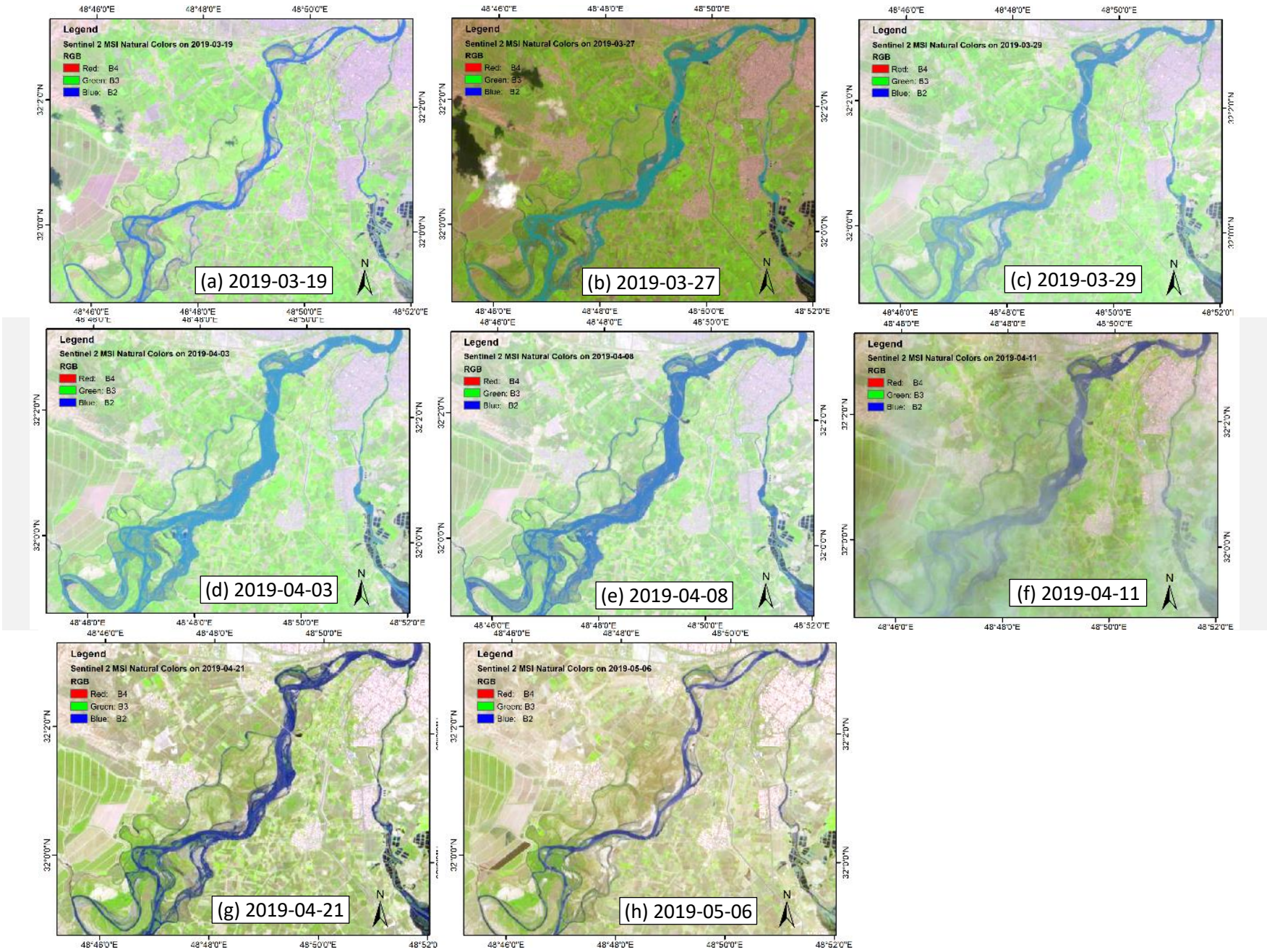

Figure 7. The time-lapse of the natural look images from Sentinel-2 for the study area Shustar, Khuzestan (Iran).

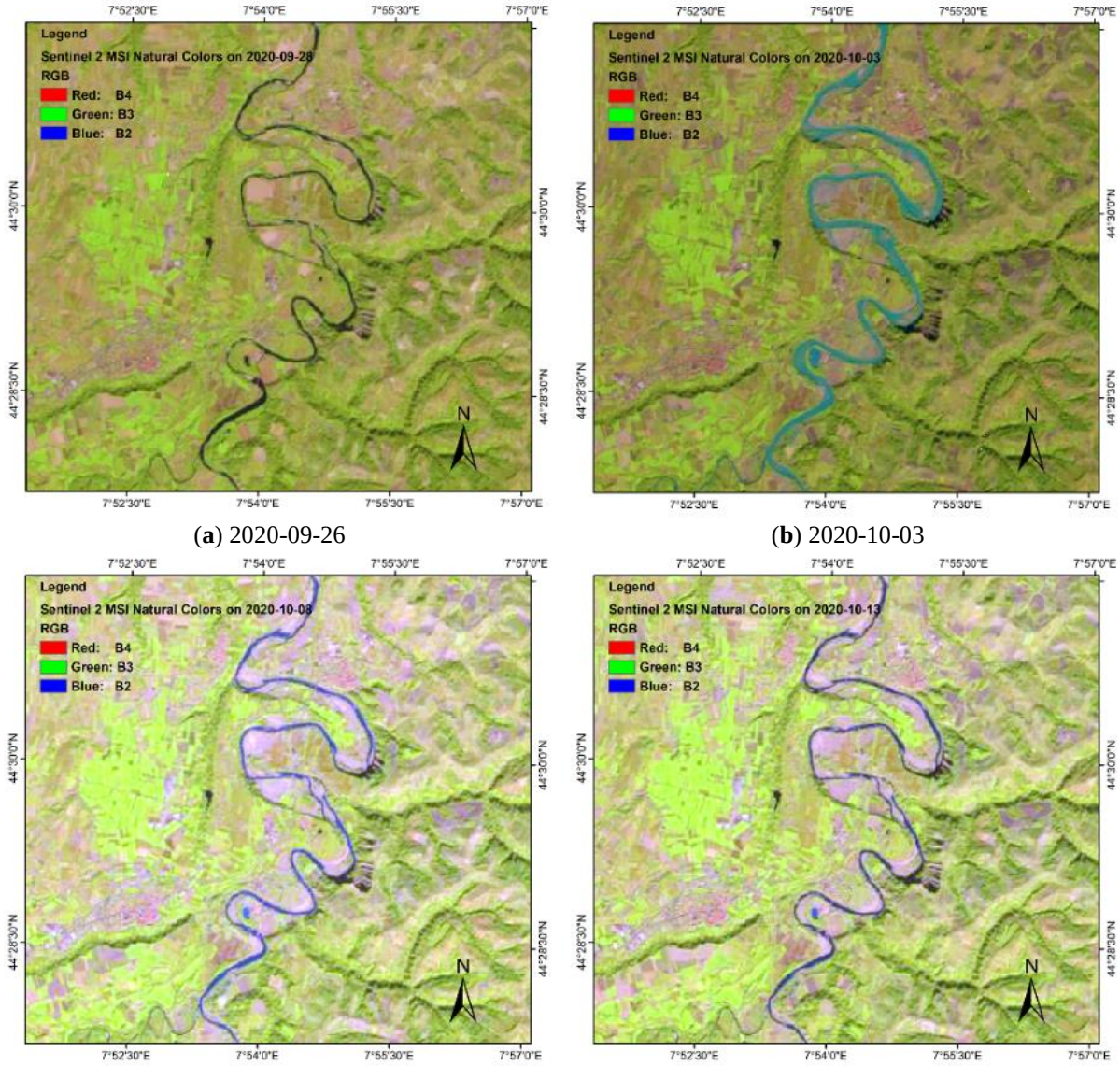

(**a**) 2020-09-26 (**b**) 2020-10-03

(**c**) 2020-10-08 (**d**) 2020-10-13

Figure 8. The time-lapse of the natural look images from Sentinel-2 for the study area Farigliano, Piedmont (Italy).

1.2.5.2. Spectral Index analysis

Figure 9 represents the raster maps of the Landsat 8 NDVI, MNDWI and NDWI indices for Metaponto study area relating to the December 2013 flood as generated by GEE code. Since the nearest image to the flood event from sentinel-2 were contaminated by clouds, the Landsat image was replaced for the purpose of this part of the study. According to Figure 9, MNDWI had the best performance to identify flooded areas in comparison with the Fig. 8. Thus, the flood map of the study area was generated by thresholding the raster histogram of Figure 9a into flooded and non-flooded categories (Figure 10). Also the results of Lavaca et al. [42] from the same flood were added to Figure 10 to evaluate the results. As can be seen in Figure 10, not only the flood map obtained from Landsat-8 MNDWI has a good consistency with those of Landsat-7 NDVI (Figure 10a) and MODIS and VIIRS RST-FLOOD algorithm (Figure 10b), but also it outperforms them considering the layout of the stream network and the spatial resolution of the maps (Figure 10c).

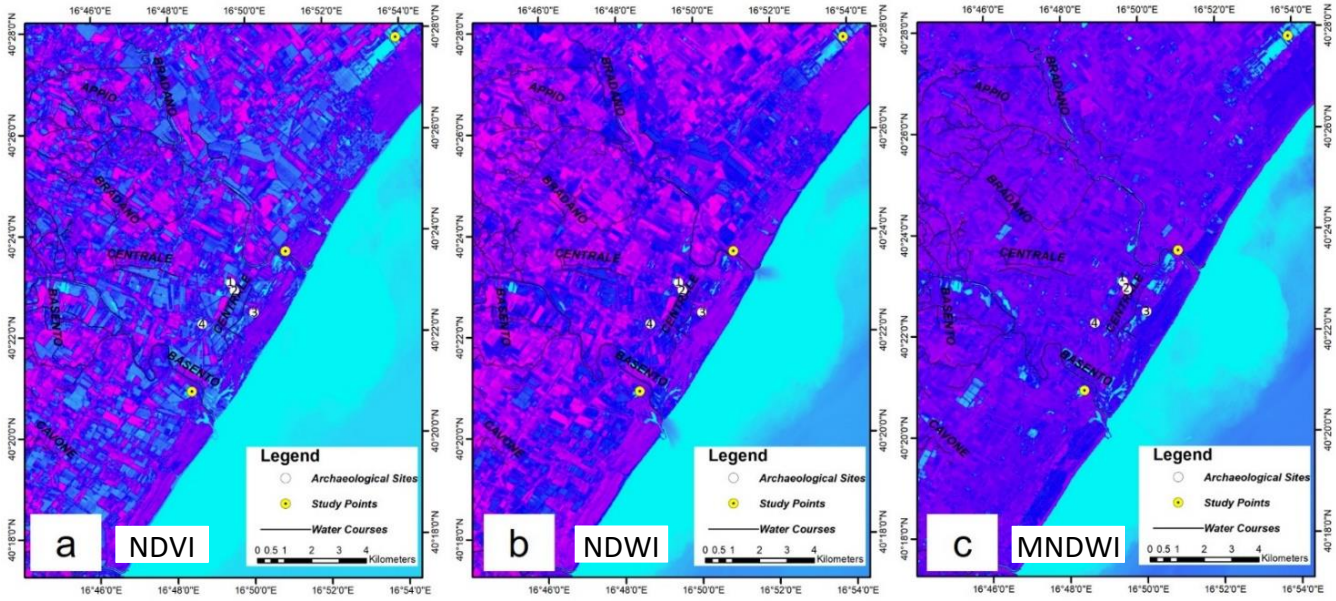

Figure 9. The raster maps of the (a) Landsat 8 NDVI, (b) NDWI and (c) MNDWI indices for the study area relating to the 1-3 December 2013 flood. Archaeological Sites: 1. Metaponto excavation; 2. Castrum; 3. Ancient remains; 4. Castello Torremare.

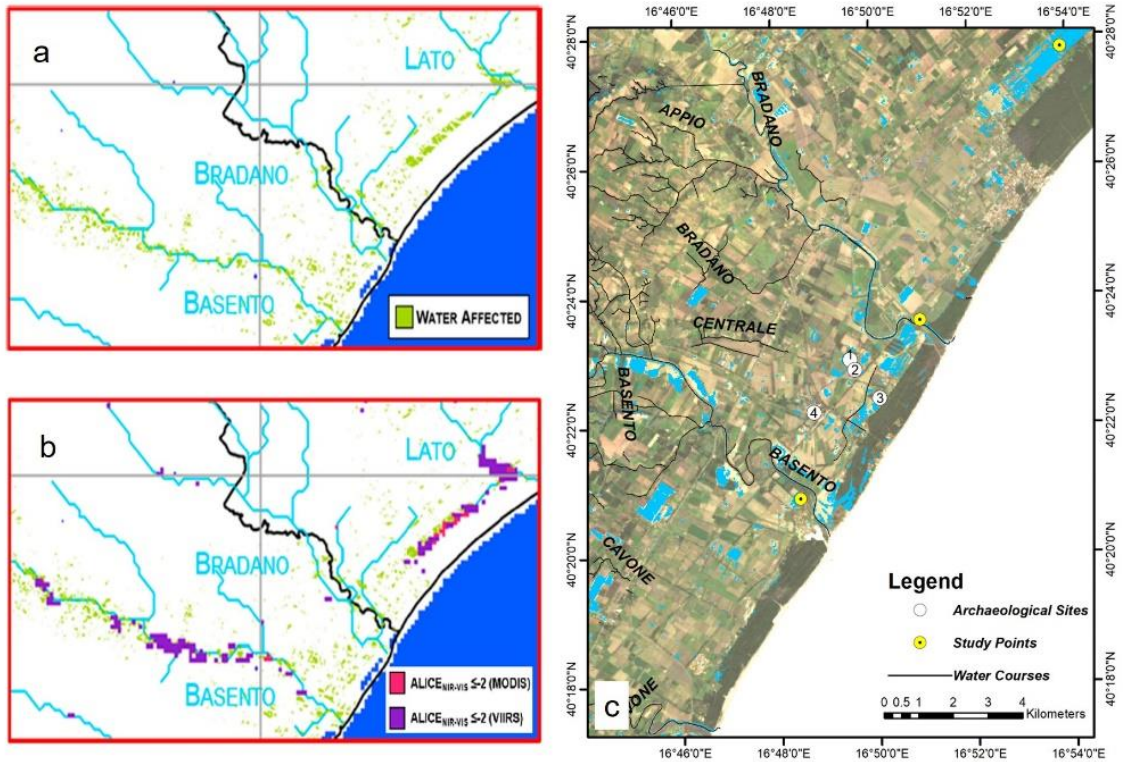

Figure 10. The flood map of the study area based on **(a)** thresholding the Landsat 7 NDVI raster on 5 December 2013; **(b)** anomalous pixels detected by RST-FLOOD algorithm on 5 December 2013 for MODIS (pink) and for VIIRS (violet); and **(c)** thresholding the Landsat 8 MNDWI raster on 6 December 2013. Figures 3a&b have been adopted from Lavaca et al. [42]. Archaeological Sites: 1. Metaponto excavation; 2. Castrum; 3. Ancient remains; 4. Castello Torremare.

For other study areas including Shushtar and Farigliano, the same multispectral indices but from Sentinel-2 data were generated using the "*normalized.Difference"* command in the GEE. Figure 11 depicts that these indices have a relatively good with the EMS reference flood maps in identifying water surfaces and inundated areas. Comparing NDWI maps in figure 11 with the natural looks in Fig. 7 and 8 reveals that despite having a higher spatial resolution, NDWI is more sensitive to urban smooth surfaces such as rooftops and bare soil surface being mistaken with the flooded areas.

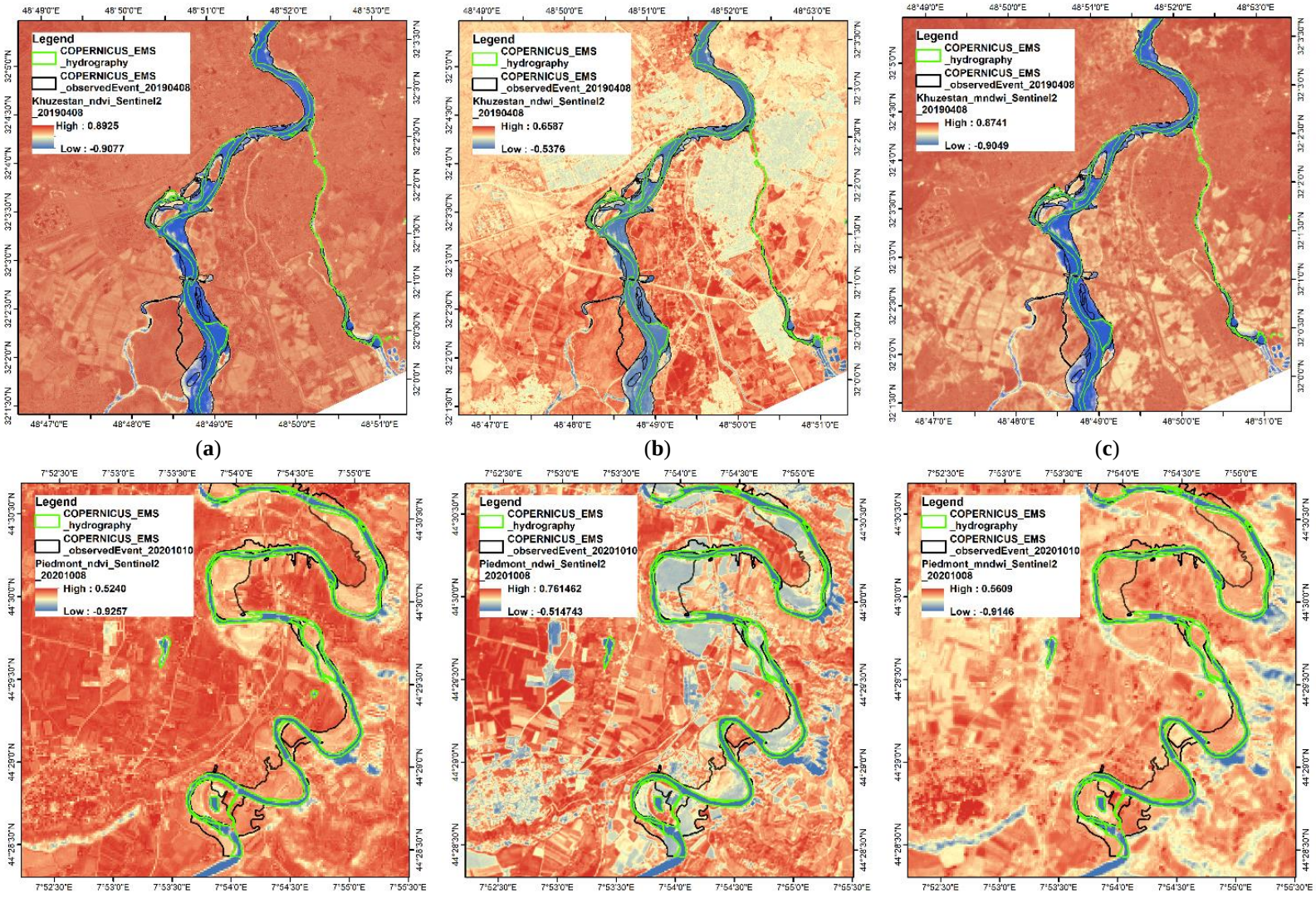

Figure 11. Sentinel-2 images of Shushtar, Iran (top) and Farigliano, Italy (bottom) were processed by different available water body indices using GEE. (a) and (e) NDVI, (b) and (f) NDWI, and (c) and (g) MNDWI. The normal river body and the observed event by the Copernicus EMS were also delineated by green and black polygons, respectively.

1.2.5.3. SAR backscattering change detection

Another method for detecting flooded areas with the Sentinel-1 SAR imagery is the classification of backscattering ratio between two images before and after the flood event using *"(after_image.divide(before_image)).lt(threshold)"* command in the GEE. Bentivenga et al. [41] studied a recent flood in Metaponto on 11 November 2019 with the Sentinel 1 SAR images that was not due to the overflow of the main streams, but rather to the failure of the reclamation channels. In this case, the flood event was investigated by both Sentinel 1 and 2 images to provide a better vision of the event. The NDWI map of the study area was generated by Sentinel-2 image on 11 November and pixels with the negative values were classified as flooded areas. Moreover, the difference in the VH band between the first Sentinel-1 image before and after the flood was calculated and pixels with the difference greater than 1.15 were identified as flooded areas (Figure 12).

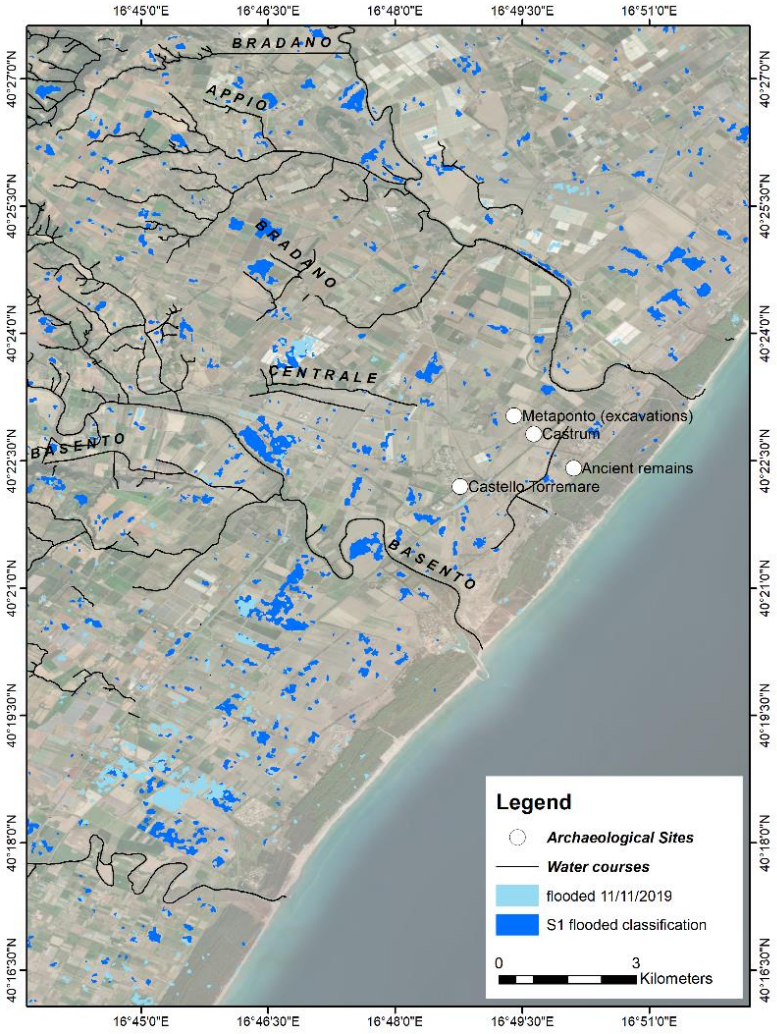

Figure 12. Sentinel-2 NDWI classification on 11/11/2019 (light blue) and Sentinel-1 before-and-after difference classification (dark blue). The image finds a useful comparison in [41, Figure 8].

For other study areas including Shushtar and Farigliano, the same procedure was applied for the Sentinel-1 SAR data and Figure 13 illustrates the results of SAR backscattering change detection for these study areas. Blue areas represent the flooded zones. Comparing the EMS standard flood maps (area delineated with the red line in Fig. 13) with the resulted SAR maps reveals that SAR data underestimate the flood extents specially in highly vegetated areas such as Piedmont, while the results in less vegetated areas such as Khuzestan is more consistent with the optical results and EMS maps.

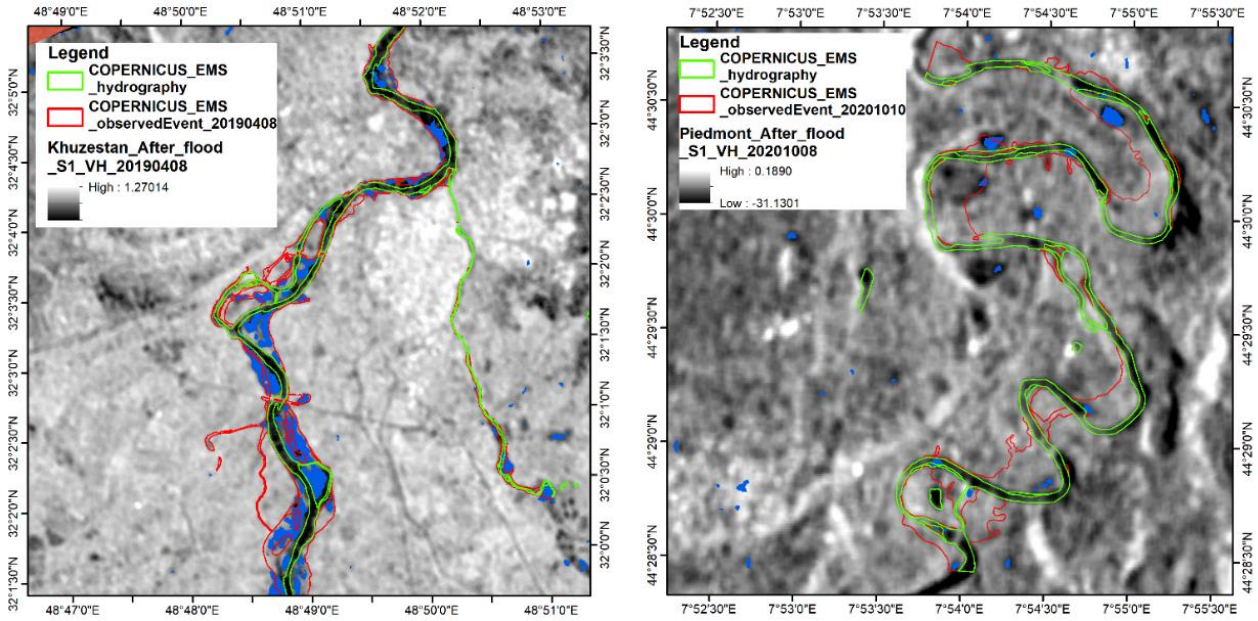

(**a**) (**b**)

Figure 13. Sentinel-1 SAR VH backscattering change detection results for (A) Shushtar, Iran; and (B) Farigliano, Italy. Blue areas represent the flooded zones

1.2.5.4. Supervised classification

In order to perform the supervised classification on the Sentinel-1 and Sentinel-2 imagery in the GEE platform, the Random Forest algorithm was employed using "*ee.Classifier.smileRandomForest()*" function and the classifications were trained based on the EMS maps. Sentinel-1 VV and VH bands, and all of the Sentinel-2 bands were introduced to GEE as the prediction bands. This selection of bands was in line with other studies (e.g. 7 and 38). Figures 14 represents the results of classification in Shustar and Farigliano study areas on the closest available Sentinel-1 image to the flood events regardless of the weather condition as opposed to closest cloud-free Sentinel-2 imagery. The overall accuracy based on a Confusion Matrix between the training points and validation points were also reported by "*ee.Classifier.smileRandomForest()*" function of GEE (table 3). Table 3 demonstrates that while Sentinel-2 provides flood maps with high accuracy in the cloud free conditions, Sentinel-1 is capable of producing acceptable results even in the cloudy conditions.

Table 3. Agreement statistics between GEE flood prediction maps and Copernicus EMS vector data layers for Shushtar (Iran) and Farigliano (Italy).

	Shustar, Khuzestan		**Farigliano, Piedmont**	
	Sentinel-1	Sentinel-2	Sentinel-1	Sentinel-2
Validation overall accuracy	0.813	0.980	0.718	0.846

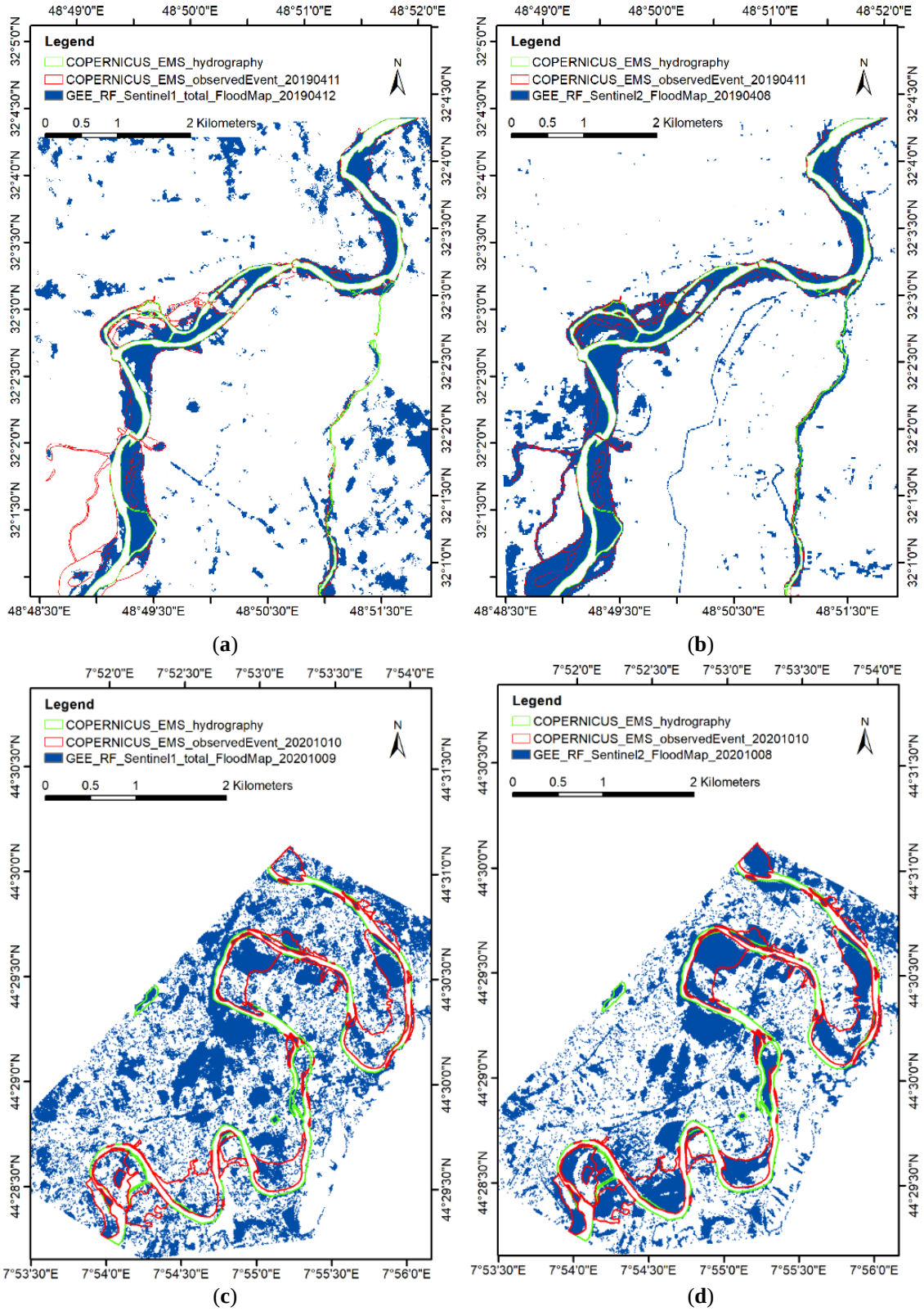

Figure 14. Results of Random Forest classification based on sentinel-1 (VV and VH bands) and Sentinel-2 (all bands) composite images for (a) and (b) Piedmont (Farigliano); and (c) and (d) Khuzestan (Shushtar), respectively.

1.2.5.5. Flood monitoring

After delineating the most apparent flooded areas in Metaponto according to Figures 10 and 12, the GEE was utilized to extract the variations of the Landsat-8 MNDWI values at five study points inside the flooded areas (Fig 10c) from 2013 to the present to investigate any apparent pattern in this parameter (Figure 15). The reason

behind using Landsat-8 imagery instead of Sentinel-2 in Metoponto was that it provided cloud free images around the period of our study flood.

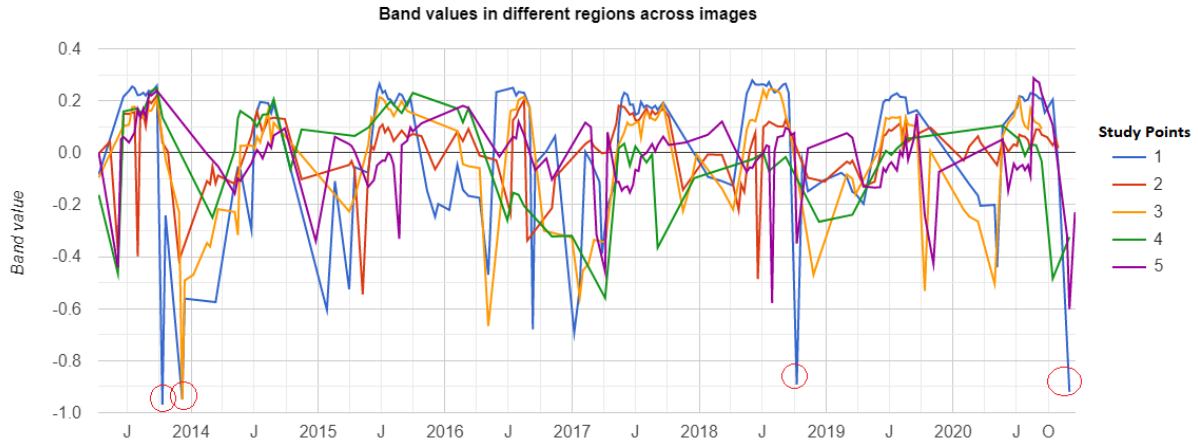

Figure 15. Time Series of the MNDWI in five study points which are prone to flooding using Landsat 8 images in the GEE.

Table 2 lists six major floods and their antecedent rainfalls in the Metaponto Plain since 2013. Comparing Figures 15 with the information in table 2 reveals that the dramatic drop in the MNDWI matches with the occurrence of the three floods with the highest 30-day antecedent rainfall (i.e. October 2013, November 2013, and November 2018). Other floods could have been detected, but they might have been omitted due to the lack of cloud free images, or their antecedent rainfalls were not big enough to inundate study points.

Table 2. Flood records in the Metaponto region along with their antecedent rainfalls that caused them. Adopted from [41].

Date	River Basin	Antecedent rainfall	
		1 day	30 days
6-8/10/2013	Bradano, Basento	122	139.8
30/11/2013 to 02/12/2013	Bradano, Basento, Cavone, Agri, Sinni	142	325
4-5/10/2014	Bradano, Basento, Cavone, Sinni	96.2	121.2
16-18/03/2016	Bradano, Basento, Cavone, Agri, Sinni	12.4	101.8
22-23/10/2018	Cavone, Agri, Sinni	20.8	239.2
11-12/11/2019	Bradano, Basento, Cavone, Agri, Sinni	37	51.8

According to Fig. 15, it can be assumed that values below -0.8 in the time-series of MNDWI can raise the alarm for detecting a flood event. Based on this assumption, it is also visible in Figure 15 that there might be another major flood in November 2020. Thus, the Landsat-8 RGB image on 30 Nov 2020 was investigated for the possible flood event and as can be seen in Figure 16a, signs of flooding are evident in the study area. Figure 16b also reveals flooded areas as identified by thresholding the Landsat-8 MNDWI on 30 Nov 2020 as well as Sentinel-1 before-and-after difference classification. Sentinel-2 cloud coverage during the flood did not permit to extract flooded areas.

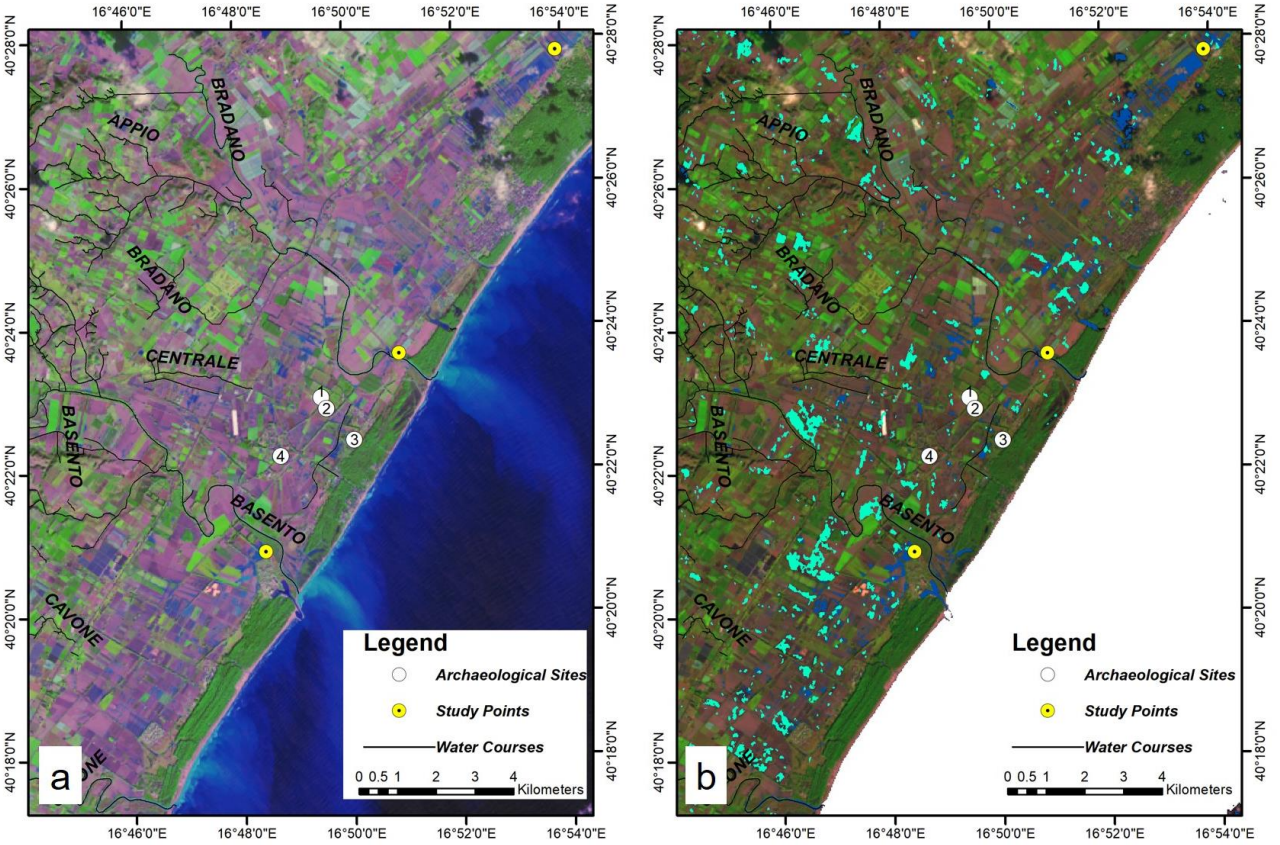

Figure 16. (a) Bands 6,5,4 RGB image of Landsat-8 image on 30 November 2020; and **(b)** flooded regions based on Landsat-8 MNDWI classification on 30 November 2020 (dark blue) and Sentinel-1 before-and-after difference classification (light blue). Archaeological Sites: 1. Metaponto excavation; 2. Castrum; 3. Ancient remains; 4. Castello Torremare.

For other study areas including Shushtar and Farigliano, a number of study points were also determined within the flood prone areas and the averaged time-series of Sentinel-1 VV and/or VH backscattering values as well as Sentinel-2 water spectral indices for that points were extracted in the GEE platform using "ui.Chart.image.seriesByRegion({imageCollection.select('water_index'),regions,reducer:ee.Reducer.mean()});" (Fig. 17). As mention before, the maximum inundation in Shustar and Farigliano happened on 2019-Apr-08 and 2010-Oct-03, respectively. Inspecting Fig.17 also reveals that the timeseries of Sentinel-1 VV and VH bands as well as MNDWI index calculated from Sentinel-2 RED and SWIR bands also recorded such events. By the beginning of floods, VV, VH and MNDWI started to decline until they reached to a Trough (or valley) at the day of maximum inundation. By receding water from the study points in the flooded areas, the above-mentioned parameters returned to their normal states. In general, it can be said that in the inundated areas there was a detectable signal which can be detected to set off potential flood alerts.

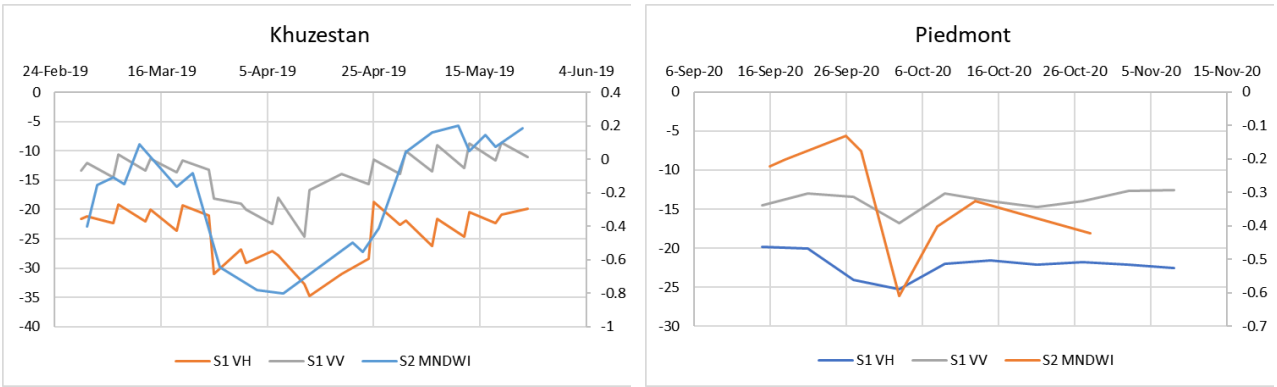

(**a**) (**b**)

Figure 17. time series of Sentinel-1 VV band, VH band, and Sentinel-2 MNDWI index during the floods.

1.2.6. Discussions

In this part of the study, we assessed the capabilities of the GEE for rapid flood mapping and monitoring in the near real-time applying supervised and unsupervised methods on the Sentinel-1 and Sentinel-2 data for the two recent flood events in Iran and Italy. This study highlights the benefits of cloud computing platforms like the GEE to allow for rapid analysis of satellite data in near real-time, in support of disaster monitoring and management activities. Using our algorithm on the GEE, we were able to produce flood maps shown to be highly similar to existing authenticated Copernicus EMS flood maps (84% overall accuracy), suggesting that this approach is highly suitable to operational and disaster management purposes. The flood maps were later manually refined with the help of ancillary data such as digital elevation models (DEMs), and constant water bodies.

The study points out some drawbacks of flood mapping based on the use of SAR and multispectral satellite data. In the latter case, the main limitation is represented by cloud cover affecting co-flood multispectral acquisitions. The presence of dense urban areas and forests affects both SAR and multispectral based flood mapping. High spatial resolution is also a key factor when mapping floods in dense urban areas, and it is one of the limitations of the free of charge satellite data approach. However, despite such drawbacks the use of freely available satellite data allowed us to map inundated areas with high accuracy for all study areas.

For future works, it is suggested to develop a Decision Support System (DSS) that integrates with the GEE cloud platform and other models and data sources for a user-friendly flood observing system. Such a system can provide relevant maps, alerts and statistics for flood emergencies.

1.2.7. Conclusion

The set of tools offered by Google Earth Engine is extremely useful and performing in the context of Remote Sensing analysis applied to the monitoring and management of risk in areas of natural and archaeological interest. The possibility of being able to integrate several data sets in a rather simple way, without having to employ hardware resources for storage, and hardware and software for computation, is definitely the greatest strength of this tool. In addition, this tool has proven to be versatile in many ways, as many as the possible fields of use, in multi-sensor/platform and multi-temporal analysis, adapting itself through simple JavaScript programming to several contexts and needs. Using combined data, as herein proposed, is possible to overcome the limits related to a single type of sensor (optical), in favor of a combined use with other sensors such as Synthetic Aperture Radar (SAR) [40, 44], whose data are implemented in the Google Earth Engine datasets. The utilization of GEE cloud platform also facilitated the implementation of different algorithms and analyses while removing the need for the prolonged steps of downloading and preprocessing the data. Moreover, as already tested in previous studies and herein proven, the methodology, once structured into a robust script, can be re-applied and scaled in different contexts and domains, making Google Earth Engine great for cross-platform analysis.

1.2.8. References

1. Hirabayashi, Y.; Mahendran, R.; Koirala, S.; Konoshima, L.; Yamazaki, D.; Watanabe, S.; Kim, H.; Kanae, S. Global flood risk under climate change. Nature Climate Change 2013, 3, 816-821.
2. Voigt, S.; Giulio-Tonolo, F.; Lyons, J.; Kučera, J.; Jones, B.; Schneiderhan, T.; Platzeck, G.; Kaku, K.; Hazarika, M.K.; Czaran, L. Global trends in satellite-based emergency mapping. Science 2016, 353, 247-252.
3. Xu, H. Modification of normalised difference water index (NDWI) to enhance open water features in remotely sensed imagery. International journal of remote sensing 2006, 27, 3025-3033.
4. Bryant, R.G.; Rainey, M. Investigation of flood inundation on playas within the Zone of Chotts, using a time-series of AVHRR. Remote Sensing of Environment 2002, 82, 360-375.
5. Crétaux, J.-F.; Bergé-Nguyen, M.; Leblanc, M.; Abarca Del Rio, R.; Delclaux, F.; Mognard, N.; Lion, C.; Pandey, R.K.; Tweed, S.; Calmant, S. Flood mapping inferred from remote sensing data. Int. Water Technol. J 2011, 1, 48-62.
6. Fattore, C.; Abate, N.; Faridani, F.; Masini, N.; Lasaponara, R. Google earth engine as multi-sensor open-source tool for supporting the preservation of archaeological areas: the case study of flood and fire mapping in Metaponto, Italy. Sensors 2021, 21, 1791.

7. Pham-Duc, B.; Prigent, C.; Aires, F. Surface water monitoring within Cambodia and the Vietnamese Mekong Delta over a year, with Sentinel-1 SAR observations. Water 2017, 9, 366.
8. DeVries, B.; Huang, C.; Armston, J.; Huang, W.; Jones, J.W.; Lang, M.W. Rapid and robust monitoring of flood events using Sentinel-1 and Landsat data on the Google Earth Engine. Remote Sensing of Environment 2020, 240, 111664.
9. Chini, M.; Hostache, R.; Giustarini, L.; Matgen, P. A hierarchical split-based approach for parametric thresholding of SAR images: Flood inundation as a test case. IEEE Transactions on Geoscience and Remote Sensing 2017, 55, 6975-6988.
10. Pulvirenti, L.; Pierdicca, N.; Chini, M.; Guerriero, L. An algorithm for operational flood mapping from Synthetic Aperture Radar (SAR) data using fuzzy logic. Natural Hazards and Earth System Sciences 2011, 11, 529-540.
11. Twele, A.; Cao, W.; Plank, S.; Martinis, S. Sentinel-1-based flood mapping: a fully automated processing chain. International Journal of Remote Sensing 2016, 37, 2990-3004.
12. Amitrano, D.; Di Martino, G.; Iodice, A.; Riccio, D.; Ruello, G. Unsupervised rapid flood mapping using Sentinel-1 GRD SAR images. IEEE Transactions on Geoscience and Remote Sensing 2018, 56, 3290-3299.
13. Clement, M.A.; Kilsby, C.; Moore, P. Multi-temporal synthetic aperture radar flood mapping using change detection. Journal of Flood Risk Management 2018, 11, 152-168.
14. Lu, J.; Li, J.; Chen, G.; Zhao, L.; Xiong, B.; Kuang, G. Improving pixel-based change detection accuracy using an object-based approach in multitemporal SAR flood images. IEEE journal of selected topics in applied earth observations and remote sensing 2015, 8, 3486-3496.
15. Hostache, R.; Matgen, P.; Wagner, W. Change detection approaches for flood extent mapping: How to select the most adequate reference image from online archives? International journal of applied earth observation and geoinformation 2012, 19, 205-213.
16. Long, S.; Fatoyinbo, T.E.; Policelli, F. Flood extent mapping for Namibia using change detection and thresholding with SAR. Environmental Research Letters 2014, 9, 035002.
17. Plank, S.; Jüssi, M.; Martinis, S.; Twele, A. Mapping of flooded vegetation by means of polarimetric Sentinel-1 and ALOS-2/PALSAR-2 imagery. International Journal of Remote Sensing 2017, 38, 3831-3850.
18. Giustarini, L.; Matgen, P.; Hostache, R.; Montanari, M.; Plaza, D.; Pauwels, V.; De Lannoy, G.; Keyser, R.D.; Pfister, L.; Hoffmann, L. Assimilating SAR-derived water level data into a hydraulic model: a case study. Hydrology and Earth System Sciences 2011, 15, 2349-2365.
19. Mason, D.C.; Giustarini, L.; Garcia-Pintado, J.; Cloke, H.L. Detection of flooded urban areas in high resolution Synthetic Aperture Radar images using double scattering. International Journal of Applied Earth Observation and Geoinformation 2014, 28, 150-159.
20. Brakenridge, G.R.; Knox, J.C.; Paylor, E.D.; Magilligan, F.J. Radar remote sensing aids study of the great flood of 1993. Eos, Transactions American Geophysical Union 1994, 75, 521-527.
21. Huang, C.; Nguyen, B.D.; Zhang, S.; Cao, S.; Wagner, W. A comparison of terrain indices toward their ability in assisting surface water mapping from Sentinel-1 data. ISPRS International Journal of Geo-Information 2017, 6, 140.
22. Wulder, M.A.; Masek, J.G.; Cohen, W.B.; Loveland, T.R.; Woodcock, C.E. Opening the archive: How free data has enabled the science and monitoring promise of Landsat. Remote Sensing of Environment 2012, 122, 2-10.
23. Torres, R.; Snoeij, P.; Geudtner, D.; Bibby, D.; Davidson, M.; Attema, E.; Potin, P.; Rommen, B.; Floury, N.; Brown, M. GMES Sentinel-1 mission. Remote Sensing of Environment 2012, 120, 9-24.
24. Lewis, A.; Lymburner, L.; Purss, M.B.; Brooke, B.; Evans, B.; Ip, A.; Dekker, A.G.; Irons, J.R.; Minchin, S.; Mueller, N. Rapid, high-resolution detection of environmental change over continental scales from satellite data–the Earth Observation Data Cube. International Journal of Digital Earth 2016, 9, 106-111.
25. Gorelick, N.; Hancher, M.; Dixon, M.; Ilyushchenko, S.; Thau, D.; Moore, R. Google Earth Engine: Planetary-scale geospatial analysis for everyone. Remote sensing of Environment 2017, 202, 18-27.
26. Donchyts, G.; Baart, F.; Winsemius, H.; Gorelick, N.; Kwadijk, J.; Van De Giesen, N. Earth's surface water change over the past 30 years. Nature Climate Change 2016, 6, 810-813.
27. Pekel, J.-F.; Cottam, A.; Gorelick, N.; Belward, A.S. High-resolution mapping of global surface water and its long-term changes. Nature 2016, 540, 418-422.
28. Tang, Z.; Li, Y.; Gu, Y.; Jiang, W.; Xue, Y.; Hu, Q.; LaGrange, T.; Bishop, A.; Drahota, J.; Li, R. Assessing Nebraska playa wetland inundation status during 1985–2015 using Landsat data and Google Earth Engine. Environmental monitoring and assessment 2016, 188, 1-14.
29. Hansen, M.; Potapov, P.; Moore, R.; Hancher, M.; Turubanova, S.; Tyukavina, A.; Thau, D.; Stehman, S.; Goetz, S.; Loveland, T. Townshend. JRG, 2013. High-Resolution Global Maps of 21st-Century Forest Cover Change. Science 2013, 342, 850-853.
30. Johansen, K.; Phinn, S.; Taylor, M. Mapping woody vegetation clearing in Queensland, Australia from Landsat imagery using the Google Earth Engine. Remote Sensing Applications: Society and Environment 2015, 1, 36-49.
31. Padarian, J.; Minasny, B.; McBratney, A.B. Using Google's cloud-based platform for digital soil mapping. Computers & geosciences 2015, 83, 80-88.

32. Xiong, J.; Thenkabail, P.S.; Gumma, M.K.; Teluguntla, P.; Poehnelt, J.; Congalton, R.G.; Yadav, K.; Thau, D. Automated cropland mapping of continental Africa using Google Earth Engine cloud computing. ISPRS Journal of Photogrammetry and Remote Sensing 2017, 126, 225-244.
33. Copernicus Emergency Management Service. Availabe online: https://emergency.copernicus.eu/ (accessed on May 20).
34. Small, D. Flattening gamma: Radiometric terrain correction for SAR imagery. IEEE Transactions on Geoscience and Remote Sensing 2011, 49, 3081-3093.
35. Huang, M.; Jin, S. Rapid flood mapping and evaluation with a supervised classifier and change detection in shouguang using sentinel-1 sar and sentinel-2 optical data. Remote Sensing 2020, 12, 2073.
36. Lacava, T.; Ciancia, E.; Faruolo, M.; Pergola, N.; Satriano, V.; Tramutoli, V. Analyzing the December 2013 Metaponto Plain (Southern Italy) Flood Event by Integrating Optical Sensors Satellite Data. Hydrology 2018, 5, 43.
37. Wang, Z.; Lai, C.; Chen, X.; Yang, B.; Zhao, S.; Bai, X. Flood hazard risk assessment model based on random forest. Journal of Hydrology 2015, 527, 1130-1141.
38. Notti, D.; Giordan, D.; Caló, F.; Pepe, A.; Zucca, F.; Galve, J.P. Potential and limitations of open satellite data for flood mapping. Remote sensing 2018, 10, 1673.
39. Lee, J.S.H.; Wich, S.; Widayati, A.; Koh, L.P. Detecting industrial oil palm plantations on Landsat images with Google Earth Engine. Remote Sensing Applications: Society and Environment 2016, 4, 219-224.
40. Lasaponara, R.; Tucci, B.; Ghermandi, L. On the Use of Satellite Sentinel 2 Data for Automatic Mapping of Burnt Areas and Burn Severity. Sustainability 2018, 10, 3889.
41. Bentivenga, M.; Giano, S.I.; Piccarreta, M. Recent Increase of Flood Frequency in the Ionian Belt of Basilicata Region, Southern Italy: Human or Climatic Changes? Water, 2020, 12, 2062. https://doi.org/10.3390/w12072062.
42. Lacava, T.; Ciancia, E.; Faruolo, M.; Pergola, N.; Satriano, V.; Tramutoli, V. Analyzing the December 2013 Metaponto Plain (Southern Italy) Flood Event by Integrating Optical Sensors Satellite Data. Hydrology, 2018, 5, 43.
43. Lacava, T.; Ciancia, E.; Faruolo, M.; Pergola, N.; Satriano, V.; Tramutoli, V. On the potential of RST-FLOOD on visible infrared imaging radiometer suite data for flooded areas detection. Remote Sensing 2019, 11, 598.
44. De Luca, G.; Modica, G.; Fattore, C.; Lasaponara, R. Unsupervised Bruned Area Mapping in a Protected Natural Site. An Approach Using SAR Sentinel-1 Data and K-mean Algorithm. In Computational Science and Its Applications – ICCSA 2020. 20th International Conference, Cagliari, Italy, July 1–4, 2020, Proceedings, Part V,

Chapter (2): Soil water balance modeling

Part 1. Soil Moisture Estimation Using Physical Models and Downscaled RS Data

2.1.1. Introduction

Spatiotemporal distribution of root zone soil moisture (RZSM) across massive areas of land significantly contributes to lots of meteorological, hydrological, and agricultural applications [1,2]. Moreover, RZSM estimation at different spatiotemporal scales has a substantial role in strategic water resources management [3]. RZSM is a key storage parameter governing mass and energy partitioning associated with runoff and evapotranspiration (ET) [4]. The temporal evolution and spatial distribution of RZSM are affected by land-use, precipitation, soil texture, topography, and various meteorological variables [3].

Having gathered in the field, soil moisture (SM) measurements—typically known as in situ measurements—can be generally retrieved from low- or high-density networks of point measurements. To determine network density, the amount and assembly of tools, project budget, and study area should be taken into account [5]. Pointwise-scale SM measurements are conducted using ground-based SM methods. These measurements fail to demonstrate SM values for adjacent areas due to the large SM spatial heterogeneity on a vast array of scales (e.g., [6–8]). Likewise, large-scale ground-based SSM extraction through geostatistical methods is not suitable due to the large spatial heterogeneity. On the other hand, there are yet no dense SM-monitoring networks in many large areas. Therefore, SM measurement on different scales with ground-based instruments is still challenging.

Recent technological and theoretical advancements have paved the way for using remote sensing techniques in measuring SM content. Active and passive microwave observations have been widely used to estimate SM (e.g., [9–11]) and the SSM products are freely available for many applications. Table 1 summarizes the specifications of some of the sensors providing remotely sensed SM products [12,13].

Table 1. Active and passive soil moisture products.

Website	Spatial Resolution (km-)	Temporal Resolution (Day)	Product Level/Version	Space Agency	Platform	Type	Sensor
https://smap.jpl.nasa.gov/ (accessed on 11-Apr-2018).	3 (Active), 36 (Passive)	1	L3	NASA	SMAP	Passive	SMAP
http://www.esa.int/Our_Activities/ accessed on 11-Apr-2018)	40	1	L2/V6	ESA	SMOS	Passive	MIRAS
https://nsidc.org/data/amsre accessed on 11-Apr-2018)	25	1	L3/V2	NASA, JAXA	AQUA	Passive	AMSR-E
https://hydro1.gesdisc.eosdis.nasa.gov/ accessed on 11-Apr-2018)	25	1	L3/V1	NASA, JAXA	GCOM-W1	Passive	AMSR2
https://trmm.gsfc.nasa.gov/ accessed on 11-Apr-2018)	25	1	L2/V1	NASA, JAXA	TRMM	Passive	TMI
https://www.ipf.tuwien.ac.at/ accessed on 11-Apr-2018)	25.5	1	L2	EUMETSAT, ESA	METOP	Active	ASCAT
https://podaac.jpl.nasa.gov/SSMI accessed on 11-Apr-2018)	25	1	-	NASA	DMSP	Passive	SSM/I

Satellite-derived remotely sensed SSM products have their own advantages, including the accessibility of global-scale measurements at a continuous spatiotemporal resolution (STRs). Nevertheless, satellite-based products are currently accessible at low spatial resolutions, rendering them useless for small-scale agricultural applications and hydrologic models [14,15]. The satellite-derived product validation process is severely restricted in the presence of ground-based networks. Recently, research has focused on improving the estimated SSM of satellite-derived products by applying various algorithms connecting SSM with variables like brightness temperature, precipitation, vegetation, and so on [2,15–18]. The majority of techniques applied to derive high-resolution SM from synergies between microwave and optical observations rest upon triangular and trapezoidal approaches. [18,19] proposed an empirical polynomial fitting downscaling approach based on the frequently used triangular feature space formed by surface temperature (Ts) and vegetation index (VI). Here, high spatial resolutions are expressed as a polynomial function of land-surface temperature (LST),

Normalized Difference of Vegetation Index (NDVI), and opticothermal data-derived surface albedo as a region/climate conditions-specific regression formula. The polynomial fitting downscaling approach was employed to downscale SM and ocean salinity (SMOS), AMSR-E SM with high-resolution surface variables from Meteosat second-generation spinning enhanced visible and infrared imager (MSG-SEVIRI) or moderate resolution imaging spectroradiometer (MODIS) observations (see, for example, [20–24]).

Microwave sensor-derived SM data are immediately associated with the surface soil layer (0.2 cm to 5 cm) [25,26]. However, the largest part of the energy and water budgets of an ecosystem depends heavily on the spatial distribution of RZSM. Examining the correlation between SSM and RZSM in various studies reveal that RZSM is a function of SSM [27–29]. It has been particularly challenging to delineate the analytical relationships between SM and SSM in lower soil layers (see, for example, [30–33]), requiring further investigation. Studies have been conducted on how RZSM is estimated from SSM [34–37]. The presented methods involve simple statistical relationships with physically based methods. They require a series of experimental parameters alterable with soil type and vegetation. Here, soil profile moisture is estimated by assuming the conditions of a hydraulic balance between momentary SSM and soil profile moisture [37,38].

By solving a simple water balance equation for arid and semi-arid zones, [37] developed a soil moisture analytical relationship (SMAR) model to express the relationship between RZSM and SSM. The results of implementing the SMAR model on measuring SM at different depths indicated that this model could predict RZSM on both local and regional scales [29,37,39]. SSM is one of the main parameters in the SMAR model, which can use satellite-based SSM data to estimate RZSM [29,39]. By applying remotely sensed SSM TRMM-TMI products (with coarse resolution 25 km), ref. [39] evaluated the estimated RZSM using the SMAR model at several stations in North America. Although satellite-based SSM products represent large-area spatial mean and assign the data to a specific point therein, it could not be effective despite being successful in some cases. They proposed in their study to increase the resolution using downscaling techniques [39].

The spatiotemporal accessibility and accuracy of SSM and RZSM measurements are significant components to obtain optimal results in a variety of applications. There are also extremely restricted resources accessible to reclaim accurate SM measurements in the Rafsanjan plain (RP). Thus, this part of the study will assess AMSR2 data quality using REC-P55 SM sensors manufactured by Ansari and Hassanpour [43] and apply a downscaling approach to better characterize satellite-derived SSM when traveling above the study area (Rafsanjan Plain). The performance of this method will be evaluated based on the differences between ground-based and satellite-derived SSM measurements. The downscaling method used consists of a simple linear equation that correlates AMSR2 SM with three parameters retrieved from MODIS: Albedo, LST, and normalized difference vegetation index (NDVI). Afterwards, to estimate RZSM, the downscaled SSM values will be utilized in the SMAR model and the results will be compared with the measured data. At the end, it can be said that the purpose of this part of the study was to provide a methodology to implement the downscaled SSM values to prepare soil profile maps at 1-km resolution in a study area.

At the end, a summary of the established and emerging soil moisture retrieval methods as well as the scientific challenges seem necessary to understand the milestones in this field of study. According to a latest review, the state-of-the-art topics can be summarized into five items [2]:

1. VIS/NIR, TIR, and microwave are currently the three main data sources for global SSM monitoring. The VIS/NIR and TIR data have higher spatial resolution and can easily be affected by clouds, while microwave data have lower spatial resolution and can provide all-weather data coverage. To overcome the gaps between these sources of data, the synergic multi-band SSM retrievals should be considered.
2. Considerable efforts have been made in the retrieval of two Land Surface Temperature (LST) and SSM using passive microwave observations and auxiliary data. However, SSM and LST are codependent making the retrieval process difficult. Moreover, obtaining accurate auxiliary information such as meteorological parameters and soil texture is difficult due to clear-sky dependency and low spatial resolution, respectively. To solve this problem, it is essential to simultaneously retrieve LST and SSM from only passive microwave data to reduce the number of unknown parameters and make the retrieval independent of auxiliary information.
3. The target accuracy of RMSE of 0.04 m^3/m^3 between the satellite and measured SSM data has been the criterion for validating the SSM products, however, scientists suggested that distinguished target accuracies should be determined for different combination of surface moisture status, soil texture, and vegetation coverage.
4. In order to validate remotely sensed SSM data, in situ SSM measurements with a fixed depth of 5 cm are frequently used. However, VIS/NIR and microwave data can reflect SSM with only a few millimeters and centimeters, respectively, mostly depending on SSM content within the soil column and frequencies used

for detecting SSM. Therefore, it seems that currently there is no good way to solve the contradiction of sensing depth, however, post-processing steps (e.g., assimilation technology and the entropy theory) can mitigate this problem.

5. The estimation of RZSM from satellite SSM has been increasingly proposed by a number of investigations. The possible approaches for obtaining such data are (a) assimilating microwave SSM data into land surface models; (b) exponential filter and the analytical relationship between RZSM and SSM; and (c) using the P-band SAR with much deeper penetration depth due to its longer wavelength. However, satellite SSM accuracy and soil texture distribution are among the great challenges to obtain RZSM at present.

2.1.2. Methodology

2.1.2.1. AMSR2 SSM Downscaling

The SSM data are one of the most important input parameters to be used in the RZSM estimation model, though it is affected by several factors, such as daily rainfall, impermeable areas, land-use, soil temperature and type, and vegetation density, introducing high variability even in small scales. Thus, any coarse resolution SSM data (>1 km) is not expected to represent variability of this parameter in small-scale application. Downscaling generally aims to set up either a physically based model or a statistical correlation between fine-scale auxiliary variables and coarse-scale SM [44]. Previous studies proved that there is a correlation between the SSM, topographic/vegetation characteristics, and soil properties [45,46]. This information is applicable during downscaling because the assessment of the relationships between SSM and for example, soil texture and topography, typically demands comprehensive observations. The approach below was adopted to enhance satellite-derived continuous spatiotemporal SSM measurements over the Rafsanjan Plain. The downscaling method used here was initially released by [19] and has been implemented formerly by [47]. Based on this method, remotely sensed SSM retrieved from AMSR2 at a 25 km spatial resolution could be downscaled to a 1 km spatial resolution by utilizing a simple linear equation in accordance with parameters estimated using a regression model founded on three physical properties (i.e., albedo, LST, and NDVI) at a MODIS-retrieved 1 km spatial resolution. The downscaling technique with respect to the above-mentioned triple parameters is expressed by Equation (1) [19]:

$$\theta_s = \sum_{i=0}^{i=n} \sum_{j=0}^{j=n} \sum_{k=0}^{k=n} a_{ijk} V^i T^j A^k \quad (1)$$

Setting the number of explanatory variables to 1 in Equation (1) yield:

$$\theta_s = a_{000} + a_{100}V + a_{010}T + a_{001}\mathrm{A} + a_{110}VT + a_{101}VA + a_{011}TA \quad (2)$$

where a_{ijk} parameters represent the correlation between satellite-derived coarse-resolution SSM product and fine-resolution downscaled SSM product. They can be measured using the multiple linear regression (MLR) model, comparing coarse-resolution SSM estimates and aggregate values of physical properties. A, T, and V represent albedo, LST, and NDVI, respectively. Each of the parameters was up-scaled to correspond toAMSR2 at a 25 km spatial resolution as follows [19]:

$$V_{25km} = \frac{\sum_{i=1}^{n}\sum_{j=1}^{m} V_{i,j}}{mn} \; ; T_{25km} = \frac{\sum_{i=1}^{n}\sum_{j=1}^{m} T_{i,j}}{mn} \; ; \; A_{25km} = \frac{\sum_{i=1}^{n}\sum_{j=1}^{m} A_{i,j}}{mn} \quad (3)$$

where 25 km denotes the resolution at which upscaling of physical parameters is performed, m denotes the value for the *i*th column of the grid with a 1 km spatial resolution within the 25 km spatial resolution and n denotes the value for the *j*th row of the grid with a 1 km spatial resolution within the 25 km spatial resolution.

2.1.2.2. SMAR Model

Based on soil physical properties, the soil moisture analytical relationship (SMAR) model correlates between SSM and RZSM. SMAR assumes two layers for the soil: (1) a surface layer (a few centimeters deep, seen as equivalent to retrieval depth of satellite-based SSM product), and (2) a layer below the surface layer extending to the vegetation rooting depth [37]. The only water mass exchange between the aforesaid layers is infiltration, with other processes, including the capillary rise and lateral flow, assumed insignificant. Equation (4) was proposed by [37], describing the instantaneous infiltration flux from the upper to the bottom layer.

$$n_1 Lr_1 I(t) = n_1 Lr_1 I[s_1(t), t] = n_1 Lr_1 \begin{cases} (s_1(t) - s_{c1}), s_1(t) \geq s_{c1} \\ 0\ , s_1(t) \geq s_{c1} \end{cases} \quad (4)$$

In the above equation, I (t) [–] represents the amount of saturated soil penetrating the lower layer, n_1 [–] represents top soil porosity, *Lr1* (L) represents top soil depth, $s_1\left(\frac{\theta_{top}}{n_1}\right)[-]$ represents relative saturation of soil in the first layer, and sc1 represents relative saturation at topsoil field capacity. SSM needs to be taken as referred to the first 5 to 10 cm of soil. Even though the majority of satellite sensors fail to see deeper than a few centimeters, it can be reasonably assumed that these measures can represent the dynamics of a ≈ 5–10 cm surface layer [37]. The depth of surface layer in the SMAR model should not be less than 5 cm, otherwise the model might underestimate the infiltration and face numerical problems. While most satellite sensors provide information about soil water content no deeper than 0–5 cm of the top soil, a number of studies proved that satellite products can capture the required SSM dynamics for the surface layer of SMAR model [29,39,48–50].

By defining $x_2 = (s_2 - s_{w2})/(1 - s_{w2})$ as the effective relative saturation at second layer of soil and $\omega_0 = (1 - s_{w2})n_2 Zr_2$ as the soil water storage, the SMAR soil water balance is described as:

$$(1 - s_{w2})n_2 Zr_2 \frac{dx_2(t)}{dt} = n_1 Zr_1 y(t) - V_2 x_2(t) \quad (5)$$

where s_2 [–] is current relative saturation, s_{w2} [–] relative saturation at wilting point, n_2 [–] soil porosity, Zr_2 [L] second layer depth, V_2 [$L\,T^{-1}$] soil water loss coefficient (both evapotranspiration and percolation losses), and x_2 [–] effective relative soil saturation of the second soil layer. The second term of the right side of the Equation (5) represents a linear soil water loss function where soil water loss would be linearly reduced from a maximum value at the saturation point to zero at the wilting point. We can simplify Equation (5) by standardized coefficients:

$$a = \frac{V_2}{(1 - s_{w2})n_2 Lr_2}\ , b = \frac{n_1 Lr_1}{(1 - s_{w2})n_2 Lr_2}\ (6) \quad (6)$$

where $s_{w2}[-]$ denotes relative saturation of soil in the second layer at wilting point (WP), $n_2[-]$ denotes porosity of the soil in the second layer, $Lr_2[-]$ denotes the depth of soil in the second layer and $V_2[LT^{-1}]$ denotes SM loss coefficient justifying percolation as well as ET losses. Finally, $s_2(\theta_{sub}/n_2)[-]$ represents relative saturation of the second soil layer, which can be measured using the following equation [37]:

$$s_2(t_j) = s_{w2} + (s_2(t_{j-1}) - s_{w2})e^{-a(t_j - t_{j-1})} + (1 - s_{w2})bI(t_j)(t_j - t_{j-1})\ (7) \quad (7)$$

The SMAR parameters for different soil textures are shown in Table 2 [37,51]. In this part of the study, the daily RZSM (10–100 cm depth) was equivalent to the weighted average measured SM by measurement sensors at depths of 10, 40, and 100 cm at selected stations of the study area. SSM (0–10 cm depth) was also measured by the measurement sensor in the surface layer. The depth of surface layer in the SMAR model should not be less than 5 cm, otherwise the model might under-estimate the infiltration and face numerical problems [39]. While most satellite sensors provide information about soil water content no deeper than 0–5 cm of the top

soil, a number of studies demonstrated that satellite products can capture the SSM dynamics required for the SMAR model surface layer [29,39,44–46].

Table 2. the SMAR parameters for different soil texture [37,51].

Soil Type	N [-]	SW [-]	SC [-]
sand	0.44	0.06	0.14
loamy sand	0.44	0.11	0.24
sandy loam	0.45	0.19	0.42
silty loam	0.50	0.27	0.57
loam	0.46	0.25	0.50
sandy clay loam	0.40	0.34	0.62
silty clay loam	0.47	0.45	0.73
clay loam	0.46	0.40	0.67
sandy clay	0.43	0.51	0.75
clay	0.48	0.56	0.80

Three input sources were envisaged for the SMAR model (three schemes) in order to investigate the effect of spatial resolution of the results: (1) the SMAR model based on ground-based measured SSM, which estimates RZSM values at selected stations, (2) the SMAR model based on AMSR2 25 km SSM, and finally (3) the SMAR model based on downscaled 1 km SSM data using MODIS products.

2.1.3. Study Area

In this part of the study, the Rafsanjan Plain was taken as the area of study, situated in southeast Iran, Kerman Province (Figure 1), Iran's center of pistachio cultivation, comprising a total area of 5622 km^2. The study area is located between 55°1′ to 56°28′ longitude and 30°3′ to 31°11′ latitude, where the elevation ranges from 1296 to 2131 m above sea level (ASL). The average annual rainfall and average annual potential evapotranspiration (PET) here are below 100 mm and above 3000 mm, respectively. There is a thermic soil temperature regime and an aridic SM regime here.

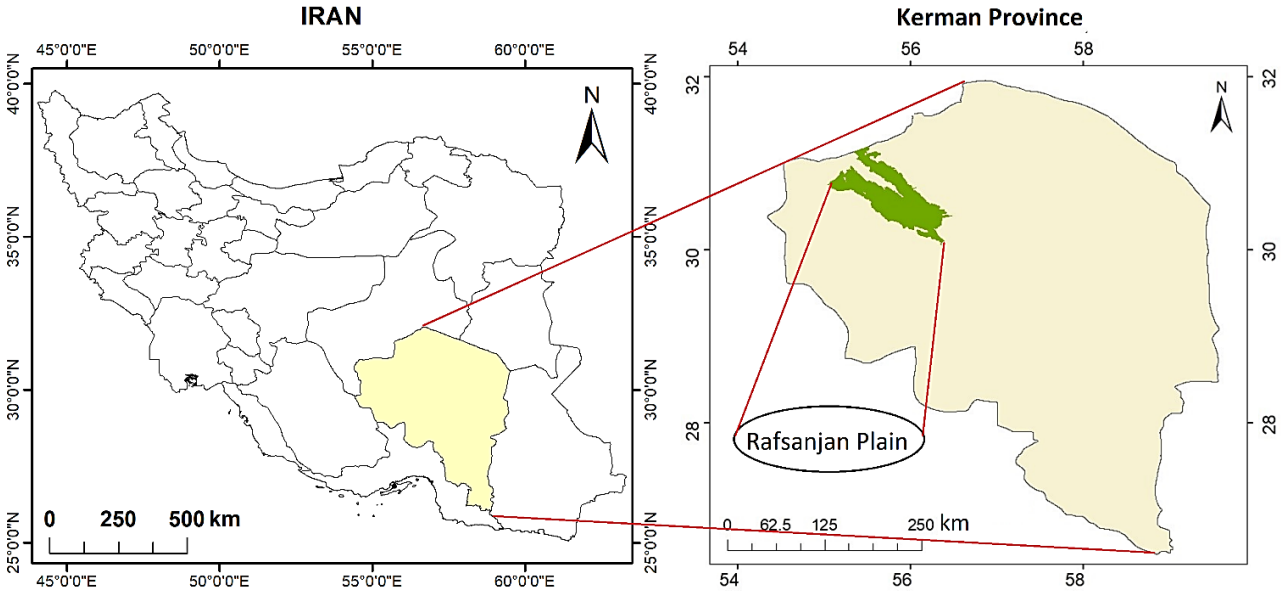

Figure 1. Geographical location of Rafsanjan Plain within Iran and Kerman Province.

2.1.4. Data

2.1.4.1. AMSR2 Satellite-Based SSM Data

The Global Change Observation Mission–Water 1 (GCOM-W1) satellite system was launched on 17 May 2012, to gather geophysical parameters, such as precipitation, sea surface temperature (SST), and SM, and witness variation in water circulation [40]. It carries the AMSR2 sensor aimed at retrieving earth-emitted radiometric waves and data utilized to estimate global-scale low-resolution SSM with a medial temporal resolution of a couple of days [40,41]. The land parameter retrieval model (LPRM) is extensively used to estimate SSM based on a radiative transfer forward (RTF) model responsible for the retrieval of vegetation optical depth (VOD) and SM. One can refer to the Japan aerospace exploration agency (JAXA) website (data downloadable in HDF5) or the NASA website (data downloadable in netCDF4), scenes (all measurements taken halfway between Earth's North and South Poles relative to observation point) or a global map (10 km and 25 km resolution), daily or monthly, to retrieve AMSR2 SSM products from Earth observation research center (EORC) for day/night readings.
This study retrieved and analyzed the data of daily global AMSR2 SSM estimates at 25 km spatial resolution from 19 July 2017 to 30 August 2018 for ascending (Asc.) overpasses. AMSR2 SSM data at 25 km spatial resolution were only available for Rafsanjan area by employing its geographic coordinates (https://hydro1.gesdisc.eosdis.nasa.gov/). (accessed on 18-Apr-2018). The complete ID of the product is: AMSR2/GCOM-W1 surface soil moisture (LPRM) L3 1 day 25 km × 25 km ascending V001 (LPRM_AMSR2_A_SOILM3) [42].

2.1.4.2. Ground-Based SM Data

To obtain ground-based measured SSM and RZSM data in the Rafsanjan Plain, REC-P55 SM sensors (presented by [43]) were installed in ten locations (Figure 2a) at three different depths of 10, 40, and 100 cm (Figure 2b). The daily soil temperature and moisture voltage were measured and recorded at 01:30pm (approximate ascending satellite overpass time) by a data logger. Sensors were pre-calibrated, and the moisture equations of each soil type were obtained for sensors by utilizing the weighing technique in the laboratory.
This study primarily analyzed SSM in each location during satellite crossing, followed by the analysis of soil profile moisture data. Two layers of surface and deep (root zone) soil with 10 and 90 cm depths were considered in the SMAR model, respectively (Figure 2c). RZSM (10–100 cm depth) was equivalent to the weighted average measured SM by measuring sensors at depths of 10, 40, and 100 cm at selected stations of the study area. SSM (0–10 cm depth) was also measured by the measurement sensor in the surface layer.

(**a**) (**b**) (**c**)

Figure 2. (**a**) Location of stations in Rafsanjan plain, (**b**) REC-P55 SM sensors manufactured by Ansari and Hassanpour [43] installed in study wells at three different depths of 10, 40, and 100 cm, and (**c**) two layers of surface and deep (root zone) soil considered in the SMAR model.

2.1.4.3. Remotely Sensed MODIS Parameters

The MODIS sensor was launched on board the Terra satellite in December 1999 and the Aqua satellite in May 2002, both belonging to NASA's international Earth Observing System (EOS), for data collection. They both revolve in a circular heliosynchronous orbit, enabling them to circle the earth every 99 min, i.e., 16 orbits each day, and gather information for the whole planet every one or two days. MODIS Albedo, LST, and NDVI products at a 1 km spatial resolution were retrieved in HDF4 format from EOS data and information system (EOSDIS) website (https://search.earthdata.nasa.gov/) (accessed on 13-Apr-2018) for the area of study. For this research, MODIS products, including MYD11A1 (Aqua Satellite), were used to estimate 1 km resolution LST (Figure 3a), and 16-day dataset MOD13A2 (Terra Satellite) and MYD13A2 (Aqua Satellite) were used to create 8-day NDVI layers (Figure 3b). Surface albedo(α) was also estimated from a combination of bands 1 to 7 of the MODIS product (MOD09A1) (Figure 3c).

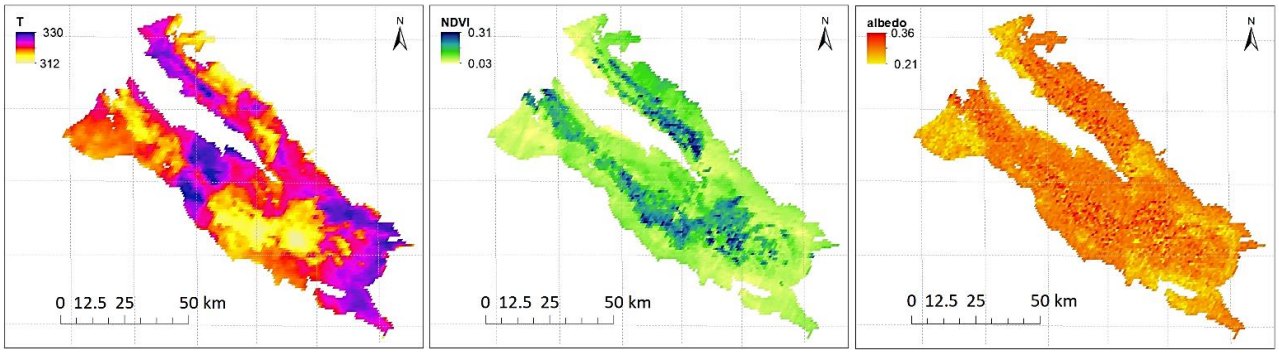

(**a**) (**b**) (**c**)

Figure 3. MODIS (**a**) land surface temperature, (**b**) NDVI, and (**c**) Albedo products of Rafsanjan Plain for random days during the study period.

2.1.5. Results

2.1.5.1. AMSR2 Downscaling Using MODIS Albedo, LST and NDVI

The AMSR2 SSM product at a 25 km spatial resolution was downscaled to 1 km spatial resolution using a simple linear equation containing MODIS Albedo, LST, and NDVI products (Figure 4). The following equation shows how AMSR2 data are downscaled:

$$\theta_s = 0.893 - 0.931\ A - 0.256\ V - 0.0025\ T + 0.0027\ TV - 0.00226\ TA - 2.133\ VA \quad (8)$$

In the above equation, θs represents downscaled SSM. A, T, and V represent albedo, LST, and NDVI, respectively. The remainder is A-T-V interactions (i.e., TA, VA, and VT). The regression model was obtained with $R^2 = 0.61$ and the acceptable *p*-value (<0.05) and F-statistic test ($=4.3 \times 10^{-248}$). Table 3 shows that *p*-values are below the significance level of 5%, meaning that the null hypothesis for each coefficient is rejected and all components are significant in the linear equation. The results indicated that the downscaling model offered an excellent fit with the AMSR2 estimates.

Table 3. Results of linear regression modeling.

Coefficient	Value	Squared Error	T-Statistic	P(%)
a_{000}	0.892618	0.0041	49.12	0.0015
a_{100}	−0.93067	2.45×10^{-5}	2.98	0.1431
a_{010}	−0.00246	1.62×10^{-5}	1.97	0.1275
a_{001}	0.255988	5.31×10^{-7}	−1.66	0.1112
a_{110}	0.002259	1.02×10^{-7}	−3.24	0.1255
a_{101}	−2.13287	1.78×10^{-9}	−0.12	0.2928
a_{011}	0.0027	2.12×10^{-9}	0.11	0.1159

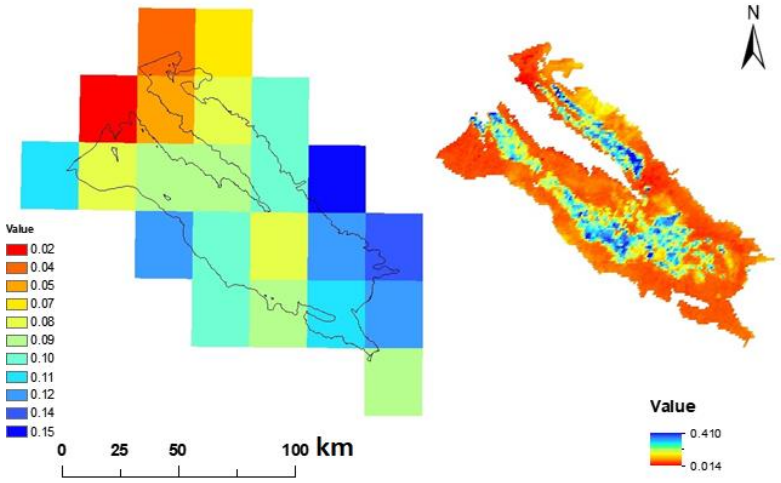

(**a**)

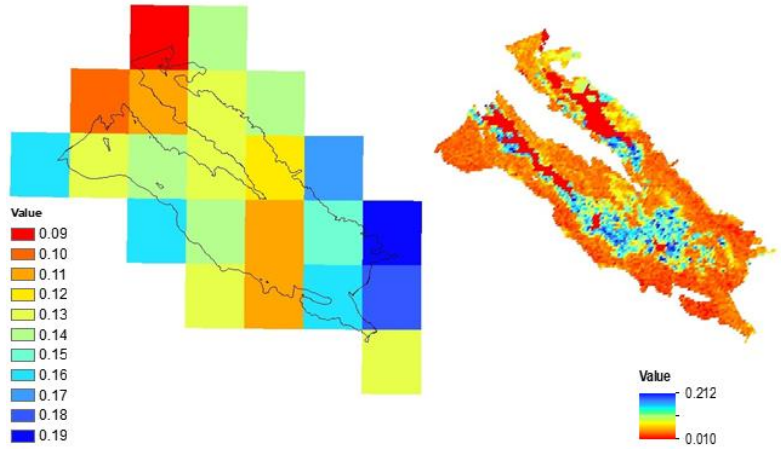

(**b**)

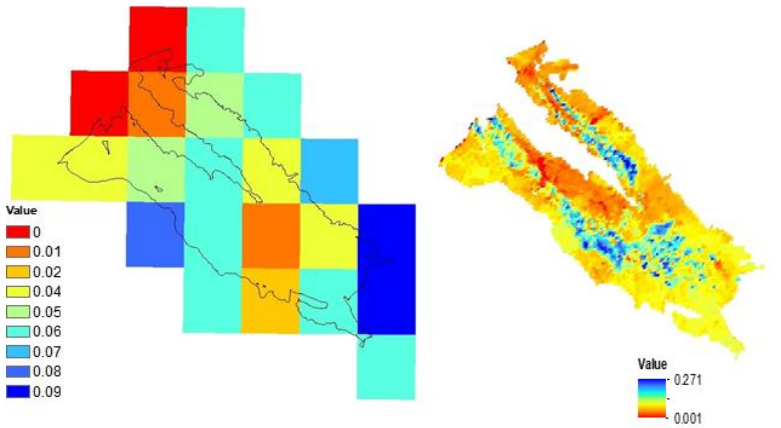

(**c**)

Figure 4. The conventional AMSRE (Left) and downscaled AMSRE (Right) SSM maps of the Rafsanjan plain on (**a**) 19-09-2017, (**b**) 01-01-2018, (**c**) 08-07-2018, and (**d**) 8/29/2018.

The AMSR2 25 km SSM and downscaled SSM values were examined by calculating MAE, RMSE, and R for every station. According to Table 4, comparing AMSR2 25 km SSM and measured values in every station revealed that the results obtained were not satisfactory for most of the stations. The highest MAE and RMSE values were obtained at Station 2. The R-value was also estimated as low at Stations 1, 2, 3, 6, and 7, which could be affected by the distance from the station to the centroid (distance) at each AMSR2 25 km/pixel, such that R values were found to be acceptable at Stations 4, 5, and 10.

Table 4. Basic statistics for each station for the comparison between the AMSR2 25 km SSM and downscaled SSM with ground-based SSM.

		AMSR2 25 km SSM			Downscaled AMSR2 1 km SSM		
Station	**Distance (km)**	**MAE (m^3/m^3)**	**RMSE (m^3/m^3)**	**R (-)**	**MAE (m^3/m^3)**	**RMSE (m^3/m^3)**	**R (-)**
1	5.84	0.028	0.030	0.473	0.012	0.015	0.742
2	8.46	0.092	0.094	0.400	0.047	0.047	0.876
3	9.73	0.043	0.044	0.350	0.011	0.013	0.715
4	2.10	0.029	0.030	0.783	0.013	0.017	0.707
5	1.97	0.027	0.029	0.707	0.025	0.029	0.782
6	2.58	0.037	0.040	0.491	0.028	0.031	0.538
7	14.27	0.050	0.051	0.232	0.026	0.032	0.793
8	2.35	0.035	0.035	0.603	0.009	0.009	0.735
9	3.46	0.004	0.004	0.666	0.002	0.004	0.802
10	1.06	0.042	0.043	0.700	0.003	0.003	0.705
Average	5.18	0.039	0.040	0.540	0.018	0.020	0.739

Other factors such as changes in vegetation density, land cover, land use, etc., at AMSR2 25 km pixel could also affect the results of MAE, RMSE, and R. Evaluating the land cover map of the study area (Figure 5a) showed that vegetation was uniform at 25 km pixels containing Stations 4, 5, 8, 9, and 10 (dominant vegetation at 25 km × 25 km pixels containing Stations 4, 5, and 10 includes irrigated agriculture and pistachio orchards, and at pixels containing Stations 8 and 9, it includes rangeland). These stations were located at places similar to the dominant vegetation cover (VC) in the pixel in terms of vegetation, influencing the superiority of results obtained from there. However, VC at Station 2 was different from the dominant vegetation of the area located in the pixel (dominant cropping pattern in this pixel included low-density rangelands and non-vegetated lands). This led to increased MAE and RMSE values and decreased R-value, save for the distance. Thus, it can be stated that the AMSR2 25 km SSM values exhibit a large-area spatial mean (25 km). Assigning the data to all points in there was ineffective, despite being successful in some stations. Hence, the area must be reduced using downscaling methods.

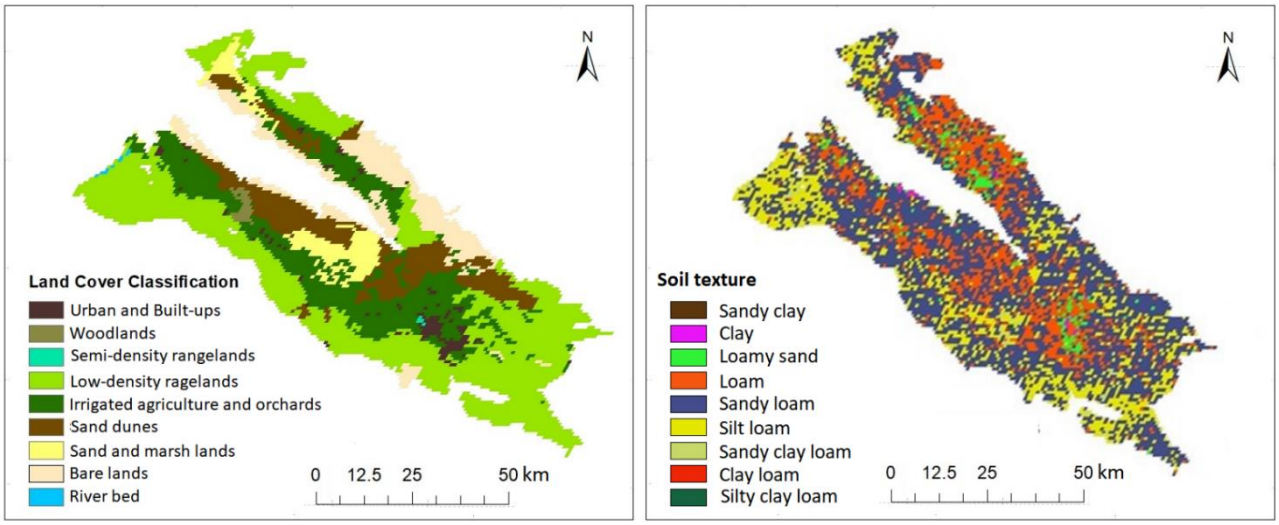

(**a**) (**b**)

Figure 5. (**a**) Landuse/landcover map, and (**b**) soil texture map of the Rafsanjan Plain.

According to Table 4, comparing downscaled SSM results with the measured values at each station indicated a decreased error rate, increased correlation coefficient, and improved SSM results for the stations far from the midpoint of the pixel (Figure 2a), all mediated by the downscaling technique used. Consequently, at Stations 1, 2, 3, and 7, error values decreased, and correlation coefficients increased. Therefore, the downscaling method that uses MODIS parameters was arguably more correlated with measured SSM data. The time series of Measured, ordinary AMSR2, and downscaled ASMR2 SSM data at 10 study station has been depicted in Figure 6 as well. The increase in the consistency and accuracy of the downscaled AMSR2 data with respect to the measured SSM data in almost all stations is visible in Figure 6.

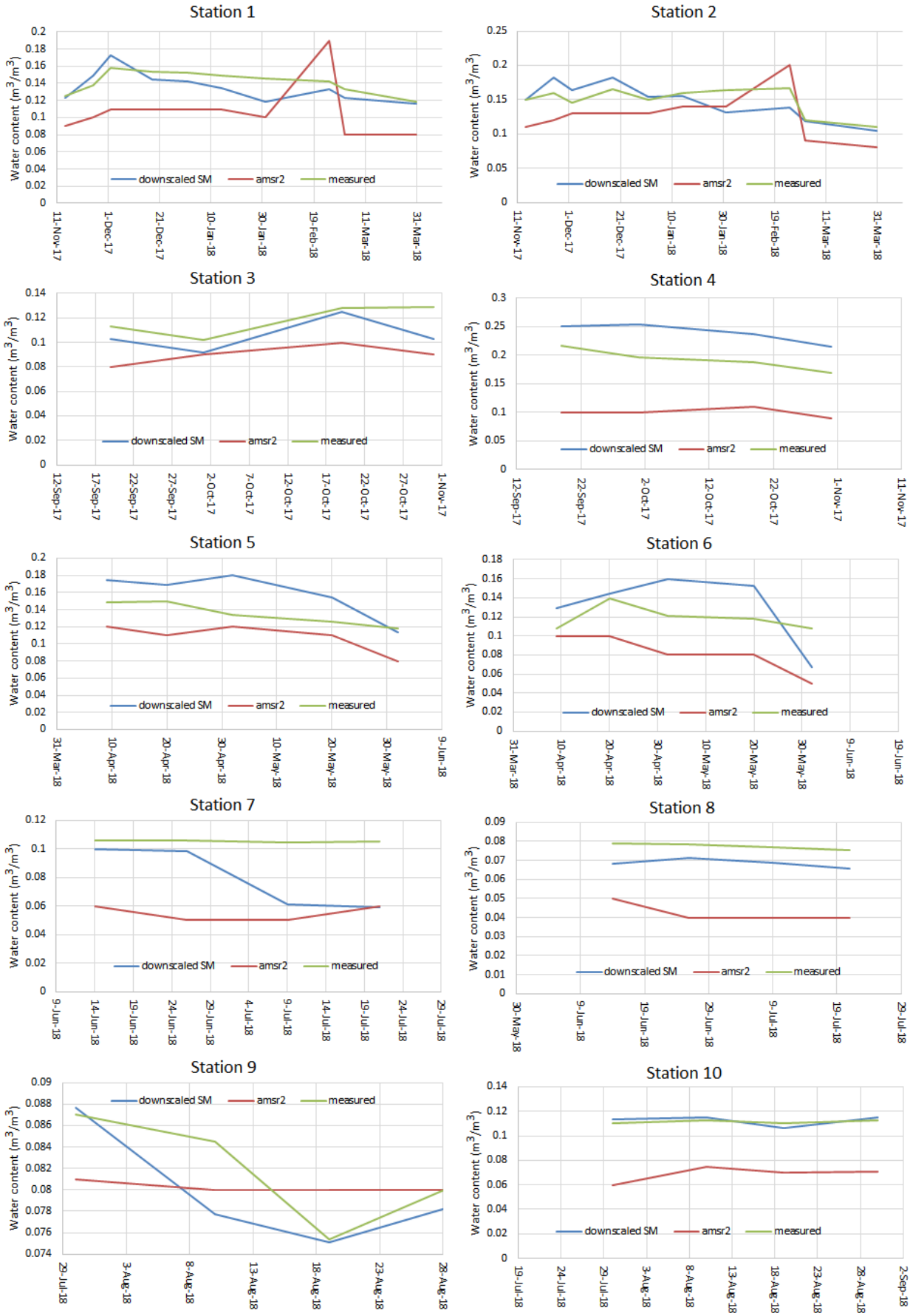

Figure 6. time series of Measured, ordinary AMSR2, and downscaled ASMR2 SSM data at ten study stations. Stations 1-10 correspond to the numbered red dots in figure 1a

2.1.5.2. RZSM Estimation Based on the SMAR Model

Three of the four SMAR parameters (i.e., n, s_w, and s_c) were determined based on soil texture map of the study area (Figure 5b), according to Table 2. Considering the SM loss coefficient justifying percolation and ET losses (V_2) in the SMAR model, the V_2 value was obtained 5.8 mm/day regarding optimization based on regional conditions using the genetic algorithm (GA) in MATLAB programing environment, with RMSE function between simulated RZSM and observational values.

Figure 7 illustrates the results of statistical analyses for the comparison results of SMAR-estimated RZSM using three schemes at ten stations. Notably, the SMAR model based on downscaled SSM has estimated RZSM with relatively high precision in most stations. The MAE and RMSE values at Station 2 were found to be higher than other stations, which could be attributed to high error values of the SSM downscaling model of this station as compared to other stations. It can, therefore, be said that in every station where the downscaling model estimates SSM at a low error rate, the SMAR model could also estimate RZSM more accurately.

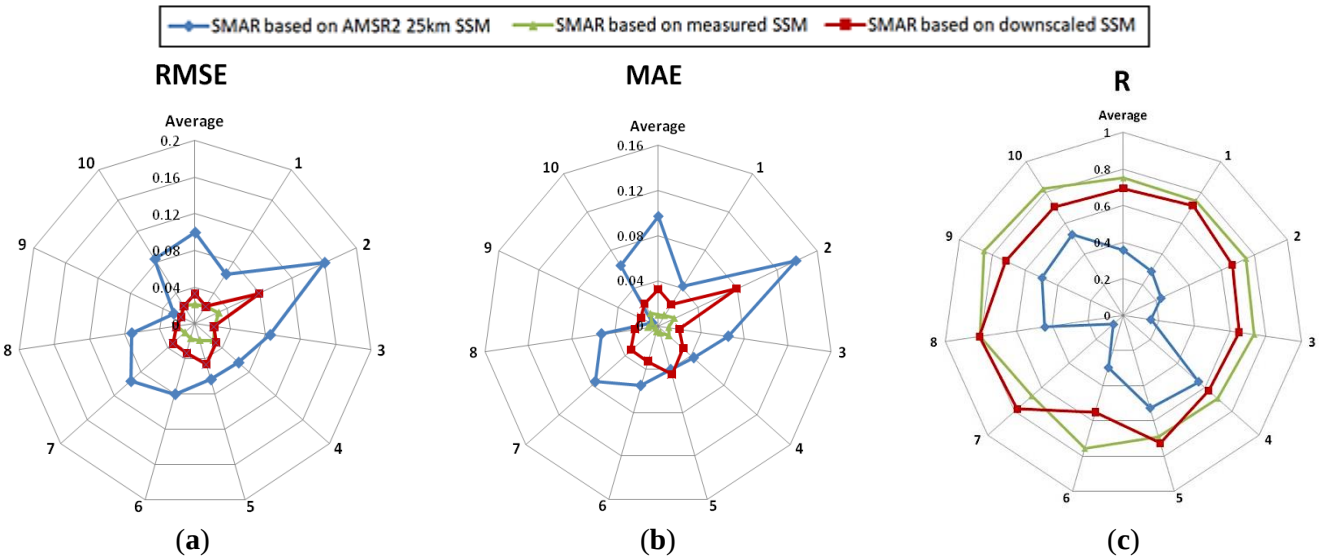

Figure 7. Basic statistics for the comparison results of SMAR-estimated RZSM using Schemes 1, 2, and 3 at ten stations.

The results indicated an increased accuracy of the model in estimating RZSM using the downscaled SSM data obtained from the method proposed in this part of the study. In this method, mean R, RMSE, MAE values between all the stations were obtained equal to 0.71, 0.032, 0.032, respectively. Since SSM is considered as the most critical parameter of the SMAR model provided that it could be estimated with high accuracy, it will affect the more accurate estimation of RZSM by the SMAR model, verified by the results obtained. The downscaled SSM-based SMAR model can be utilized to develop a system for receiving downscaled SSM values to create RZSM maps. Hence, the AMSR2-downscaled SSM model was used in the SMAR model based on MODIS parameters, and the RZSM values were obtained at 1 km pixels for different days. Figure 8 depicts the downscaled RZSM sample (θ_{sub}) based on the SMAR model in the Rafsanjan Plain for 29 August 2018.

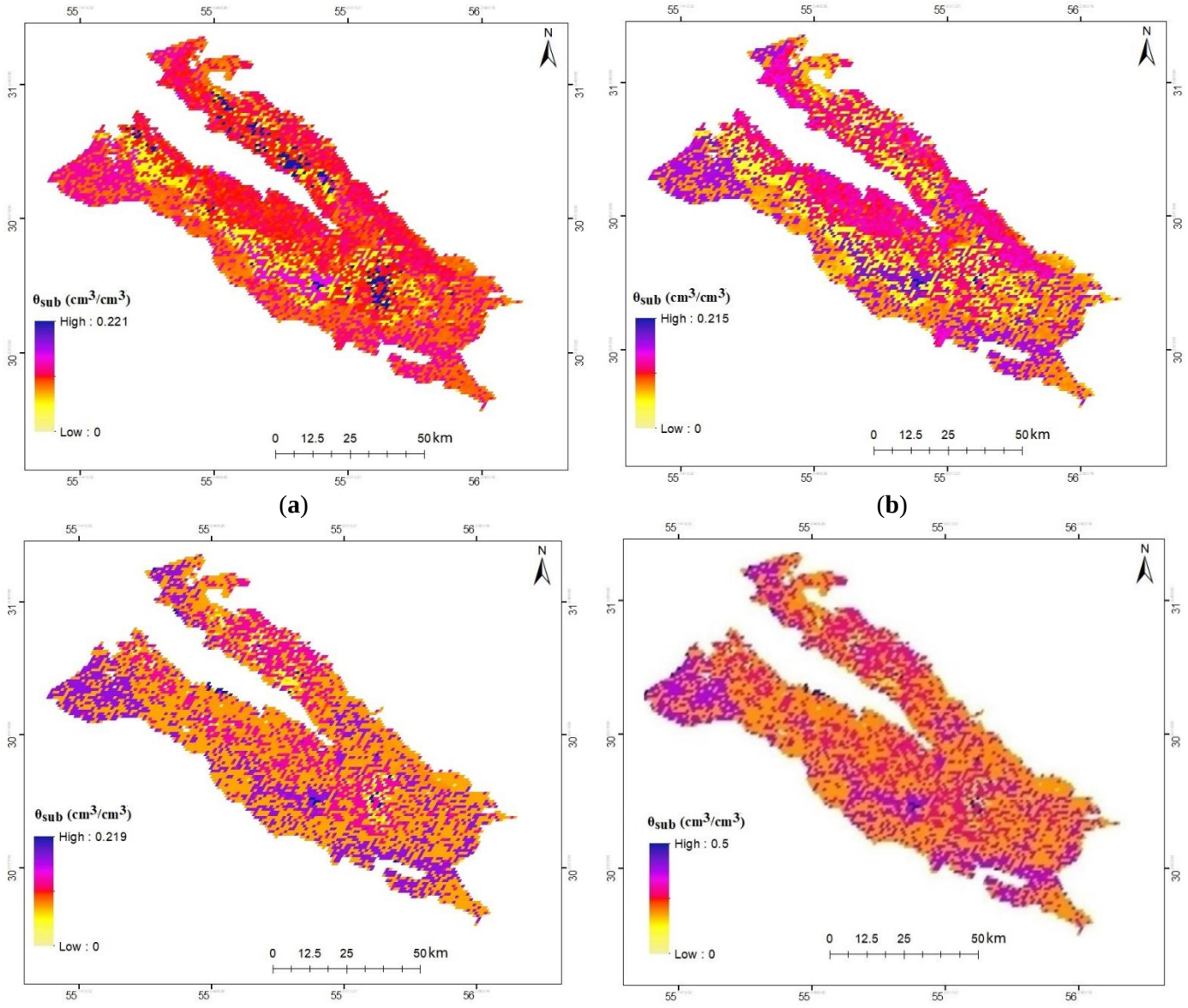

Figure 8. The downscaled RZSM (θ_{sub}) values in Rafsanjan plain on (**a**) 9/19/2017, (**b**) 10/1/2017, (**c**) 5/31/2018, and (**d**) 8/29/2018.

2.1.6. Discussion

This study developed an RZSM estimation model, i.e., SMAR, at 1 km × 1 km pixels in the Rafsanjan Plain. Initially, the AMSR2 25 km SSM was compared with the ground-based SSM values in the Rafsanjan Plain. The overall validation results suggested a low correlation in most stations. In addition to the distance of the station from the midpoint of 25 km pixel, other factors such as changes in vegetation compaction, land-use, topography, rainfall, and soil properties of the study area could affect the correlation between large-scale data and measured field data. It is necessary to collect more SSM data from 25 km pixels to have stronger validation. The coarse-resolution satellite-based SSM data necessitates the downscaling of SSM data for many hydrological and agricultural plans in the study area, contributing to a precise RZSM estimation by the SMAR model on a finer scale.

Since fine-resolution MODIS data are available globally and daily, this part of the study considered the downscaled AMSR2 SSM based on MODIS parameters. The results demonstrated a good consistency between the downscaling method that exploits these parameters and the measured data—which were consistent with those of the previous studies [20,52]—leading to reduced error rates and increased correlation coefficients at measurement stations. The downscaled SSM was estimated using a linear equation, which correlated MODIS Albedo, LST, and NDVI. After the downscaling, at Stations 1, 2, 3, and 7, the correlation coefficients increased

from 0.473, 0.400, 0.350, and 0.232 to 0.742, 0.876, 0.715, and 0.793, respectively, and the values of MAE and RMSE in the root zone decreased, indicating improved results by using the above-mentioned downscaling technique.

To obtain RZSM at 1 km pixel in the Rafsanjan Plain, the downscaled SSM model was used based on MODIS parameters in the SMAR model. RZSM obtained from the SMAR model based on downscaled SSM was compared with measurement RZSM data. The results indicated that the model could initially manage to estimate RZSM values from SSM variations, and then increase the accuracy of the model to estimate RZSM using the downscaled data obtained from the proposed method in this part of the study. Mean R, RMSE, MAE values were obtained for all the stations equal to 0.71, 0.032, 0.032, respectively. As the most crucial parameter of the SMAR model, the accurate estimation of SSM will affect the more accurate estimation of RZSM by this model [39].

2.1.7. Conclusions

It is essential to estimate RZSM for different biogeochemical, ecological, and hydrometeorological applications and modeling. This study developed the SMAR model for estimating RZSM at 1 km pixels of the Rafsanjan Plain and subsequently, evaluated its variations. Spatiotemporal continuity of estimated RZSM by this model is one of the advantages of this method. SSM is the most important input parameter in the SMAR model, which will lead to a more accurate estimation of RZSM if precisely determined. Methods based on microwave remote sensing are suitable for retrieving SSM.

It is suggested to estimate other effective parameters of the model, e.g., soil moisture loss coefficient and soil texture parameters, more accurately for each pixel in the Rafsanjan Plain, optimize them with measured data, and use them in the SMAR model. It was generally concluded that the SMAR model, in which SSM was downscaled based on MODIS parameters, could accurately estimate and demonstrate the variations of the RZSM of the Rafsanjan Plain.

It is also suggested to consider other affecting variables, including rainfall that improves downscaled SSM products. Consider the effect of other VIs, including soil-adjusted vegetation index (SAVI) or simple ratio vegetation index (SRVI) on improved quality of downscaled products, and utilize the best of these indices. Optimization of downscaling approaches using sensitivity analysis (SA) by a network of sensors within the coverage area of a single AMSR2 pixel is suggested to validate the AMSR2 products and downscaled SSM values in the future studies.

2.1.8. References

1. Hanson, J.D.; Rojas, K.; Shaffer, M.J. Calibrating the root zone water quality model. *Agron. J.* **1999**, *91*, 171–177.
2. Li, Z.-L.; Leng, P.; Zhou, C.-H.; Chen, K.-S.; Zhou, F.-C.; Shang, G.-F. Soil moisture retrieval from remote sensing measurements: Current knowledge and directions for the future. *Earth Sci. Rev.* **2021**, 218, 103673.
3. Das, N.N.; Mohanty, B.P. Root zone soil moisture assessment using remote sensing and vadose zone modeling. *Vadose Zone J.* **2006**, *5*, 296–307.
4. Georgakakos, K.P. *Soil Moisture Theories and Observations-Preface*; Elsevier Science Bv: Amsterdam, The Netherlands, 1996.
5. Nuñez-Olivieri, J.; Muñoz-Barreto, J.; Tirado-Corbalá, R.; Lakhankar, T.; Fisher, A. Comparison and downscale of AMSR2 soil moisture products with in situ measurements from the SCAN–NRCS network over Puerto Rico. *Hydrology* **2017**, *4*, 46.
6. Crow, W.T.; Berg, A.A.; Cosh, M.H.; Loew, A.; Mohanty, B.P.; Panciera, R.; de Rosnay, P.; Ryu, D.; Walker, J.P. Upscaling sparse ground-based soil moisture observations for the validation of coarse-resolution satellite soil moisture products. *Rev. Geophys.* **2012**, *50, 1-20.*
7. Njoku, E.G.; Jackson, T.J.; Lakshmi, V.; Chan, T.K.; Nghiem, S.V. Soil moisture retrieval from AMSR-E. *IEEE Trans. Geosci. Remote Sens.* **2003**, *41*, 215–229.
8. Zreda, M.; Shuttleworth, W.; Zeng, X.; Zweck, C.; Desilets, D.; Franz, T.; Rosolem, R. COSMOS: The cosmic-ray soil moisture observing system. *Hydrol. Earth Syst. Sci.* **2012**, *16*, 4079–4099.
9. Montzka, C.; Bogena, H.R.; Zreda, M.; Monerris, A.; Morrison, R.; Muddu, S.; Vereecken, H. Validation of spaceborne and modelled surface soil moisture products with cosmic-ray neutron probes. *Remote Sens.* **2017**, *9*, 103.
10. Das, N.N.; Entekhabi, D.; Dunbar, R.S.; Chaubell, M.J.; Colliander, A.; Yueh, S.; Jagdhuber, T.; Chen, F.; Crow, W.; O'Neill, P.E. The SMAP and Copernicus Sentinel 1A/B microwave active-passive high resolution surface soil moisture product. *Remote Sens. Environ.* **2019**, *233*, 111380.

11. Cho, E.; Su, C.-H.; Ryu, D.; Kim, H.; Choi, M. Does AMSR2 produce better soil moisture retrievals than AMSR-E over Australia? *Remote Sens. Environ.* **2017**, *188*, 95–105.
12. Gruhier, C.; Rosnay, P.d.; Hasenauer, S.; Holmes, T.; Jeu, R.d.; Kerr, Y.; Mougin, E.; Njoku, E.; Timouk, F.; Wagner, W. Soil moisture active and passive microwave products: Intercomparison and evaluation over a Sahelian site. *Hydrol. Earth Syst. Sci.* **2010**, *14*, 141–156.
13. Su, C.-H.; Zhang, J.; Gruber, A.; Parinussa, R.; Ryu, D.; Crow, W.T.; Wagner, W. Error decomposition of nine passive and active microwave satellite soil moisture data sets over Australia. *Remote Sens. Environ.* **2016**, *182*, 128–140.
14. Malbéteau, Y.; Merlin, O.; Gascoin, S.; Gastellu, J.P.; Mattar, C.; Olivera-Guerra, L.; Khabba, S.; Jarlan, L. Normalizing land surface temperature data for elevation and illumination effects in mountainous areas: A case study using ASTER data over a steep-sided valley in Morocco. *Remote Sens. Environ.* **2017**, *189*, 25–39.
15. Wang, Y.; Leng, P.; Ma, J.; Peng, J. A Method for Downscaling Satellite Soil Moisture Based on Land Surface Temperature and Net Surface Shortwave Radiation. *Ieee Geosci. Remote Sens. Lett.* **2021**.
16. Jackson, T.J.; Cosh, M.H.; Bindlish, R.; Starks, P.J.; Bosch, D.D.; Seyfried, M.; Goodrich, D.C.; Moran, M.S.; Du, J. Validation of advanced microwave scanning radiometer soil moisture products. *IEEE Trans. Geosci. Remote Sens.* **2010**, *48*, 4256–4272.
17. Yan, H.; DeChant, C.M.; Moradkhani, H. Improving soil moisture profile prediction with the particle filter-Markov chain Monte Carlo method. *IEEE Trans. Geosci. Remote Sens.* **2015**, *53*, 6134–6147.
18. Liu, P.-W.; Bindlish, R.; Fang, B.; Lakshmi, V.; O'Neill, P.E.; Yang, Z.; Cosh, M.H.; Bongiovanni, T.; Bosch, D.D.; Collins, C.H. Assessing Disaggregated SMAP Soil Moisture Products in the United States. *IEEE J. Sel. Top. Appl. Earth Obs. Remote Sens.* **2021**, *14*, 2577–2592.
19. Chauhan, N.; Miller, S.; Ardanuy, P. Spaceborne soil moisture estimation at high resolution: A microwave-optical/IR synergistic approach. *Int. J. Remote Sens.* **2003**, *24*, 4599–4622.
20. Choi, M.; Hur, Y. A microwave-optical/infrared disaggregation for improving spatial representation of soil moisture using AMSR-E and MODIS products. *Remote Sens. Environ.* **2012**, *124*, 259–269.
21. Piles, M.; Sánchez, N.; Vall-llossera, M.; Camps, A.; Martínez-Fernández, J.; Martínez, J.; González-Gambau, V. A downscaling approach for SMOS land observations: Evaluation of high-resolution soil moisture maps over the Iberian Peninsula. *IEEE J. Sel. Top. Appl. Earth Obs. Remote Sens.* **2014**, *7*, 3845–3857.
22. Sánchez-Ruiz, S.; Piles, M.; Sánchez, N.; Martínez-Fernández, J.; Vall-llossera, M.; Camps, A. Combining SMOS with visible and near/shortwave/thermal infrared satellite data for high resolution soil moisture estimates. *J. Hydrol.* **2014**, *516*, 273–283.
23. Zhao, W.; Li, A. A downscaling method for improving the spatial resolution of AMSR-E derived soil moisture product based on MSG-SEVIRI data. *Remote Sens.* **2013**, *5*, 6790–6811.
24. Piles, M.; Sánchez, N. Spatial downscaling of passive microwave data with visible-to-infrared information for high-resolution soil moisture mapping. In *Satellite Soil Moisture Retrieval*; Elsevier: 2016; pp. 109–132.
25. Gao, H.; Wood, E.F.; Jackson, T.; Drusch, M.; Bindlish, R. Using TRMM/TMI to retrieve surface soil moisture over the southern United States from 1998 to 2002. *J. Hydrometeorol.* **2006**, *7*, 23–38.
26. Escorihuela, M.-J.; Chanzy, A.; Wigneron, J.-P.; Kerr, Y. Effective soil moisture sampling depth of L-band radiometry: A case study. *Remote Sens. Environ.* **2010**, *114*, 995–1001.
27. Mahmood, R.; Hubbard, K.G. Relationship between soil moisture of near surface and multiple depths of the root zone under heterogeneous land uses and varying hydroclimatic conditions. *Hydrol. Process. Int. J.* **2007**, *21*, 3449–3462.
28. Mahmood, R.; Littell, A.; Hubbard, K.G.; You, J. Observed data-based assessment of relationships among soil moisture at various depths, precipitation, and temperature. *Appl. Geogr.* **2012**, *34*, 255–264.
29. Baldwin, D.; Manfreda, S.; Keller, K.; Smithwick, E. Predicting root zone soil moisture with soil properties and satellite near-surface moisture data across the conterminous United States. *J. Hydrol.* **2017**, *546*, 393–404.
30. Ragab, R. Towards a continuous operational system to estimate the root-zone soil moisture from intermittent remotely sensed surface moisture. *J. Hydrol.* **1995**, *173*, 1–25.
31. Puma, M.J.; Celia, M.A.; Rodriguez-Iturbe, I.; Guswa, A.J. Functional relationship to describe temporal statistics of soil moisture averaged over different depths. *Adv. Water Resour.* **2005**, *28*, 553–566.
32. Manfreda, S.; McCabe, M.F.; Fiorentino, M.; Rodríguez-Iturbe, I.; Wood, E.F. Scaling characteristics of spatial patterns of soil moisture from distributed modelling. *Adv. Water Resour.* **2007**, *30*, 2145–2150.
33. Sabater, J.M.; Jarlan, L.; Calvet, J.-C.; Bouyssel, F.; De Rosnay, P. From near-surface to root-zone soil moisture using different assimilation techniques. *J. Hydrometeorol.* **2007**, *8*, 194–206.
34. Wagner, W.; Lemoine, G.; Rott, H. A method for estimating soil moisture from ERS scatterometer and soil data. *Remote Sens. Environ.* **1999**, *70*, 191–207.
35. Laio, F.; Porporato, A.; Fernandez-Illescas, C.; Rodriguez-Iturbe, I. Plants in water-controlled ecosystems: Active role in hydrologic processes and response to water stress: IV. Discussion of real cases. *Adv. Water Resour.* **2001**, *24*, 745–762.
36. Manfreda, S.; Fiorentino, M. A stochastic approach for the description of the water balance dynamics in a river basin. *Hydrol. Earth Syst. Sci.* **2008**, *12*, 1189–1200.
37. Manfreda, S.; Brocca, L.; Moramarco, T.; Melone, F.; Sheffield, J. A physically based approach for the estimation of root-zone soil moisture from surface measurements. *Hydrol. Earth Syst. Sci.* **2014**, *18*, 1199–1212.

38. Jackson, T.J.; Schmugge, T.J. Passive microwave remote sensing system for soil moisture: Some supporting research. *Ieee Trans. Geosci. Remote Sens.* **1989**, *27*, 225–235.
39. Faridani, F.; Farid, A.; Ansari, H.; Manfreda, S. Estimation of the root-zone soil moisture using passive microwave remote sensing and SMAR Model. *J. Irrig. Drain. Eng.* **2017**, *143*, 04016070.
40. Kawaguchi, M.; Yoshida, T. Regular Observation by Global Change Observation Mission 1st-Water GCOM-W1 (Shizuku). *Nec Tech. J* **2013**, *8*, 32–35.
41. Hihara, T.; Kubota, M.; Okuro, A. Evaluation of sea surface temperature and wind speed observed by GCOM-W1/AMSR2 using in situ data and global products. *Remote Sens. Environ.* **2015**, *164*, 170–178.
42. Owe, M.; de Jeu, R.; Holmes, T. Multisensor historical climatology of satellite-derived global land surface moisture. *J. Geophys. Res. Earth Surf.* **2008**, *113*, *F01002*, *1-17*.
43. Ansari, H.; Hassanpour, M. Design and construction of REC-P55 for reading of soil moisture, temperature and salinity. *Iran. J. Irrig. Drain.* **2015**, *9*, 32–43.
44. Peng, J.; Loew, A.; Merlin, O.; Verhoest, N.E. A review of spatial downscaling of satellite remotely sensed soil moisture. *Rev. Geophys.* **2017**, *55*, 341–366.
45. Busch, F.A.; Niemann, J.D.; Coleman, M. Evaluation of an empirical orthogonal function–based method to downscale soil moisture patterns based on topographical attributes. *Hydrol. Process.* **2012**, *26*, 2696–2709.
46. Coleman, M.L.; Niemann, J.D. Controls on topographic dependence and temporal instability in catchment-scale soil moisture patterns. *Water Resour. Res.* **2013**, *49*, 1625–1642.
47. Ray, R.L.; Jacobs, J.M.; Cosh, M.H. Landslide susceptibility mapping using downscaled AMSR-E soil moisture: A case study from Cleveland Corral, California, US. *Remote Sens. Environ.* **2010**, *114*, 2624–2636.
48. Gheybi, F.; Paridad, P.; Faridani, F.; Farid, A.; Pizarro, A.; Fiorentino, M.; Manfreda, S. Soil Moisture Monitoring in Iran by Implementing Satellite Data into the Root-Zone SMAR Model. *Hydrology* **2019**, *6*, 44.
49. Baldwin, D.; Manfreda, S.; Lin, H.; Smithwick, E.A. Estimating root zone soil moisture across the Eastern United States with passive microwave satellite data and a simple hydrologic model. *Remote Sens.* **2019**, *11*, 2013.
50. Zhuang, R.; Zeng, Y.; Manfreda, S.; Su, Z. Quantifying long-term land surface and root zone soil moisture over Tibetan Plateau. *Remote Sens.* **2020**, *12*, 509.
51. Laio, F. A vertically extended stochastic model of soil moisture in the root zone. *Water Resour. Res.* **2006**, *42, W02406*, *1-10*.
52. Piles, M.; Camps, A.; Vall-Llossera, M.; Corbella, I.; Panciera, R.; Rudiger, C.; Kerr, Y.H.; Walker, J. Downscaling SMOS-derived soil moisture using MODIS visible/infrared data. *IEEE Trans. Geosci. Remote Sens.* **2011**, *49*, 3156–3166.

Part 2. Estimating soil water balance components from surface soil moisture measurements using a physically-based approach

2.2.1. Introduction

The quantification of hydrological components in the soil is crucial for different applications of water resources management such as irrigation, drinking water and industry [1]. The hydrological variability is predicted to increase with the climate change, making predictions for recharge and groundwater storage even more important to implement and to maintain sustainable water use [2]. Groundwater is usually the only source of water in arid and semiarid regions due to low amount of precipitation, and lack of surface water resources. The water balance estimation is one of the most sensitive steps in groundwater management which have a critical component in the commonly known "recharge rate estimation" [3,4].

Most of the soil-water processes in agricultural fields occur while the soil is in unsaturated condition [5]. The unsaturated soil is well-known as a complicated porous media due to its temporally and spatially variable parameters. Consequently, the unsaturated water flow in such condition is hard to measure or simulate, especially when hysteresis (i.e. the dependence of soil water retention curve on whether soil is wetting or draining) and root water uptake are taken into account [5,6]. Recently, the unsaturated flow modeling has become one of the most active topics of research in hydrology and soil physics [7,8].

Many models of varying degree of complexity and dimensionality have been developed during the past several decades to quantify the basic physical and chemical processes affecting water flow and pollutant transport in the unsaturated zone [9,10]. These models are now being used increasingly for a wide range of applications in research and management of natural subsurface systems. Modeling approaches range from relatively simple analytical and semi-analytical models (e.g. SWI [11], SMAR [12]) to more complex numerical codes (e.g. HYDRUS [7], MODFLOW-SURFACT [13], STOMP [14], SWAP [15], and TOUGH2 [16]) that permit consideration of a large number of simultaneous nonlinear processes.

The description of an analytical relationship between the soil moisture at the surface and in the lower soil layers has been emphasized as a significant challenge [17-21]. The Soil Moisture Analytical Relationship (SMAR) was derived from a simplified soil water balance equation for arid and semi-arid environments that provides a relationship between root-zone and surface soil moisture. Applications of the SMAR model in estimating root-zone soil moisture (RZSM) from a time series of in-situ and remotely sensed surface soil moisture (SSM), at both local and regional scales, proved the performance in providing a good description of RZSM (e.g., [12,22-26]). The advantage of the SMAR model is that there are clear physical interpretations for the SMAR parameters which can be directly determined knowing soil texture and climate of the target location. In the original model proposed by [12], the water loss function was assumed to be a linear function of current soil moisture content and maximum water loss in the soil which is in a way the sum of maximum evapotranspiration and deep percolation. [24] presented the Modified SMAR model (MSMAR) using a soil water loss function that could account for the non-linearity of the water loss process and estimate daily ET and DP separately.

Among variety of proposed methodologies [27-29], numerical simulation of transient water flow in saturated-unsaturated porous media using HYDRUS software has been widely used in many different branches such as drip and pitcher irrigation modeling [30-32], root zone and deep vadose zone modeling [33,34], groundwater modeling [2,35], and hydrology [36,37].

The objective of this paper is to introduce a physically based model that estimates Soil Moisture, Evapotranspiration and Deep Percolation using information about surface soil moisture and soil texture only. HYDRUS-1D as a well-known numerical method will be used to compare the performance of two different approaches (i.e. analytical and numerical) in modeling soil hydrological processes using field measurements in a sprinkler irrigated farm Northwest Iran. It is expected that the proposed methodology would provide the

possibility of estimating hydrological components in the large scales using also satellite surface soil moisture data which is available on the daily basis for the whole world.

2.2.2. Methodology

2.2.2.1. HYDRUS-1D Numerical Model

HYDRUS-1D [10] is a physically-based model to solve and couple governing equations of water flow, solute and heat transport along with root water and nutrient uptake. Water flow in a variably-saturated soil in HYDRUS-1D is described by the mixed-form of a Richards' equation [40].

$$\frac{\partial \theta}{\partial t} = \frac{\partial}{\partial z}\left[K(\psi)\frac{\partial \psi}{\partial z} + K(\psi)\right] - RWU \tag{1}$$

where, θ is volumetric water content [L^3L^{-3}], ψ is soil water pressure head [L], K is saturated/unsaturated hydraulic conductivity [LT^{-1}], t is time [T], z is vertical space coordinate [L], and RWU is root water uptake [$L^3L^{-3}T^{-1}$]. Thanks to the constitutive relations of soil water retention curve $\theta(\psi)$ and saturated/unsaturated hydraulic conductivity, HYDRUS-1D employs a so-called Modified-Picard iteration scheme [41] to solve equation (1) iteratively. Among different options available in HYDRUS-1D the following constitutive relations of Van Genuchten [42] has been used.

$$\theta(\psi) = \theta_r + \frac{\theta_s - \theta_r}{(1 + (\alpha\,\psi)^{\lambda})^{\phi}} \tag{2}$$

$$K(\psi) = K_s S_e^{\frac{1}{2}}\left(1 - \left(1 - S_e^{\frac{1}{\phi}}\right)^{\phi}\right)^2 \quad \text{where} \quad \phi = 1 - \frac{1}{\lambda}, \quad \lambda > 1 \tag{3}$$

$$S_e = \frac{\theta - \theta_r}{\theta_s - \theta_r} \tag{4}$$

where S_e is effective saturation [L^3L^{-3}], θ_s and θ_r are saturated and residual water contents, respectively [L^3L^{-3}], α is the inverse of air-entry value [L^{-1}], ϕ and λ are pore size distribution indices and K_s is the saturated hydraulic conductivity [LT^{-1}]. Root water uptake module of HYDRUS-1D [43] employs the following equation to obtain non-compensated actual root water uptake.

$$RWU(\psi, z, t) = \alpha_s(\psi, z, t)\;\; b(z, t)\; T_p(t) \tag{5}$$

where, $\alpha_s(\psi,z,t)$ is the stress response function, b is the 1D normalized water uptake distribution function [L^{-1}] and T_p is the potential transpiration rate [LT^{-1}]. In this part of the study, normalized water uptake distribution function of Hoffman and van Genuchten [44] and stress response function of Feddes [45] have been employed which are demonstrated by equation (6) and (7).

$$b(z) = \begin{cases} \dfrac{1.6667}{L_R} & z > L - 0.2L_R \\ \dfrac{2.0833}{L_R}\left(1 - \dfrac{L - z}{L_R}\right) & L - L_R < z < L - 0.2L_R \\ 0 & z > L - 0.2L_R \end{cases} \tag{6}$$

$$\alpha(h) = \begin{cases} \dfrac{h - h_4}{h_3 - h_4} & h_4 < h \le h_3 \\ 1 & h_3 < h \le h_2 \\ \dfrac{h - h_1}{h_2 - h_1} & h_2 < h \le h_1 \\ 0 & h \le h_4 \; or \; h > \; h_1 \end{cases} \tag{7}$$

where L is equal to the total depth of soil which is intended to be simulated [L], L_R is maximum root depth [L] and h_1, h_2, h_3, and h_4 are pressure head threshold parameters [L]. Equation (1) is a partial differential equation requiring initial condition and two boundary conditions. Initial soil moisture was measured during the experiment by means of soil moisture sensors installed in the observation wells. The lower boundary condition was set as free drainage boundary and the upper boundary (at soil surface) was set as atmospheric boundary condition. This requires the variations of potential evaporation rate to be specified during the experiment. To this end, potential evapotranspiration rate (ET_P [LT^{-1}]) was calculated following the recommendations of Ref. [46].

During the iterative process of solving Richards' equation, HYDRUS-1D calculates the distribution of pressure head in the soil profile at each time step. Therefore, water flux q [$L^3L^{-2}T^{-1}$] can be computed at an arbitrary nodal point by discretizing Darcy-Buckingham equation.

$$q = -K(\psi)\frac{d\psi}{dz} \tag{8}$$

where, positive and negative fluxes at each node means upward and downward movement of water in the soil profile, representing *ET* and *DP* respectively.

2.2.2.2. Modified Soil Moisture Analytical Relationship (MSMAR)

Ref. [12] presented the novel Soil Moisture Analytical Relationship (SMAR) model to define a soil water balance relationship in a two-layered soil profile in which infiltration is the most important flux between the two layers and other processes, such as lateral flow and capillary rise are assumed negligible. The Infiltration is not expressed as a function of precipitation, but as a function of the percentage of soil moisture in the first layer which allows to obtain soil moisture in the second layer as a function of soil moisture in the top layer:

$$n_1 Zr_1 y(t) = n_1 Zr_1 y[s_1(t), t] \;\; = \;\; n_1 Zr_1 \begin{cases} (s_1(t) - s_{c1}), & s_{c1} < s_1(t) \\ 0, & s_1(t) \le s_{c1} \end{cases} \tag{9}$$

where $y(t)$ [–] is the fraction of soil saturation infiltrating in the lower layer, n_1 [–] is the soil porosity, Zr_1 [L] is the depth, s_1 (θ_1/n_1) [–] is the relative saturation, and s_{c1} [–] is the value of relative saturation at field capacity of the first layer of soil. The flux from the top layer is only considered significant if the moisture content is higher than the field capacity and it occurs in less than one day following the Green-Ampt infiltration relationship [47]. By defining $x_2 = (s_2\text{-}s_{w2})/(1\text{-}s_{w2})$ as the effective relative saturation of the second layer of soil and $\omega_0 = (1\text{-}s_{w2})\, n_2 Zr_2$ as the soil water storage, the SMAR soil water balance is described as:

$$(1 - s_{w2}) n_2 Zr_2 \; \frac{dx_2(t)}{dt} = n_1 Zr_1 y(t) - V_2 x_2(t) \tag{10}$$

where s_2 [–] is current relative saturation, s_{w2} [–] is relative saturation at the wilting point, n_2 [–] is soil porosity, Zr_2 [L] is soil depth, V_2 [LT^{-1}] is soil water loss coefficient accounting for both evapotranspiration and percolation losses, and x_2 [–] is effective relative soil saturation of the second soil layer. The second term of the right side of the Eq. (11) represents a linear soil water loss function where soil water loss would be linearly reduced from a maximum value at the saturation point to zero at the wilting point (Fig. 1).

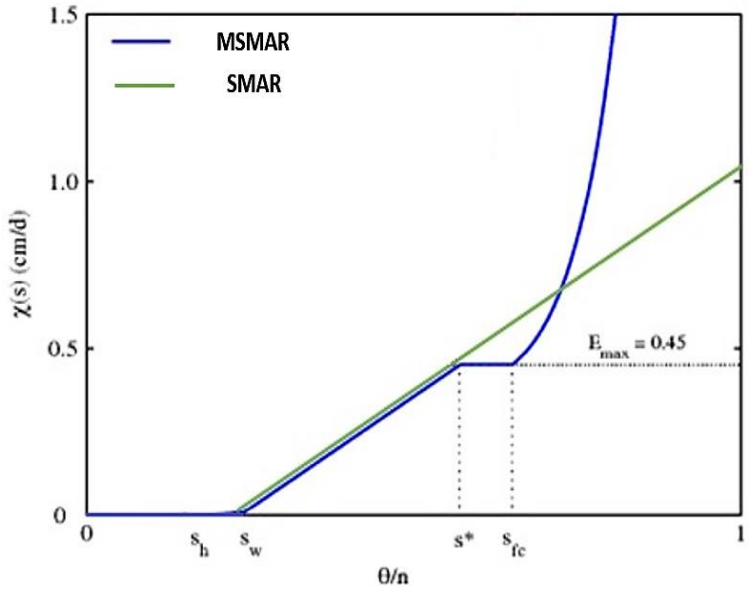

Figure 1. Typical water loss function (*L(s)*) of SMAR model (green), and MSMAR model (blue) for the typical climate, soil and vegetation conditions in arid and semi-arid regions.

Ref. [24] presented the Modified SMAR (MSMAR) model by substituting the constant V_2 with a variable coefficient $L(s_2)$ which estimates a different maximum soil water loss in each day as a function of potential *ET* and *DP* in that day:

$$L(s_2) = ET(s_2) + DP(s_2) \tag{11}$$

where at a certain soil saturation in the second layer (s_2), $L(s_2)$ [LT^{-1}] is the total soil water loss, $ET(s_2)$ [LT^{-1}] is soil water loss due to evapotranspiration, and $DP(s_2)$ [LT^{-1}] is soil water loss due to deep percolation. According to Liao et al. (2001), the maximum DP occurs under saturated conditions and decreases exponentially with decreasing soil hydraulic conductivity from K_s at saturation point to zero at field capacity:

$$DP\ (s_2) = \begin{cases} K_s s_2^c & s_{c2} < s_2 \leq 1 \\ 0 & s_{w2} < s_2 \leq s_{c2} \end{cases} \tag{12}$$

where K_s [LT^{-1}] is hydraulic conductivity of soil saturation and c [-] is the empirical parameter of power function. The amount of loss due to evapotranspiration was also calculated from the following equation [48]:

$$ET(s_2) = \begin{cases} ET_{max} & s_2^* < s_2 \leq 1 \\ ET_w + (ET_{max} - ET_w)\dfrac{s_2 - s_{w2}}{s^* - s_{w2}} & s_{w2} < s_2 \leq s_2^* \end{cases} \tag{13}$$

where s_w [–] is the degree of saturation at the wilting point, s^* [–] is the degree of saturation at the stomata closure, ET_{max} [LT^{-1}] is the potential evapotranspiration and ET_w [LT^{-1}] is the evapotranspiration at the wilting point. The water loss function of the MSMAR can be compared with that of SMAR in Fig.1. In this regard, $L(s_2)$ can be replaced with V_2 to account for non-linearity of the soil water loss and the Eq. 11 becomes:

$$(1 - s_{w2}) n_2 Z r_2 \frac{dx_2}{dt} = n_1 Z r_1 y(t1) - L(s_2) x_2(t) \tag{14}$$

Equation (15) can be redefined using the coefficients *a* and *b* as follows:

$$a = \frac{L(s_2)}{(1 - s_{W2}) n_2 Z r_2} \ , \ b = \frac{n_1 Z r_1}{(1 - s_{W2}) n_2 Z r_2} \tag{15}$$

The value of these parameters can be directly related to the depth of the two layers and the soil water loss coefficient. As a result, the soil water balance relationship becomes:

$$\frac{dx_2(t)}{dt} = by(t) - ax_2(t) \tag{16}$$

Assuming an initial condition for relative saturation $x_2(t)$ equal to zero, the analytical solution for this linear differential equation is:

$$x_2(t) = \int_0^t b\, e^{a(t'-t)} y\,(t')dt' \tag{17}$$

For practical applications, the relationship can be represented discretely:

$$x_2(t_j) = \sum_{i=0}^{j} b\, e^{a(t_i-t_j)} y\,(t_i)\Delta t \tag{18}$$

Assuming $\Delta t = (t_{(j)}\text{-}t_{(j-1)})$ and extending the Eq.18, the following equation is obtained for soil moisture in the second layer based on the time series of surface soil moisture:

$$x_2(t_j) = x_2(t_{j-1})e^{-a(t_j-t_{j-1})} + by(t_j)(t_j - t_{j-1}) \tag{19}$$

And it can be rewritten as a function of s_2 as follows:

$$s_2(t_j) = s_{w2} + (s_2(t_{j-1}) - s_{w2})e^{-a(t_j - t_{j-1})} + (1 - s_{w2})by(t_j)(t_j - t_{j-1}) \tag{20}$$

The main parameters of MSMAR model includes Zr_1, Zr_2, n_1, n_2, s_{c1}, s_{c2}, s_2^*, s_{w2}, K_s, c, ET_{max} and ET_w. Since there is a clear physical meaning to each of these parameters, they can be determined according to the soil texture using reference tables in the literature (e.g. [12,23,48]) or can be calibrated based on the field data.

2.2.3. Study area

For the purpose of this research, the information presented by Ref. [38] was exploited including the soil moisture measurements, meteorological data, soil physical properties, volume of applied irrigation water, and cultivation dates. The study area in this research is a 17 ha 'Triticale' farm, (F) under sprinkler irrigation near Neishabour (58° 39' 2" E and 36° 11' 3" N), Iran (Fig. 2 a&b). Triticale is a hybrid of wheat and rye with the maximum rooting depth of 100 cm and soil water depletion fraction of 0.55, which is the average fraction of Total Available Soil Water (TAW) that can be depleted from the root zone before moisture stress (reduction in ET) occurs (Allen et al., 1998). The annual average precipitation and potential evapotranspiration are 247 and 2,335 mm, respectively. The highest and lowest monthly-averaged precipitations, fall in March and August whose values are 51 and 0.16 mm, respectively.

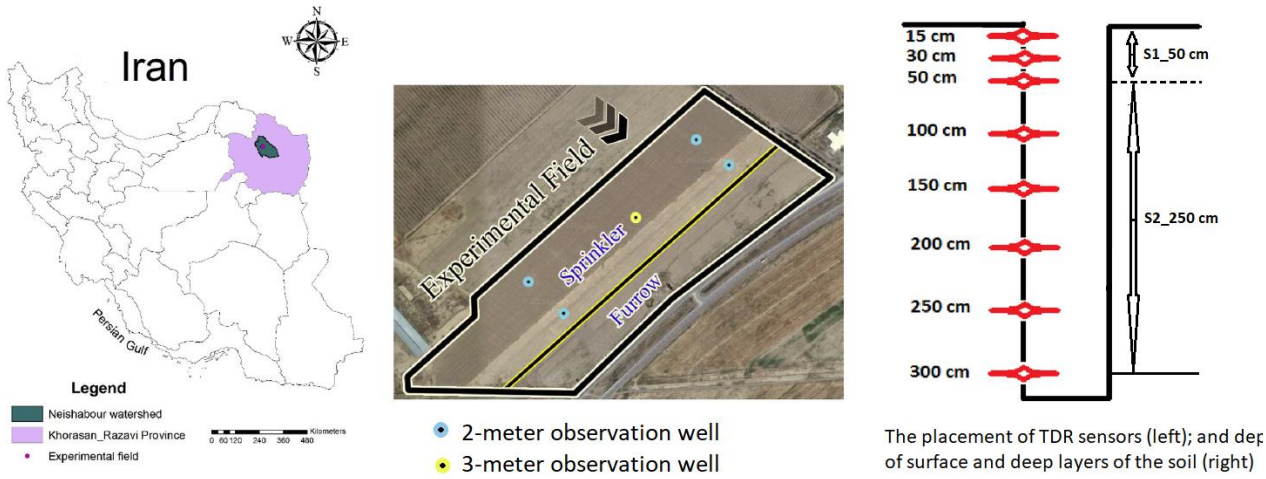

(a) (b) (c)

Figure 2. (**a**) Location of study farm in Neishabour watershed and (**b**) layout of sprinkler and furrow irrigation systems along with the locations of two- and three-meter-deep monitoring wells (**c**) schematic diagram showing the installation of soil moisture sensors into the monitoring wells (adopted from Ref. [38]).

2.2.4. Data

The daily soil moisture profile in the study area was monitored via 5 observation wells (Fig. 2b) equipped with 8 REC® TDR sensors [38] installed down to 3 m to achieve a high resolution dataset in the root zone (Fig. 2c). Several soil samples were obtained whilst drilling the observation wells, which were analyzed in the Laboratory of Water Science and Engineering Department of Ferdowsi University of Mashhad (FUM) to determine the soil parameters and water content of different soil layers in the field. Sensor calibration had been performed following the procedure outlined in Ref. [39] and the regression equation between the calibrated and measured soil water contents ($y = 0.9959x + 0.0007$; $R^2 = 0.947$) showed the accuracy of TDR sensors. These data were also used to set up initial conditions of the models, and validate the simulation results. The overall status of the soil water content in the field was then calculated by the arithmetic average of the TDR values obtained from the five monitoring wells (i.e. spatial average). Table 1 summarizes the results of the soil physical properties.

Table 1. Soil physical properties of experimental plots at different layers.

Soil depth (cm)	Soil mineral particles (%)			Soil texture (USDA Classification)	ρb[a] [g/ cm^3]	SVWC[b] (%)	θ_s*	K_s * [cm/day]
	sand	silt	clay					
0 – 50	29.08	30.00	40.92	Clay loam	1.60	42	0.4418	3.84
50 – 100	44.25	34.65	21.10	Loam	1.52	34	0.3991	9.30
100 – 150	32.75	35.75	31.50	Clay Loam	1.65	41	0.4418	2.81
150 – 200	61.00	26.75	12.25	Sandy Loam	1.50	36	0.387	31.62
200 – 250	68.50	19.50	12.00	Sandy Loam	1.61	32	0.387	28.41
250 – 300	55.60	24.40	20.00	Sandy Loam	1.56	36	0.387	13.99

Note. [a] Bulk density. [b] Saturated Volumetric Water Content. * The calibrated parameters of van Genuchten's water retention model.

2.2.5. Results

In order to run HYDRUS-1D, the initial guess for soil hydraulic parameters were obtained using RETC [49] and ROSETTA [50] software based on the soil texture measurements (table 1). These values were fine-tuned in the calibration phase to improve the accuracy of simulations. Root water uptake parameters of Feddes' function [45] were selected from Ref. [51]. The rooting depth of the Triticale was assumed to be 1 m and the effect of salinity was assumed to be negligible since soil and water quality samples showed an average of 2.89 and 2.24 $dS.m^{-1}$ on the region, respectively. The HYDRUS-1D simulated the soil water balance of the Triticale field for a period of six months starting from sowing to harvest date (01/11/2012- 22/04/2013).

The parameters of MSMAR model were calibrated using Genetic Algorithm in the MATLAB software (https://www.mathworks.com/discovery/genetic-algorithm.html) with the objective function of minimum RMSE between the observed and estimated soil moisture values. The sensitivity of MSMAR model to the depth of surface layer was assessed by assuming three different combinations of soil layers (Zr1/Zr2 = 15/285, 30/270 and 50/250 [cm/cm]). In the case of Zr1/ Zr2 = 50/250 cm (figure 1c), for example, $S1_{50cm}$ is the weighted average of TDR measurements at the depths of 15, 30, and 50 cm; whereas, $S2_{50cm}$ is the weighted average of the TDR measurements at the depths of 100, 150, 200, 250 and 300 cm. The calibrated parameters of all layer combinations are presents in table (2) which are largely consistent with the correspondent values in table 1. The daily ET_{max} was assumed to be equal to the potential evapotranspiration (ET_p) and estimated by FAO dual crop coefficient method (see section 3.2). ET_w was assumed to be a constant value equal to 0.001 cm/day.

Table 2. MSMAR calibrated parameters for different surface and deep layer depths using GA in MATLAB based on the minimum RMSE with observed data.

Surface layer	soil depth [cm]	s_{c1} [-]	s_{w2} [-]	s_{c2} [-]	n_1 [-]	n_2 [-]	K_s [cm/day]	c [-]	s_2^*[-]
S1_15cm	30	0.758	0.598	0.899	0.441	0.441	3.978	14.450	0.838
	50	0.725	0.525	0.700	0.441	0.441	2.389	17.337	0.665
	100	0.701	0.587	0.841	0.441	0.406	9.987	11.027	0.790
	150	0.899	0.518	0.894	0.441	0.407	9.956	11.075	0.819
	200	0.879	0.229	0.751	0.441	0.412	9.507	16.051	0.647
	250	3.52E-16	1.67E-16	0.9	0.441	0.441	1	26	0.72
	300	0.900	0.106	0.527	0.441	0.431	31.907	11.040	0.443
S1_30cm	30	-	-	-	-	-	-	-	-
	50	0.730	0.599	0.988	0.471	0.488	3.986	11.058	0.910
	100	0.730	0.089	0.993	0.471	0.501	9.993	11.010	0.812
	150	0.730	0.157	0.643	0.471	0.487	1.510	16.708	0.546
	200	0.730	0.005	0.953	0.471	0.407	26.778	12.091	0.764
	250	0.730	0.000	0.587	0.471	0.405	28.991	11.003	0.470
	300	0.730	1.24E-08	0.208	0.471	0.398	13.997	11.000	0.166
S1_50cm	30	-	-	-	-	-	-	-	-
	50	-	-	-	-	-	-	-	-
	100	0.839	0.465	0.804	0.434	0.464	14.153	14.483	0.736
	150	0.839	0.464	0.564	0.434	0.462	18.121	13.956	0.544
	200	0.839	0.203	0.831	0.434	0.500	12.372	15.628	0.705
	250	0.839	0.139	0.561	0.434	0.493	10.210	15.807	0.477
	300	0.839	0.207	0.436	0.434	0.435	14.965	15.446	0.390

In the following three separate sections, the results of MSMAR and HYDRUS-1D models in estimating Soil Moisture (SM), Evapotranspiration (ET) and Deep Percolation (DP) were discussed in details:

2.2.5.1. Soil moisture content

The soil moisture profiles of the Triticale farm during the growth period were generated using the average TDR values with the same depth over the field (Fig. 3a), the SM results of HYDRUS-1D (Fig. 3b), and the SM results of MSMAR model (Fig. 3c). In order to investigate the effects of infiltrated water on the SM profiles, the precipitations and irrigation events were illustrated in Fig. 3d. The TDR data was not available during some of the precipitations and irrigation events which leaded to losing some information about the dynamics of SM profile. Nevertheless, Fig.3 shows that these events could effectively recharge the soil profile to the field capacity point ($\approx 0.4\ [cm/cm]$) down to the Triticale root zone (100 cm). Comparing the SM profiles reveals that infiltration process in MSMAR was sudden (on the same day as the precipitation or irrigation), while it was smoother for the HYDRUS-1D. The fluctuations and level of soil saturation decreased dramatically beneath the root zone, indicating the significance of root water uptake.

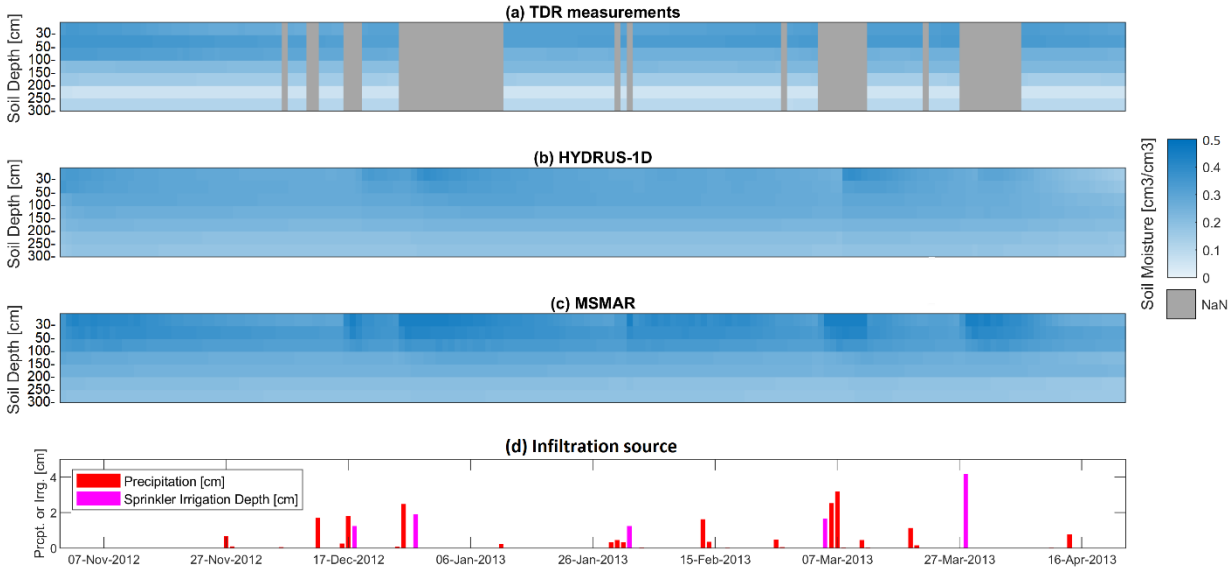

Figure 3. SM profile for **(a)** the average TDR values with the same depth over the field, **(b)** the HYDRUS-1D results, **(c)** the MSMAR results, as well as **(d)** precipitation and irrigation events during the growth period of Triticale between 01/11/2012 and 21/04/2013. **(a-c)** have the same color map scales.

In order to be able to evaluate the SM results of MSMAR, the TDR measurements at different depths were averaged according to the MSMAR layer combinations (as explained earlier) to produce an overall status of the soil profile. The SM results of HYDRUS-1D were presented as they were, though, since this model intrinsically considers the whole soil profile when generating the results. Figures 4, 5 and 6 illustrate the SM time series of MSMAR, HYDRUS-1D, and TDR measurements at different depths (30, 50, 100, 150, 200, 250, and 300 cm) when the surface layer is 15, 30 and 50 cm, respectively. Not surprisingly, the soil moisture fluctuations are relatively extreme within topsoil layers especially after the precipitation or irrigation events. The amplitude of SM spikes dampened and reached a monotonous trend in the deeper soil layers.

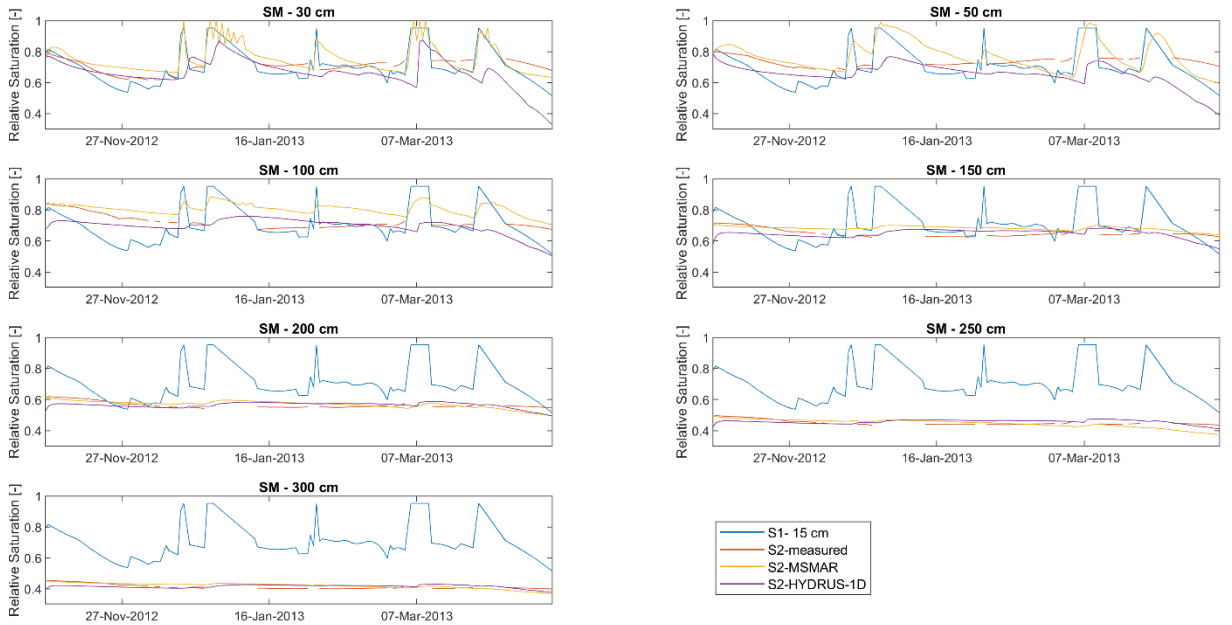

Figure 4. The time series of relative saturation in the soil profile assuming that the surface layer is 15 cm. (Blue) TDR measurements in the surface layer; (Red) TDR measurements in the deep layer; (Yellow) MSMAR estimates in the deep layer; and (Purple) HYDRUS-1D estimates in the deep layer.

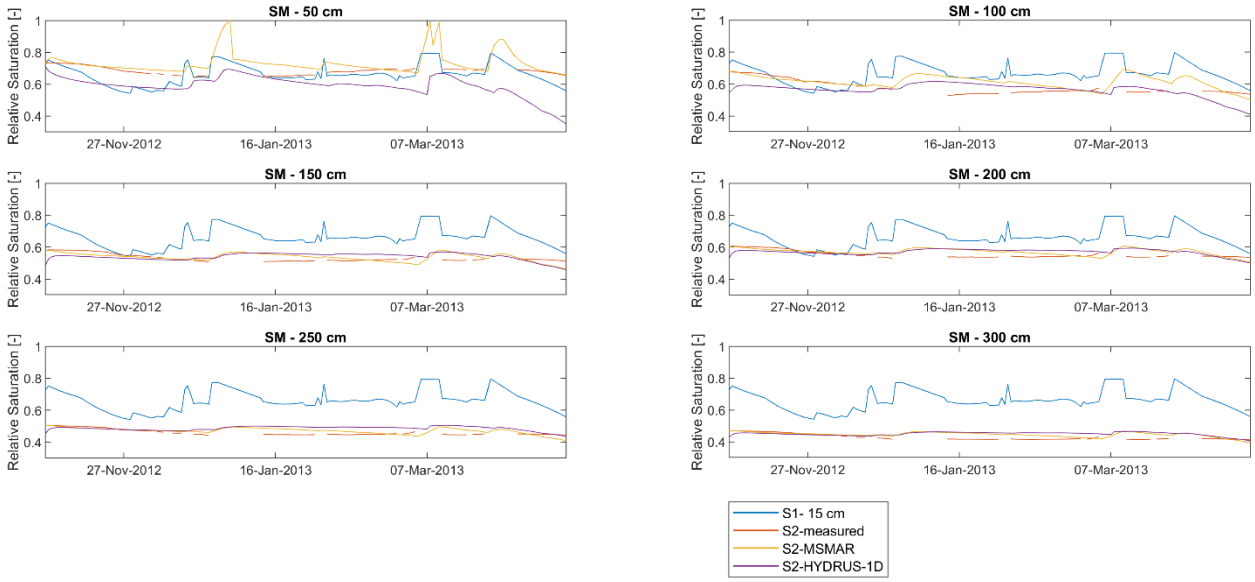

Figure 5. The time series of relative saturation in the soil profile assuming that the surface layer is 30 cm. (Blue) TDR measurements in the surface layer; (Red) TDR measurements in the deep layer; (Yellow) MSMAR estimates in the deep layer; and (Purple) HYDRUS-1D estimates in the deep layer.

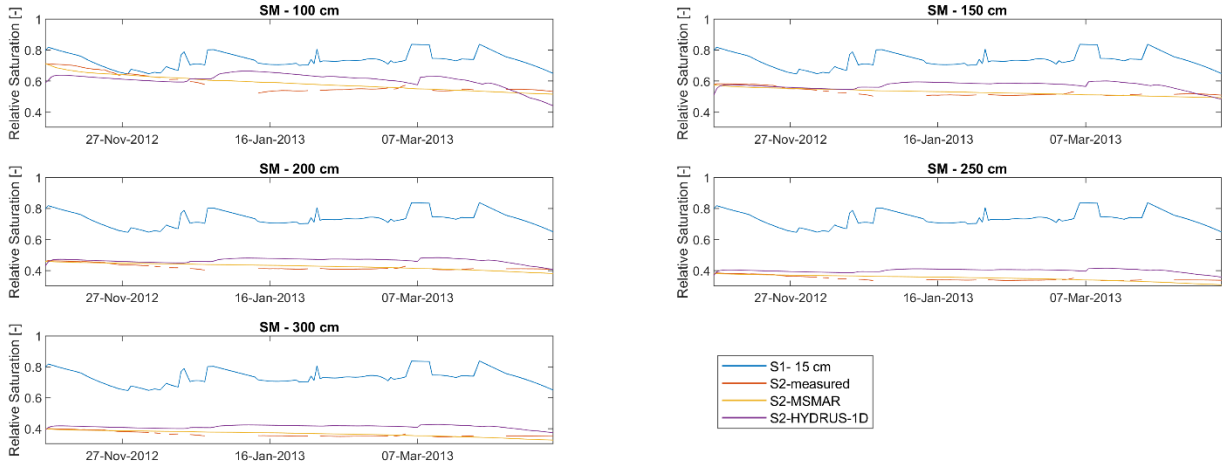

Figure 6. The time series of relative saturation in the soil profile assuming that the surface layer is 50 cm. (Blue) TDR measurements in the surface layer; (Red) TDR measurements in the deep layer; (Yellow) MSMAR estimates in the deep layer; and (Purple) HYDRUS-1D estimates in the deep layer.

Table 3. represents the values of Root Mean Square Error (RMSE) and coefficient of determination (R^2) between the SM estimates of MSMAR and HYDRUS-1D models to provide a quantitative interpretation of the MSMAR performance. According to the Table 3, the MSMAR had an overall average RMSE = 0.069 cm^3/cm^3 and R^2 = 0.39 with the SM estimates of HYDRUS-1D of all three layer ratios, which is quite acceptable. However, the MSMAR was more consistent with the HYDRUS-1D when Zr_2>100 cm (average RMSE = 0.079 cm^3/cm^3 and R^2 = 0.47), than $Zr_2 \leq 100$ cm (average RMSE = 0.051 cm^3/cm^3 and R^2 = 0.23). The MSMAR was also the most consistent with the HYDRUS-1D when Zr_1 = 50 with average RMSE = 0.058 cm^3/cm^3 and R^2 = 0.59.

Table 3. RZSM and R^2 values between the SM results of Hydrus-1D and MSMAR.
* S1_15cm means the surface layer has been considered 15 cm

Soil depth		**30 cm**	**50 cm**	**100 cm**	**150 cm**	**200 cm**	**250 cm**	**300 cm**
		RMSE [cm^3/cm^3]						
MSMAR	**S1_15cm***	0.051	0.066	0.052	0.050	0.087	0.126	0.086

	S1_30cm	-	0.082	0.034	0.039	0.085	0.124	0.082
	S1_50cm	-	-	0.022	0.029	0.067	0.107	0.064
				R^2 [-]				
	S1_15cm	0.482	0.274	0.159	0.297	0.074	0.926	0.675
MSMAR	**S1_30cm**	-	0.049	0.220	0.164	0.052	0.414	0.295
	S1_50cm	-	-	0.178	0.860	0.207	0.914	0.775

2.2.5.2. Evapotranspiration

In order to estimate the potential evapotranspiration (ET_P), the FAO dual crop coefficient method was employed because of its performance on daily basis as results of a dynamic soil evaporation coefficient rather than an average value [52]. Also, Ref. [46] reported that after precipitations or irrigations, dual crop coefficient approach had better ET estimations. In the current study, the data provided by Ref. [46] and field observations were used to specify crop coefficient values and length of four growth stages. i.e., initial, crop development, mid-season, and late season stages. The basal crop coefficient values of mid-season and late season were then adjusted for local climatic conditions and the mean plant height at each stage. The variation of plant height was estimated using Richards' function [53] which is a well-known S-shaped function commonly used for modeling plant growth. The initial value of plant height at sowing time (November 1, 2012) was set to zero. The function asymptotically approached to the maximum plant height which was assumed to be 1m herein for Triticale. Table 4 shows the adjusted crop coefficients and the length of each growth stage used in this part of the study. Figure 7 illustrates the time series of ET_p in our Triticale study farm calculated by FAO dual coefficient method [46].

Table 4. Crop coefficient values and length of growth stages for Triticale.

Crop	**Crop coefficient (K_{cb})**			**Length of growth stages (day)**			
Triticale	$K_{cb\ ini}$	$K_{cb\ mid}$	$K_{cb\ end}$	L_{ini}	L_{dev}	L_{mid}	L_{late}
	0.5	1.16	0.25	30	120	60	30

The daily actual evapotranspiration (ET_a) of MSMAR model was calculated by Eq. (13) assuming Zr_1 = 15, 30, and 50 cm (Fig. 7a-c). However, the HYDRUS-1D computed the actual evaporation and transpiration separately at the upper boundary of soil profile governed by atmospheric condition, and the sum of these parameters produced ET_a. Actual transpiration was calculated by integrating nodal actual root water uptake (Eq. (5)) at each time step over the root zone.

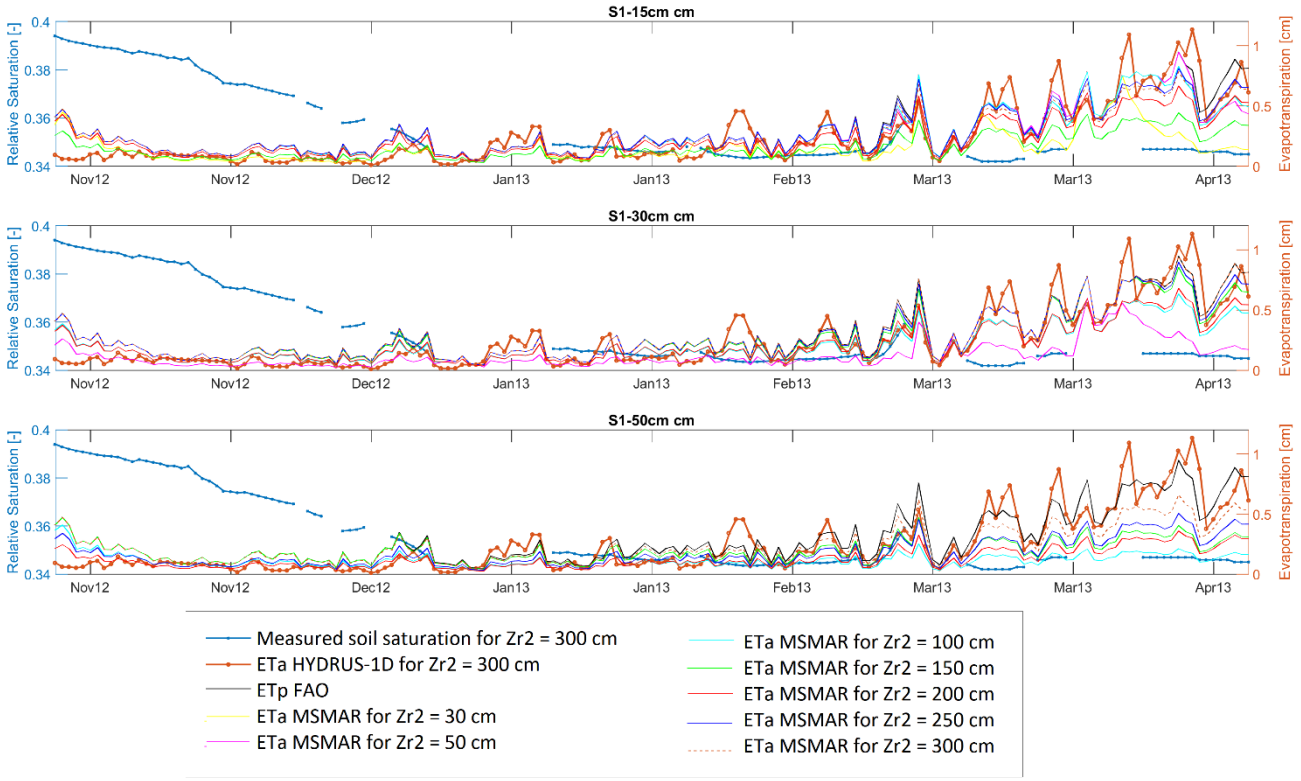

Figure 7. The time series of ET_p by FAO dual crop coefficient method; ET_a by HYDRUS-1D from the surface of the soil, and ET_a by MSMAR for Zr_2 = 30 to 300 cm when **(a)** Zr_1 = 15 cm, **(b)** Zr_1 = 30 cm, and **(c)** Zr_1 = 50 cm.

According to Fig. 7, ET_p rises at the beginning of spring due to the increase in the solar radiation, resulting in the depletion of soil water content (S_2). ET_a estimated by HYDRUS-1D and MSMAR follow the same pattern with a distance from ET_p resulted from water deficit in the soil. The RZSM and R2 values between the ET estimates of Hydrus-1D and MSMAR are presented in Table 5. According to the Table 5, the MSMAR model was in good agreement and HYDRUS-1D in estimating the daily actual evapotranspiration (ET_a) for all of Zr_1 and Zr_2 combinations, with the average RMSE = 0.173 cm/day and R2 = 0.649. Moreover, the performance of MSMAR improved as Zr_1 and/or Zr_2 increases.

Table 5. RZSM and R^2 values between the ET results of Hydrus-1D and MSMAR simulations.

	30 cm	**50 cm**	**100 cm**	**150 cm**	**200 cm**	**250 cm**	**300 cm**
				RMSE [cm/day]			
S1_15cm	0.231	0.141	0.143	0.199	0.150	0.137	0.138
S1_30cm	-	0.233	0.153	0.131	0.145	0.130	0.130
S1_50cm	-	-	0.273	0.216	0.228	0.186	0.157
				R^2 [-]			
S1_15cm	0.294	0.723	0.711	0.730	0.732	0.747	0.744
S1_30cm	-	0.477	0.752	0.765	0.769	0.772	0.776
S1_50cm	-	-	0.164	0.420	0.709	0.712	0.689

2.2.5.3. Deep percolation

HYDRUS-1D yields DP at each control volume by means of Darcy-Buckingham flux using pressure head distribution obtained at each time step, while MSMAR estimates this parameter as a function of water content and hydraulic conductivity of the second layer of the soil following Eq. 12. Figures 8-10 represent the estimated DP by HYDRUS-1D and MSMAR models at different depths (30, 50, 100, 150, 200, 250, and 300 cm) when the surface layer is 15, 30 and 50 cm, respectively.

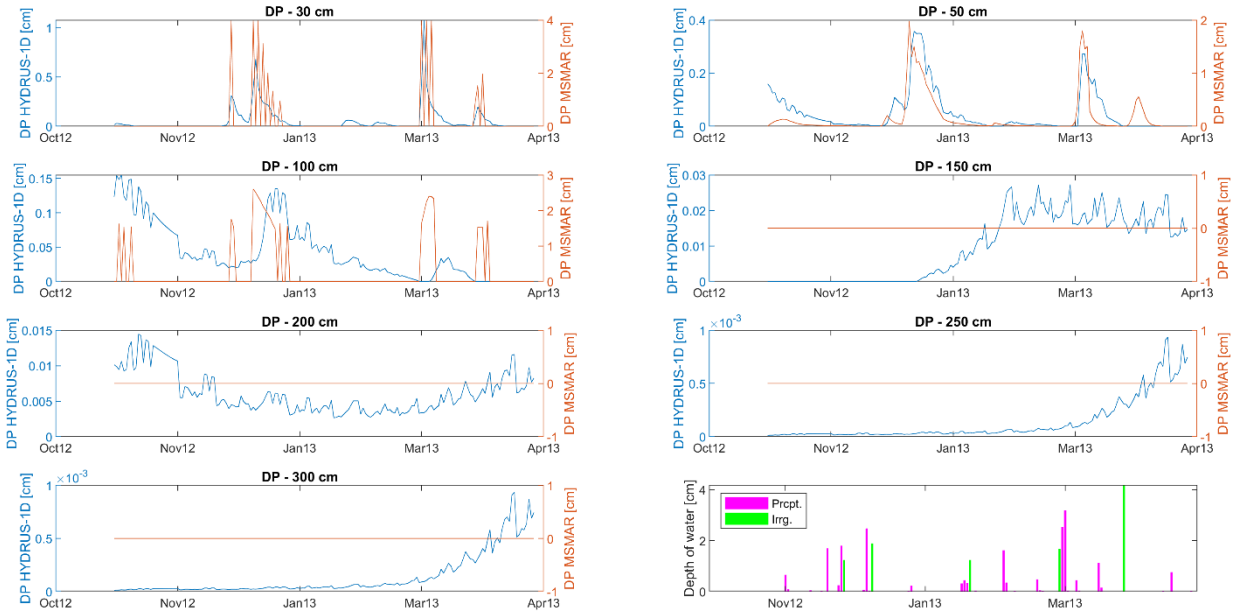

Figure 8. The time series of DP estimates of HYDRUS-1D and MSMAR (with Zr_1 = 15 cm) at Zr_2 = 30-300 cm; as well as the bar chart of precipitations and irrigation events.

Fig.8 illustrates that when Zr_1 = 15 cm, the MSMAR can produce consistent DP estimates with those of HYDRUS-1D down to Zr_2 = 50 cm, and yet capture the DP dynamics in the soil down to Zr_2 = 100 cm.

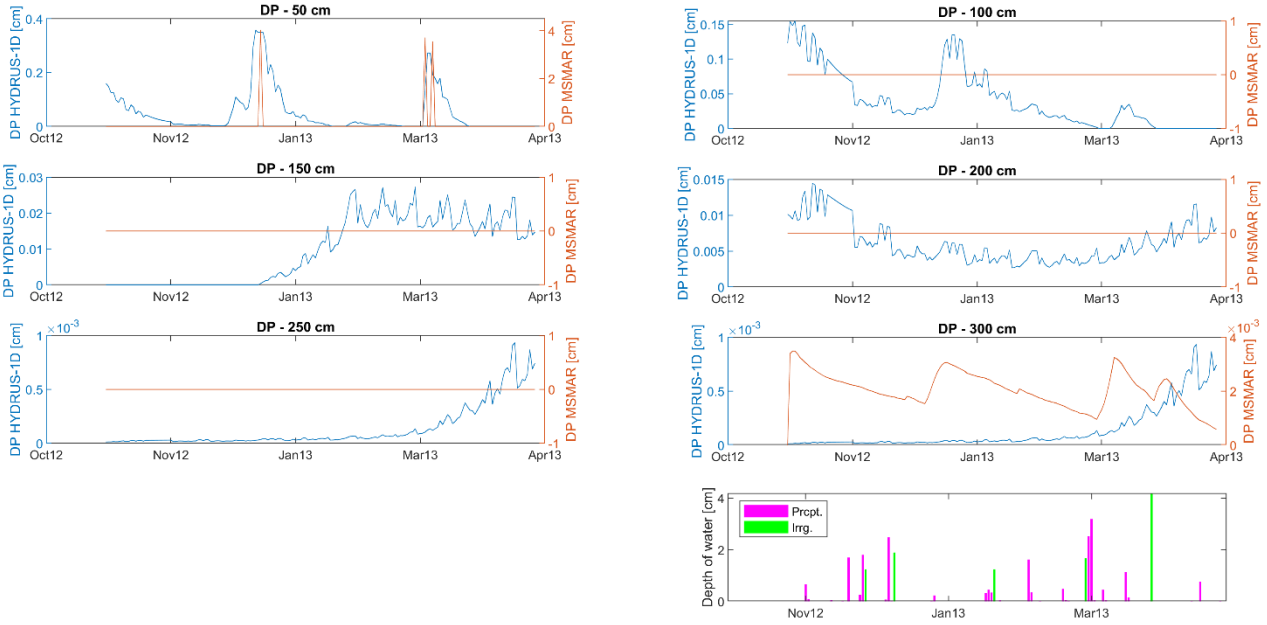

Figure 9. The time series of DP estimates of HYDRUS-1D and MSMAR (with Zr_1 = 30 cm) at Zr_2 = 50-300 cm; as well as the bar chart of precipitations and irrigation events.

Inspecting Figures 8-10 reveals that not only MSMAR model estimated no DP for Zr_2 > 100 cm (except for Zr_2 = 300 cm in Fig. 9), but also HYDRUS-1D estimated very small DP values which could be neglected. According to Eq. (12), Figures (4-6) and Table 2, the water content of soil layers with Zr_2 > 100 cm were always lower than the field capacity during the study period leaded to estimating no DP in the MSMAR model. The results also showed that increasing the depth of surface layer decreased the sensitivity of MSMAR model in capturing the DP dynamics of the soil, which might be due to the same reason but for the concept of infiltration in Eq. 9.

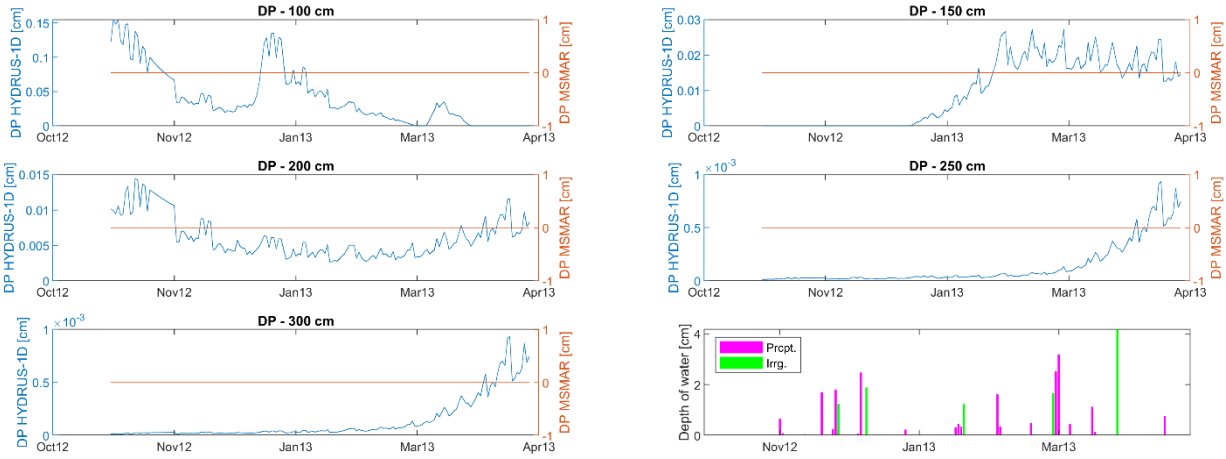

Figure 10. The time series of DP estimates of HYDRUS-1D and MSMAR (with Zr_1 = 50 cm) at Zr_2 = 100-300 cm; as well as the bar chart of precipitations and irrigation events.

The total RMSE and R^2 values between the DP results of HYDRUS-1D and MSMAR simulations are presented in table 6. Table 6 represents that the best performance of MSMAR model in estimating DP was at Zr_1 = 15 cm and Zr_2 = 50 cm with RMSE = 0.32 cm, and R^2 = 0.7.

Table 6. RZSM and R^2 values between the DP results of Hydrus-1D and MSMAR simulations.

	30 cm	**50 cm**	**100 cm**	**150 cm**	**200 cm**	**250 cm**	**300 cm**
				RMSE [cm/day]			
S1_15cm	0.746	0.323	0.742	0.013	0.007	0.000	0.001
S1_30cm	-	0.469	0.058	0.013	0.007	0.000	0.002
S1_50cm	-	-	0.058	0.013	0.007	0.000	0.001
				R^2[-]			
S1_15cm	0.39	0.70	0.01	0.00	0.00	0.00	0.00
S1_30cm	-	0.14	0.00	0.00	0.00	0.00	0.01
S1_50cm	-	-	0.00	0.00	0.00	0.00	0.00

2.2.6. Discussion

In this paper the ability of the MSMAR model in estimating SM, ET and DP was evaluated with the well-known HYDRUS-1D model in a study *Triticale* farm with the sprinkler irrigation system in an arid region of Iran. MSMAR is an analytical solution for the water balance in a soil composed of two layers, whereas HYDRUS-1D is a software for numerical simulation of saturated/unsaturated water flow within a continuous soil profile using 1D Richards' equation. Field data within the deep vadose zone (3 m) was provided for about six month using one three-meter-deep and four two-meter deep monitoring wells equipped with TDR sensors. In order to investigate the effect of the surface layer depth on the performance of MSMAR, this model was run assuming three different depths (15, 30 and 50 cm) for the surface layer. Having the soil texture measurements, the RETC and ROSETTA software were used to estimate the initial guess for soil hydraulic parameters of HYDRUS-1D. A genetic algorithm in MATLAB was also used to calibrate the MSMAR based on the minimum error with the TDR measurements.

The results showed that the MSMAR was consistent with the HYDRUS-1D in estimating the daily actual evapotranspiration (Average RMSE = 0.173 cm/day and R^2 = 0.649 for all Zr_1 and Zr_2 combinations). Also, the MSMAR was more accurate as Zr_1 or Zr_2 increased. The performance of MSMAR in estimating soil moisture content was also acceptable with the average RMSE = 0.069 cm3/ cm3 and R^2 = 0.39 for all Zr_1 and Zr_2 combinations. The MSMAR model was successful in simulating deep percolation after the precipitations and irrigation events when Zr_1 = 15 cm and Zr_2 = 50 cm (RMSE = 0.32 cm, and R^2 = 0.7), and capturing the DP dynamics for Zr_2 =100 cm. The first layer of MSMAR model acts as the driving force for the water movement into the second layer. So it was assumed that by increasing the depth of first layer, more real-world

phenomena would be integrated and incorporated into MSMAR model and therefore it was expected that MSMAR yield more accurate results in the second layer. However, the results showed that increasing the depth of surface layer did not improve the performance of the MSMAR significantly. It should be noted that the MSMAR model had not been calibrated to produce minimum discrepancies with the HYDRUS-1D, and yet it succeeded in producing relatively consistent results using a few input parameters and low computational requirements.

2.2.7. Conclusions

It can be concluded that MSMAR model has the advantage of implementing a few inputs (including the time series of surface soil moisture and some information about the soil and climate of the study region) and producing valuable information about the hydraulic components of the root zone (i.e. SM, ET and DP) in different spatial scales depending on the utilization of in-situ or remotely sensed SM data, which gives a great promise for different environmental sectors (e.g. agriculture and water resource management) especially in the developing countries and ungauged regions. For the future works, it is suggested to improve the performance of MSMAR model by devising a more sophisticated calibration plan, or to couple the MSMAR model with other distributed hydrological models (e.g. SWAT, MODFLOW etc.).

2.2.8. References

1. Brunner, P.; Simmons, C.T. HydroGeoSphere: a fully integrated, physically based hydrological model. *Groundwater* **2012**, *50*, 170-176.
2. Vogel, M. Effects of model spin-up on simulated recharge using the Hydrus-1D vadose zone model. 2019.
3. Spelman, D.; Kinzli, K.-D.; Kunberger, T. Calibration of the 10HS soil moisture sensor for southwest Florida agricultural soils. *Journal of Irrigation and Drainage Engineering* **2013**, *139*, 965-971.
4. Vázquez-Suñé, E.; Abarca, E.; Carrera, J.; Capino, B.; Gámez, D.; Pool, M.; Simó, T.; Batlle, F.; Niñerola, J.; Ibáñez, X. Groundwater modelling as a tool for the European Water Framework Directive (WFD) application: The Llobregat case. *Physics and Chemistry of the Earth, Parts A/B/C* **2006**, *31*, 1015-1029.
5. Hillel, D. *Environmental soil physics: Fundamentals, applications, and environmental considerations*; Elsevier: 1998.
6. Lipiec, J.; Tarkiewicz, S. The influence of water content and bulk density on penetration resistance of two soils. *Zeszyty Problemowe Postępów Nauk Rolniczych* **1990**, *388*.
7. Simunek, J.; van Genuchten, M.T.; Sejna, M. Development and applications of the HYDRUS and STANMOD software packages and related codes. *Vadose Zone Journal* **2008**, *7*, 587-600.
8. Zhang, Y.; Zhao, W.; Ochsner, T.E.; Wyatt, B.M.; Liu, H.; Yang, Q. Estimating Deep Drainage Using Deep Soil Moisture Data under Young Irrigated Cropland in a Desert-Oasis Ecotone, Northwest China. *Vadose Zone Journal* **2019**, *18*, 1-10.
9. Langergraber, G.; Simunek, J. Modeling variably saturated water flow and multicomponent reactive transport in constructed wetlands. *Vadose Zone Journal* **2005**, *4*, 924-938.
10. Simunek, J.; Van Genuchten, M.T.; Sejna, M. The HYDRUS-1D software package for simulating the one-dimensional movement of water, heat, and multiple solutes in variably-saturated media. *University of California-Riverside Research Reports* **2005**, *3*, 1-240.
11. Wagner, W.; Lemoine, G.; Rott, H. A method for estimating soil moisture from ERS scatterometer and soil data. *Remote sensing of environment* **1999**, *70*, 191-207.
12. Manfreda, S.; Brocca, L.; Moramarco, T.; Melone, F.; Sheffield, J. A physically based approach for the estimation of root-zone soil moisture from surface measurements. *Hydrology and Earth System Sciences* **2014**, *18*, 1199-1212.
13. Panday, S.; Huyakorn, P.S. MODFLOW SURFACT: A state-of-the-art use of vadose zone flow and transport equations and numerical techniques for environmental evaluations. *Vadose Zone Journal* **2008**, *7*, 610-631.
14. White, M.D.; Oostrom, M.; Rockhold, M.L.; Rosing, M. Scalable modeling of carbon tetrachloride migration at the Hanford site using the STOMP simulator. *Vadose Zone Journal* **2008**, *7*, 654-666.
15. van Dam, J.C.; Groenendijk, P.; Hendriks, R.F.; Kroes, J.G. Advances of modeling water flow in variably saturated soils with SWAP. *Vadose Zone Journal* **2008**, *7*, 640-653.
16. Finsterle, S.; Doughty, C.; Kowalsky, M.; Moridis, G.; Pan, L.; Xu, T.; Zhang, Y.; Pruess, K. Advanced vadose zone simulations using TOUGH. *Vadose Zone Journal* **2008**, *7*, 601-609.
17. Ragab, R. Towards a continuous operational system to estimate the root-zone soil moisture from intermittent remotely sensed surface moisture. *Journal of Hydrology* **1995**, *173*, 1-25.
18. Puma, M.J.; Celia, M.A.; Rodriguez-Iturbe, I.; Guswa, A.J. Functional relationship to describe temporal statistics of soil moisture averaged over different depths. *Advances in Water Resources* **2005**, *28*, 553-566.
19. Sabater, J.M.; Jarlan, L.; Calvet, J.-C.; Bouyssel, F.; De Rosnay, P. From near-surface to root-zone soil moisture using different assimilation techniques. *Journal of Hydrometeorology* **2007**, *8*, 194-206.

20. Albergel, C.; Rüdiger, C.; Pellarin, T.; Calvet, J.-C.; Fritz, N.; Froissard, F.; Suquia, D.; Petitpa, A.; Piguet, B.; Martin, E. From near-surface to root-zone soil moisture using an exponential filter: an assessment of the method based on in-situ observations and model simulations. *Hydrology and Earth System Sciences* **2008**, *12*, 1323-1337.
21. Ochsner, E.; Cosh, M.H.; Cuenca, R.; Hagimoto, Y.; Kerr, Y.; Njoku, E.; Zreda, M. State of the art in large-scale soil moisture monitoring. *Soil Science Society of America Journal* **2013**, 1-32.
22. Baldwin, D.; Manfreda, S.; Keller, K.; Smithwick, E. Predicting root zone soil moisture with soil properties and satellite near-surface moisture data across the conterminous United States. *Journal of Hydrology* **2017**, *546*, 393-404.
23. Faridani, F.; Farid, A.; Ansari, H.; Manfreda, S. Estimation of the root-zone soil moisture using passive microwave remote sensing and SMAR Model. *Journal of Irrigation and Drainage Engineering* **2017**, *143*, 04016070.
24. Faridani, F.; Farid, A.; Ansari, H.; Manfreda, S. A modified version of the SMAR model for estimating root-zone soil moisture from time-series of surface soil moisture. *Water SA* **2017**, *43*, 492-498.
25. Gheybi, F.; Paridad, P.; Faridani, F.; Farid, A.; Pizarro, A.; Fiorentino, M.; Manfreda, S. Soil Moisture Monitoring in Iran by Implementing Satellite Data into the Root-Zone SMAR Model. *Hydrology* **2019**, *6*, 44.
26. Zhuang, R.; Zeng, Y.; Manfreda, S.; Su, Z. Quantifying long-term land surface and root zone soil moisture over Tibetan Plateau. *Remote sensing* **2020**, *12*, 509.
27. An, H.; Ichikawa, Y.; Tachikawa, Y.; Shiiba, M. Three-dimensional finite difference saturated-unsaturated flow modeling with nonorthogonal grids using a coordinate transformation method. *Water Resources Research* **2010**, *46*.
28. An, H.; Yu, S. Finite volume integrated surface-subsurface flow modeling on nonorthogonal grids. *Water Resources Research* **2014**, *50*, 2312-2328.
29. Mansell, R.; Ma, L.; Ahuja, L.; Bloom, S. Adaptive grid refinement in numerical models for water flow and chemical transport in soil: A review. *Vadose Zone Journal* **2002**, *1*, 222-238.
30. Ebrahimian, H.; Liaghat, A.; Parsinejad, M.; Playán, E.; Abbasi, F.; Navabian, M. Simulation of 1D surface and 2D subsurface water flow and nitrate transport in alternate and conventional furrow fertigation. *Irrigation science* **2013**, *31*, 301-316.
31. Mohammad, N.; Alazba, A.; Šimůnek, J. HYDRUS simulations of the effects of dual-drip subsurface irrigation and a physical barrier on water movement and solute transport in soils. *Irrigation science* **2014**, *32*, 111-125.
32. Yang, T.; Šimůnek, J.; Mo, M.; Mccullough-Sanden, B.; Shahrokhnia, H.; Cherchian, S.; Wu, L. Assessing salinity leaching efficiency in three soils by the HYDRUS-1D and-2D simulations. *Soil and Tillage Research* **2019**, *194*, 104342.
33. Kornelsen, K.C.; Coulibaly, P. Root-zone soil moisture estimation using data-driven methods. *Water Resources Research* **2014**, *50*, 2946-2962.
34. Zhang, H.; Yang, R.; Guo, S.; Li, Q. Modeling fertilization impacts on nitrate leaching and groundwater contamination with HYDRUS-1D and MT3DMS. *Paddy & Water Environment* **2020**, *18*.
35. Assefa, K.A.; Woodbury, A.D. Transient, spatially varied groundwater recharge modeling. *Water Resources Research* **2013**, *49*, 4593-4606.
36. Hilten, R.N.; Lawrence, T.M.; Tollner, E.W. Modeling stormwater runoff from green roofs with HYDRUS-1D. *Journal of hydrology* **2008**, *358*, 288-293.
37. Jandl, R.; Spögler, H.; Simunek, J.; Heng, L.K. Simulation of soil hydrology and establishment of a nitrogen budget of a mountain forest. *Environmental Science and Pollution Research* **2002**, *9*, 42-45.
38. Naghedifar, S.M.; Ziaei, A.N.; Ansari, H. Simulation of irrigation return flow from a Triticale farm under sprinkler and furrow irrigation systems using experimental data: A case study in arid region. *Agricultural water management* **2018**, *210*, 185-197.
39. Cobos, D.; Chambers, C. Calibrating ECH2O soil moisture sensors, application note. *Decagon Devices, Pullman* **2010**.
40. Richards, L.A. Capillary conduction of liquids through porous mediums. *Physics* **1931**, *1*, 318-333.
41. Celia, M.A.; Bouloutas, E.T.; Zarba, R.L. A general mass-conservative numerical solution for the unsaturated flow equation. *Water resources research* **1990**, *26*, 1483-1496.
42. Van Genuchten, M.T. A closed-form equation for predicting the hydraulic conductivity of unsaturated soils. *Soil science society of America journal* **1980**, *44*, 892-898.
43. Šimůnek, J.; Hopmans, J.W. Modeling compensated root water and nutrient uptake. *Ecological modelling* **2009**, *220*, 505-521.
44. Hoffman, G.J.; Van Genuchten, M.T. Soil properties and efficient water use: Water management for salinity control. *Limitations to efficient water use in crop production* **1983**, 73-85.
45. Feddes, R.A. *Simulation of field water use and crop yield*; Pudoc: 1982.
46. Allen, R.G.; Pereira, L.S.; Raes, D.; Smith, M. Crop evapotranspiration-Guidelines for computing crop water requirements-FAO Irrigation and drainage paper 56. *Fao, Rome* **1998**, *300*, D05109.
47. Green, W.H.; Ampt, G. Studies on Soil Phyics. *The Journal of Agricultural Science* **1911**, *4*, 1-24.
48. Laio, F.; Porporato, A.; Fernandez-Illescas, C.; Rodriguez-Iturbe, I. Plants in water-controlled ecosystems: active role in hydrologic processes and response to water stress: IV. Discussion of real cases. *Advances in Water Resources* **2001**, *24*, 745-762.
49. Leij, F.J.; Van Genuchten, M.T.; Yates, S.; Russell, W.; Kaveh, F. RETC: A computer program for analyzing soil water retention and hydraulic conductivity data. *Indirect methods for estimating the hydraulic properties of unsaturated soils. University of California, Riverside* **1992**, 263-272.

50. Schaap, M.G.; Leij, F.J.; Van Genuchten, M.T. Rosetta: A computer program for estimating soil hydraulic parameters with hierarchical pedotransfer functions. *Journal of hydrology* **2001**, *251*, 163-176.
51. Wesseling, J.; Elbers, J.; Kabat, P.; Van den Broek, B. SWATRE: Instructions for input. *Internal Note, Winand Staring Centre, Wageningen, the Netherlands* **1991**, *1991*.
52. Tolk, J.A.; Howell, T.A. Measured and simulated evapotranspiration of grain sorghum grown with full and limited irrigation in three high plains soils. *Transactions of the ASAE* **2001**, *44*, 1553.
53. Richards, F. A flexible growth curve for empirical use, J. Exp. *Botany* **1959**, *10*, 290-300.

Part 3. Estimation of soil moisture from UAS platforms

2.3.1. Introduction

Soil water content is one of the most essential environmental variables due to its key role in water and energy balances at the land-atmosphere interface [1]. Surface Soil Moisture (SSM) is highly varied in space and time and across different scales; therefore, detailed information on soil water content is of practical importance, especially over arid and semi-arid regions, which aims at improving water resources utilization efficiency, food productivity, irrigation planning and achieving sustainable water resources management [2-4].
Direct in situ observations of SSM are prolonged, labor-intensive, costly, and limited to discrete measurements in point scale, which precludes the spatial distribution of SSM due to its temporal and spatial variability [5]. An alternative to measure and monitor large-scale SSM is the application of Remotely-Sensed (RS) products [6]. Soil surface reflectance is the basis of SM monitoring through visible radiation methods, while Thermal Infrared Radiation (TIR) methods function on the sensitivity of Land Surface Temperature (LST) to SSM [7]. RS methods based on microwave radiation functions relied on the high level of difference between the soil and water dielectric constants [8].
SM estimations at coarse spatial resolution have been provided from several satellite missions including Soil Moisture and Ocean Salinity (SMOS) [9], Soil moisture Active and Passive (SMAP) [10], and Advanced Scatterometer (ASCAT) [11]. However, SM spatial-temporal variability [12] creates challenges in accurately estimating soil water content even through the current high-resolution satellite sensors and despite the recent advances in RS methods [13-14].
In the last decade, with the increasing developments in Unmanned Aerial Systems (UASs), they have been promoted as a suitable alternative for precise monitoring due to their high versatility, flexibility, and the ability to operate rapidly without necessarily planned scheduling. UASs represent major advantages against conventional platforms that have been broadly used over the years due to the ability to acquire near real-time ultra-high spatial and temporal resolution aerial maps with low operational costs [15-17].
Rapid signs of progress in the use of TIR techniques for soil moisture investigations have been made since 1974 [18]. The thermal RS methods estimate SM based on soil thermal properties or LST measurements at the TIR wavelengths (3 to 14 μm). Vegetation indices affected by climate conditions are included in the latter empirical methods [1]. However, the former approach relates SM to soil Thermal Inertia (TI), an intrinsic property that represents the ability of surface soil to resist temperature change. High TI values indicate small changes in temperature, while the reverse is true for low TI values [18]. Heat capacity and thermal conductivity as the two elements governing the TI, increase as SM increases; thus, SM can be inversely determined using TI if a relationship between these parameters is obtained in advance [19].
An algorithm was first developed by Price [20-21] to measure TI through satellite measurements of surface temperature by deriving an analytical expression that illustrates the satellite-based retrieved relation between bare soil temperature, mean evaporation and TI. Due to the requirements of a large number of observed ground data for model calibration in the TI-based empirical equations proposed by [22 and 19], these approaches are unavailable for many regions. Soil texture and porosity have been applied in models that relate TI to SM by [1, 23-24].
Only a few studies have monitored SM through RS in Iran despite the importance of water in this arid and semi-arid region [25-27]; on the other hand, the thermal inertia approach for SM estimation and UAS application have never been tested in this region. The present study gives a description on generating high-resolution SM products through applying a TI approach in this poorly monitored area by the application of drone-based thermal imagery.

2.3.2. Methodology

2.3.2.1. Thermal Inertia and Soil Moisture

The temperature of the soil's surface is influenced by many physical parameters, and the trends in temperature fluctuations of soil depend on its different thermal properties [28]. The method applied in this part of the study is to derive SM distribution based on TI, which describes the impedance of soil to temperature variations [29]. TI (J m^{-2} K^{-1} $s^{-1/2}$) is determined by volumetric heat capacity (c, J m^{-3} K^{-1}) and thermal conductivity (k, W m^{-1} K^{-1}) of the surface layer:

$$TI = \sqrt{c \times k} \quad (1)$$

Variations in temperature that occur during a diurnal solar cycle are caused by variations of TI. High TI indicates a high resistance to temperature change, resulting in a low difference in temperature (e.g., wet soils). The opposite happens to surfaces characterized by low TI (e.g., dry soils). Therefore, SM can be estimated from the differences in soil temperatures during the day [20]. TI cannot be derived directly due to dependency on factors that cannot be retrieved from remote observations (c and k can only be measured in situ); therefore, Price [21] simplified the estimation of TI through application of Apparent Thermal Inertia (ATI).

$$ATI = 1 - \alpha/\Delta T \quad (2)$$

where α is the surface albedo and ΔT (K) is the difference between the maximum and minimum soil surface temperatures during a diurnal solar cycle.
The procedure followed, as shown in Figure 1, included the derivation of ATI map using the FLIR Tau2 sensor (for diurnal ΔT estimation) and the grayscale reflection map from RGB sensor (for albedo estimation). In order obtain a good relationship between ATI and SM, the TI method must be applied over bare or scarcely vegetated soils [8]; therefore, the RGB orthomosaic was firstly applied to create a mask of bare soils and separate the vegetated pixels using the NGRDI index [30]. The common range for green vegetation is 0.1–0.8. The NGRDI threshold for separation of green vegetation from bare soils in the selected study area was 0.15. Once removing the vegetated pixels from the thermal map, it is necessary also to remove the shadow of vegetation. In this regard, while investigating the histogram of the ATI map masked by NGRDI index, a bi-modal distribution was observed. The first peak with lower temperature values characterizes the shadowed pixels and the second peak with higher temperatures corresponds to wet and dry soil pixels. The minimum between these two peaks was chosen as a threshold to remove the vegetated pixels. ATI is dependent on boundary conditions; therefore, a normalization analogous has to be performed [23]:

$$K_{ATI} = \frac{ATI - ATI_{dry}}{ATI_{sat} - ATI_{dry}} \quad (3)$$

where ATI_{dry} (K^{-1}) is ATI of dry soils, and ATI_{sat} (K^{-1}) represents the ATI of saturated soils, which are the minimum and maximum values of ATI spatial distributions during a time series, respectively. Considering the normalized value of ATI and soil porosity, the SM spatial distribution was derived from the equation below.

$$\theta = \Phi \left[1 - \frac{\ln K_{ATI}}{\varepsilon}\right]^{(1/-\mu)} \quad (4)$$

Where Φ is the soil porosity, ε and μ are two empirical parameters equal to 0.6 and 0.71 for fine-textured soils, respectively, whereas for coarse-textured soils these values are 2.95 and 0.16, respectively [23].

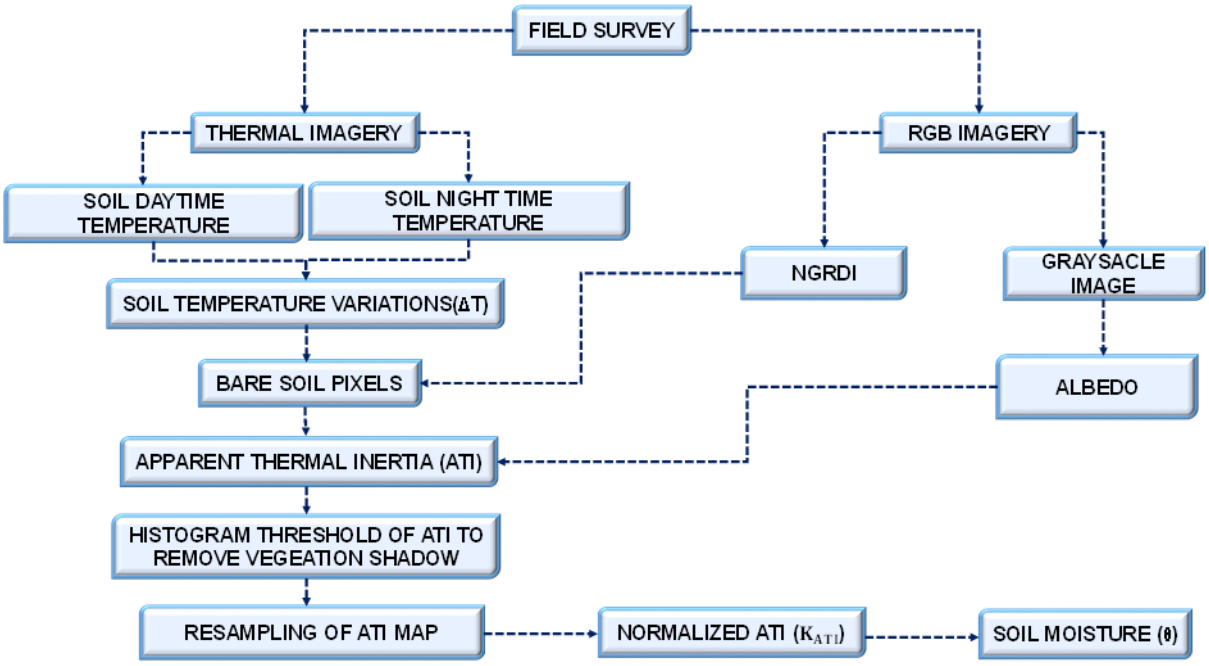

Figure 1. Flowchart of the applied methodology.

2.3.3. Study Area

The experimental site, selected for the execution of field and aerial surveys, was located 10 km from the Municipality of Neishabour, Iran (Figure 2), which comprises a total area of 2 ha. From the climatic point of view, the territory is part of the Eutemperate region with the biotope of the semi-desert. The annual average precipitation and potential evapotranspiration in this basin are 247.4 and 2335 mm, respectively. The highest and lowest monthly-averaged precipitations fall in March and August with values of 51 and 0.16 mm, respectively. The land use is characterized by bare soils and heterogeneous low vegetated agricultural fields. The main type of crop occurring at the aerial imagery acquisition day was wheat; although, some parts of the area were irrigated for saffron cultivation.

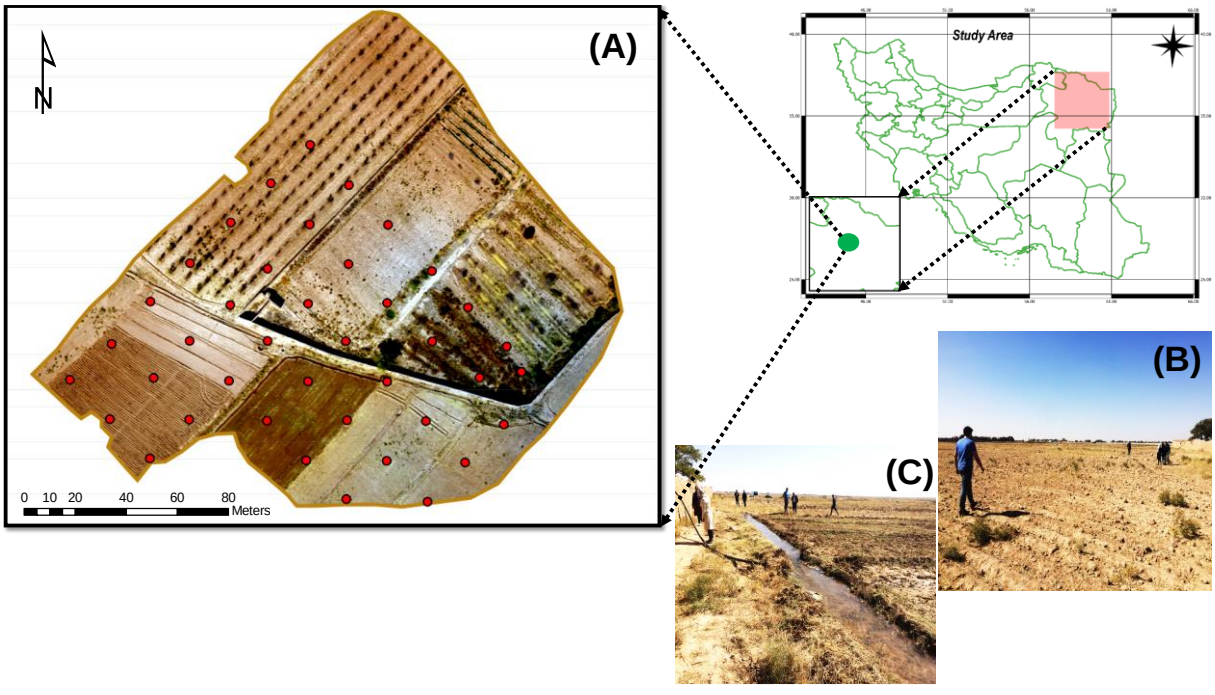

Figure 2. Location of the study area (**A**) Triband orthomosaic over study site overlapped with observed SM data (red symbols), (**B**) and (**C**) Field survey performed on 17 October 2018.

2.3.3.1. Thermal data

On 17 October 2018, two flight campaigns were carried out over the study area with a FLIR Tau2 336 thermal sensor (FLIR Systems, Inc. Wilsonville, Oregon, United States) installed onboard a quadcopter DJI Phantom 3 Pro (SZ DJI Technology Co., Ltd. Shenzhen, Guangdong, China), which was equipped with an RGB color filter array camera of FC 300X.
The first aerial survey was carried out around 11:30 in the morning UTC in order to evaluate the daily increase in surface soil temperature, while the second one was conducted on the same day at 20:00 UTC to estimate the soil temperature in the absence of solar load. Both surveys were performed in clear sky conditions. Flight height was set according to a ground sampling distance (GSD) of 19cm and 4.6cm for thermal and RGB images, respectively, and the flight plan applied a cross pattern with 90% side lap and 90% forward overlap. The radiometric solution produces thermographic IR video files in ".TMC" format, which were visualized, processed, and radiometrically corrected with ThermoViewer Software to extract 426 and 476 thermal images during day and nighttime, respectively. The procedure of georeferencing the thermal images was conducted in Geosetter Software in order to assign geographical data to each image metadata, and the final thermal orthomosaics were obtained in Pix4D Mapper Software. Afterward, Ground Control Points (GCPs) obtained on the field were assigned to the thermal and RGB orthomosaics to ensure a proper overlap. A total of 184 RGB images were acquired to build the triband orthomosaic (Figure 2), which was further applied to extract the Normalized Green Red Difference Index (NGRDI).

2.3.3.2. In-situ data

Simultaneously with the acquisition of the thermal images, a ground campaign was carried out to collect soil samples at forty locations. The sampling was carried out on bare soil, which were further analyzed using the method of hydrometer in the laboratory to obtain the amount of each particle fraction from the United States Department of Agriculture (USDA) soil texture triangle. In particular, SM in 40 points was measured at a depth of 10-15 cm from a FieldScout TDR300 Soil Moisture Meter (by Spectrum Technologies, Inc.), which was applied to measure soil volumetric water content and were further analyzed in the validation procedures of the SM map. This portable device consists of a probe with 0.15 m long steel rods and is characterized by a soil moisture resolution of 0.1%. Table 1 shows the characteristics of the observed SM data.

Table 1. Soil moisture of soil samples collected on 17 October 2018.

Soil Sample	Latitude (°N)	Longitude (°E)	Soil Moisture (%)	Soil Sample	Latitude (°N)	Longitude (°E)	Soil Moisture (%)
1	36° 8'9.76"	58°51'39.10"	10.4	**21**	36° 8'11.23"	58°51'35.19"	8.4
2	36° 8' 10.23"	58°51'38.55"	4.4	**22**	36° 8'11.68"	58°51'35.78"	8.3
3	36° 8'10.70"	58°51'38.00"	3.1	**23**	36° 8'10.81"	58°51'33.48"	5.8
4	36° 8'11.18"	58°51'37.45"	4.6	**24**	36° 8'10.37"	58°51'32.89"	5.7
5	36° 8'11.65"	58°51'36.90"	5.5	**25**	36° 8'9.93"	58°51'32.31"	5.6
6	36° 8'11.20"	58°51'36.32"	5.6	**26**	36° 8'9.3"	58°51'32.86"	6
7	36° 8'10.74"	58°51'36.87"	6.5	**27**	36° 8'9.8"	58°51'33.44"	5.4
8	36° 8'10.26"	58°51'37.42"	8.3	**28**	36° 8'10.35"	58°51'34.03"	6.6
9	36° 8'9.79"	58°51'37.97"	6.8	**29**	36° 8'10.32"	58°51'35.16"	8
10	36° 8'9.32"	58°51'38.52"	11.6	**30**	36° 8'9.87"	58°51'34.58"	8.3
11	36° 8'9.35"	58°51'37.39"	13.6	**31**	36° 8'9.42"	58°51'33.99"	5.5
12	36° 8'9.82"	58°51'36.84"	22.2	**32**	36° 8'8.98"	58°51'33.41"	6.1
13	36° 8'10.29"	58°51'36.29"	5.2	**33**	36° 8'8.95"	58°51'34.54"	50.3
14	36° 8'10.76"	58°51'35.74"	5.2	**34**	36° 8'9.39"	58°51'35.12"	51.4
15	36° 8'12.12"	58°51'36.35"	5.8	**35**	36° 8'8.92"	58°51'35.67"	55.2
16	36° 8'12.60"	58°51'35.81"	7.2	**36**	36° 8'8.49"	58°51'35.10"	57.1
17	36° 8'12.16"	58°51'35.23"	7.1	**37**	36° 8'8.45"	58°51'36.22"	11.3
18	36° 8'11.71"	58°51'34.64"	8.1	**38**	36° 8'8.43"	58°51'37.36"	9.6
19	36° 8'11.27"	58°51'34.07"	7.6	**39**	36° 8'8.90"	58°51'36.81"	12.3
20	36° 8'10.79"	58°51'34.61"	7.8	**40**	36° 8'8.87"	58°51'37.94"	12.1

2.3.4. RESULTS AND DISCUSSION

In this part of the study, the spatial distribution of SM was derived through a remotely sensed ATI map. In the following sections, we present the temperature, ATI, and SM maps.

2.3.4.1. Temperature and ATI Maps

Two temperature maps were obtained from the FLIR Tau2 sensor after the stitching and radiometrically correction of the imageries. The retrieved temperature maps are shown in Figure 3. In particular, Figure 3A shows the temperature map of the morning flight, ranging from 287 to 332 K; while, the temperature map of the nighttime flight, which varies between 273 and 286 K is shown in Figure 3B. Cai et al.[32] illustrated that a temperature variation of the order of 10 K is sufficient for an accurate estimation of SM, which is in concordance with the obtained temperature range.

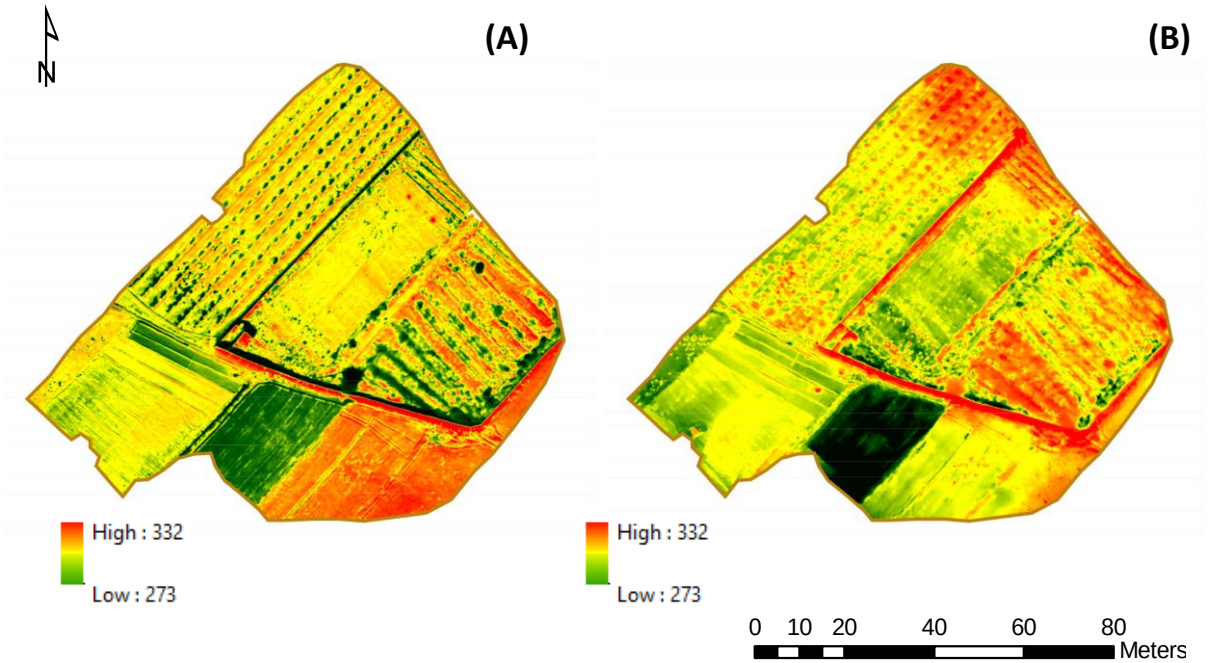

Figure 3. Soil surface temperatures obtained from the thermal camera (**A**) during maximum solar load; (**B**) at night.

The ATI map obtained from the temperature variations of the study field after separating the vegetation and its shadow is illustrated in Figure 4A. After this step, a resampling method was applied over the ATI map to perform an averaging of 1 m over the pixels due to the ultra-high resolution of pixels.

2.3.4.2. Soil Moisture Map

The laboratory analyses' results of the collected soil samples in the study area highlighted that all of our samples are almost homogeneous in terms of texture and recommended clay loam as the main soil texture in different parts of the field; thus, the parameters of Φ, ε, and μ were considered equal to 0.50, 0.6 and 0.71, respectively [23]. SM spatial distribution corresponding to the 40 sample points was obtained by using Eq. (4). Calculated SM values were compared with the measured ones (Figure 5A). The R^2=0.81 and RMSE= 0.03 were obtained, which are in full agreement with [31].

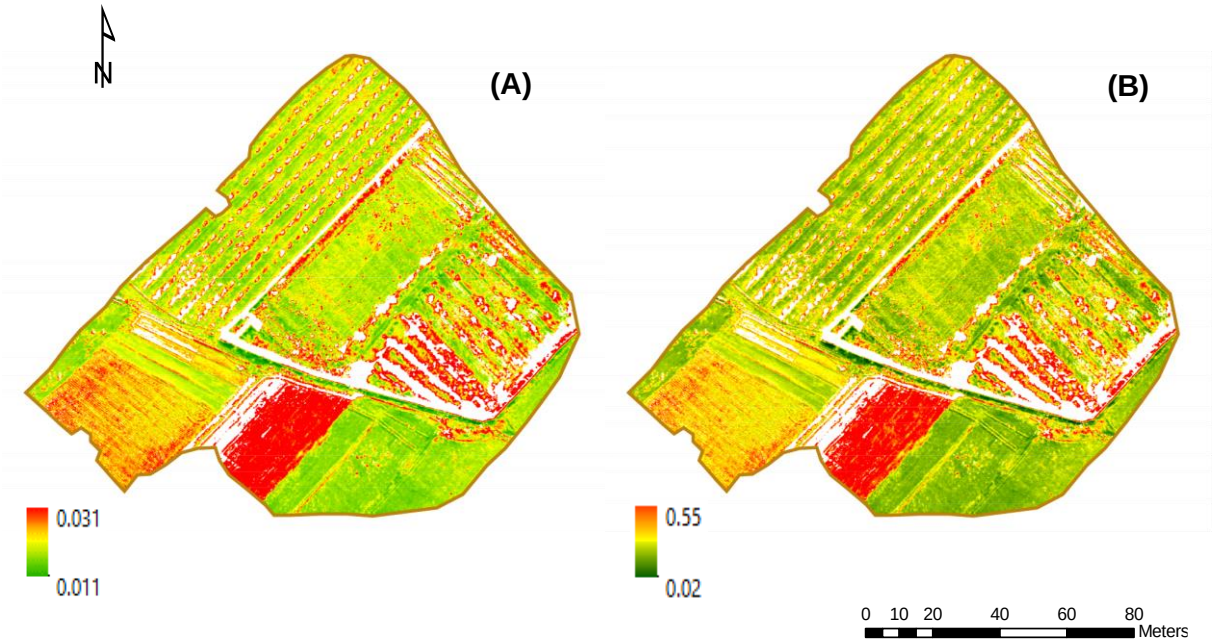

Figure 4. (**A**) ATI map of the bare soils of the study area. The ATI values in the map are expressed in k^{-1} units; (**B**) Map of SM derived from FLIR thermal camera onboard the UAS expressed in m^3/m^3.

Other studies have also demonstrated a good relationship between ATI over bare soils and SM values, as verified in our research [22-23]. Visual examination of SM (Figure 4B) indicates spatial trends of soil water content for bare and low vegetated soils in the study area, including observation of the lowest SM values identified in the northwest side of the acquired imagery; while, high SM values were recognized along the central section of the study area that is characterized by the irrigation performed for saffron cultivation.

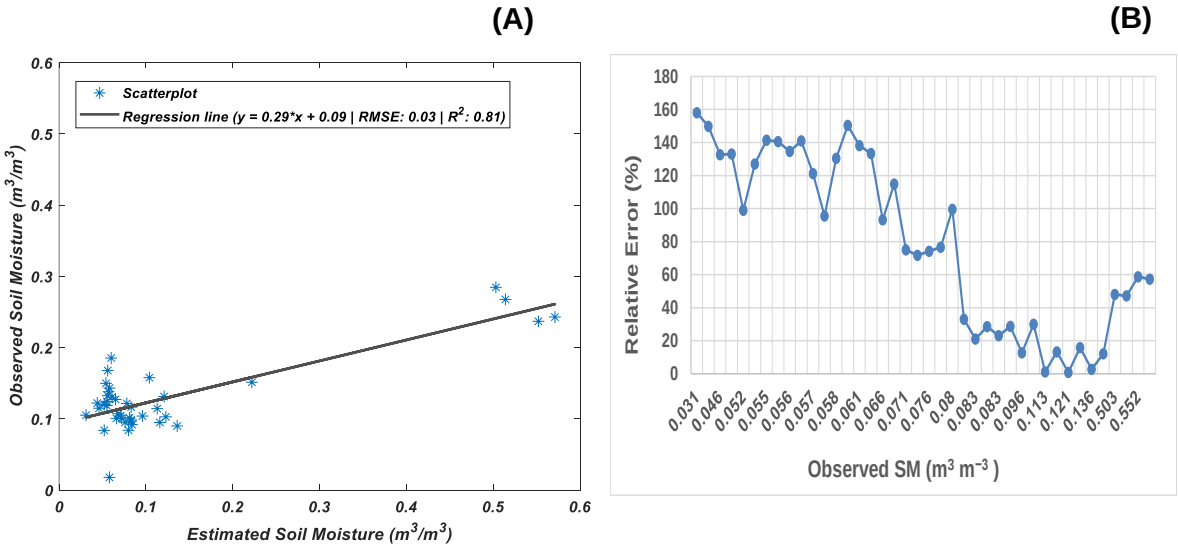

Figure 5. (**A**) Scatterplot of Estimated vs. Observed SM; (B) Relative errors observed in each sample point vs. the observed SM values.

As shown in Fig 5B, the TI method applied on the thermal imagery obtained from the UAS estimated SM accurately in the medium range of its values from 8% up to 30% and showed the minimum relative error $(100 \times |measured\ SM - observed\ SM|)/observed\ SM)$ values up to 30%. However, in the southwestern part of the field covered with the driest soils with less than 8% of water content, and in the middle-irrigated zone that water content was recorded by TDR up to 50%, this method was not able to estimate the SM values very precisely, and the errors obtained from the model results show higher error values. Based on similar results obtained by [23], it can be concluded that the applied method overestimated the values corresponding to soil water contents <0.05 $m^3\ m^{-3}$. The errors observed in value ranges higher than 30% could be due to a

different porosity value over this zone, which will affect the SM results greatly since one porosity value for all parts of the field was applied. Another possible source of underestimations in this zone lies in the albedo calculations. Due to lack of multispectral sensor onboard the UAS, the albedo map was obtained from the grayscale reflection imagery and by comparing the maximum reflection amount from a total white pixel with the value of 255 with all the desired pixels throughout the field and by considering the known albedo value of the white surface. The albedo values over the irrigated area are lower than the dry soil due to lower reflections from the wet surface. Since the albedo calculation procedure was not from a multispectral camera, the albedo values over the irrigated area and the driest part of the field were overestimated, which affected the final SM results. Moreover, it should be considered that in the process of extracting vegetation from bare soil pixels, there were some vegetated pixels that were not precisely extracted due to the fact that separating 100% pixels of vegetation is nearly impossible since the resolution of thermal and RGB sensors are different. More importantly, we applied an RGB index instead of the most commonly used NDVI to separate vegetation from soil, which distinguishes vegetation from soil so much better. Therefore, by applying an RGB index, separating the exact pixels of vegetation from soil cannot be done due to the almost similar reflection from red, greed, and blue bands rather than NIR, which is applied in NDVI. Consequently, applying a multispectral sensor and calculating NDVI is suggested in future studies.

2.3.5. Conclusions

In this part of the study, a TI approach was applied to retrieve SM for bare and scarcely vegetated soils by integrating high spatial resolution thermal imagery onboard a UAS regarding the fact that diurnal thermal behavior of soil surface temperature is affected by fluctuations in SSM. For this purpose, ground soil sampling was carried out in the study area in order to determine the top soil moisture content and the composition of the soil samples. These data were used to validate the SM obtained on the basis of two different airborne thermal surveys. The results obtained with an R^2=0.81 show a satisfactory relation between in situ observations and the estimated SM values obtained from integration of soil texture properties and surface temperature with an accuracy that can be considered satisfactory for practical purposes. The potential of UASs in acquiring high-resolution thermal data was evaluated in this part of the study, suggesting that these instruments represent a fast, reliable, and cost-effective resource in measuring crop biophysical variables in precision farming applications as well as soil water content as an aid for sustainable water management in the agricultural domain over arid and semi-arid regions. The authors are currently working with a larger dataset, including a wider range of soil moisture conditions, to generalize this methodology.

2.3.6. References

1. Lu, Y., Horton, R., Zhang, X., and Ren, T. (2018). Accounting for soil porosity improves a thermal inertia model for estimating surface soil water content. Remote Sens. Environ. *212*, 79–89 https://doi.org/10.1016/j.rse.2018.04.045.
2. Engman, E.T. (1991). Applications of microwave remote sensing of soil moisture for water resources and agriculture. Remote Sens. Environ. *35*, 213–226 https://doi.org/10.1016/0034-4257(91)90013-v.
3. Bolten, J.D., Crow, W.T., Zhan, X., Jackson, T.J., and Reynolds, C.A. (2010). Evaluating the Utility of Remotely Sensed Soil Moisture Retrievals for Operational Agricultural Drought Monitoring. IEEE J-STARS *3*, 57–66 https://doi.org/10.1109/jstars.2009.2037163.
4. Robinson, D., Campbell, C., Hopmans, J., Hornbuckle, B., Jones, S., Knight, R., Ogden, F., Selker, J., and Wendroth, O. (2008). Soil Moisture Measurement for Ecological And Hydrological Watershed-Scale Observatories: A Review. Vadose Zone J. 7, 358–389 https://doi.org/10.2136/vzj2007.0143.
5. Crow, W., Berg, A., Cosh, M.H., Loew, A., Mohanty, B.P., Panciera, R., Rosnay, P. de, Ryu, D., and Walker, J. (2012). Upscaling sparse ground-based soil moisture observations for the validation of coarse-resolution satellite soil moisture products. Rev. Geophys. *50*, 1–20 https://doi.org/10.1029/2011rg000372.
6. Wang, L., and Qu, J.J. (2009). Satellite remote sensing applications for surface soil moisture monitoring: A review. Front. Earth Sci. China *3*, 237–247 https://doi.org/10.1007/s11707-009-0023-7.
7. Petropoulos, G.P., Ireland, G., and Barrett, B. (2015). Surface soil moisture retrievals from remote sensing: Current status, products & future trends. Physics and Chemistry of the Earth, Parts A/B/C *83–84*, 36–56 https://doi.org/10.1016/j.pce.2015.02.009.
8. Jackson, T.J. (1993). III. Measuring surface soil moisture using passive microwave remote sensing. Hydrol. Process. *7*, 139–152 https://doi.org/10.1002/hyp.3360070205.
9. Kerr, Y.H., Waldteufel, P., Wigneron, J.-, Martinuzzi, J., Font, J., and Berger, M. (2001). Soil moisture retrieval from space: the Soil Moisture and Ocean Salinity (SMOS) mission. IEEE Trans. Geosci. Remote Sens. *39*, 1729–1735 https://doi.org/10.1109/36.942551.

10. Entekhabi, D., Njoku, E.G., O'Neill, P.E., Kellogg, K.H., Crow, W.T., Edelstein, W.N., Entin, J.K., Goodman, S.D., Jackson, T.J., Johnson, J., et al. (2010). The Soil Moisture Active Passive (SMAP) Mission. Proc. IEEE *98*, 704–716 https://doi.org/10.1109/jproc.2010.2043918.
11. Wagner, W., Hahn, S., Kidd, R., Melzer, T., Bartalis, Z., Hasenauer, S., Figa-Saldaña, J., de Rosnay, P., Jann, A., Schneider, S., et al. (2013). The ASCAT Soil Moisture Product: A Review of its Specifications, Validation Results, and Emerging Applications. Meteorol. Z. *22*, 5–33 https://doi.org/10.1127/0941-2948/2013/0399.
12. Brocca, L., Melone, F., Moramarco, T., and Morbidelli, R. (2010). Spatial-temporal variability of soil moisture and its estimation across scales. Water Resour. Res. *46* https://doi.org/10.1029/2009wr008016.
13. El Hajj, M., Baghdadi, N., Zribi, M., and Bazzi, H. (2017). Synergic Use of Sentinel-1 and Sentinel-2 Images for Operational Soil Moisture Mapping at High Spatial Resolution over Agricultural Areas. Remote Sens. *9*, 1292 https://doi.org/10.3390/rs9121292.
14. Kim, H., and Lakshmi, V. (2018). Use of Cyclone Global Navigation Satellite System (CyGNSS) Observations for Estimation of Soil Moisture. Geophys. Res. Lett. *45*, 8272–8282 https://doi.org/10.1029/2018gl078923.
15. Pajares, G. (2015). Overview and Current Status of Remote Sensing Applications Based on Unmanned Aerial Vehicles (UAVs). PHOTOGRAMM. ENG. REM. S *81*, 281–330 https://doi.org/10.14358/pers.81.4.281.
16. Manfreda, S., M. F. McCabe, P. E. Miller, R. Lucas, V. Pajuelo Madrigal, G. Mallinis, E. Ben-Dor, D. Helman, L. Estes, G. Ciraolo, J. Müllerová, F. Tauro, M. I. de Lima, J. L. M. P. de Lima, A. Maltese, F. Frances, K. Caylor, M. Kohv, M. Perks, G. Ruiz-Pérez, Z. Su, G. Vico, and B. Toth, On the Use of Unmanned Aerial Systems for Environmental Monitoring, Remote Sensing, 10(4), 641; (doi:10.3390/rs10040641) 2018.
17. Tmušić, G., S. Manfreda, H. Aasen, M. James, G. Gonçalves E. Ben-Dor, A. Brook, M Polinova, J.J. Arranz, J. Mészáros, R. Zhuang, K. Johansen, Y. Malbeteau, I.P. de Lima, C. Davids, S. Herban, M. McCabe, Practical guidance for UAS-based environmental mapping, Remote Sensing, 12, 1001, (doi: 10.3390/rs12061001) 2020.
18. Pratt, D.A., and Ellyett, C.D. (1979). The thermal inertia approach to mapping of soil moisture and geology. Remote Sens. Environ. *8*, 151–168 https://doi.org/10.1016/0034-4257(79)90014-2.
19. Matsushima, D., Kimura, R., and Shinoda, M. (2011). Soil Moisture Estimation Using Thermal Inertia: Potential and Sensitivity to Data Conditions. J. Hydrometeorol. *13*, 638–648 https://doi.org/10.1175/jhm-d-10-05024.1.
20. Price, J.C. (1980). The potential of remotely sensed thermal infrared data to infer surface soil moisture and evaporation. Water Resour. Res. *16*, 787–795 https://doi.org/10.1029/wr016i004p00787.
21. Price, J.C. (1985). On the analysis of thermal infrared imagery: The limited utility of apparent thermal inertia. Remote Sens. Environ. *18*, 59–73 https://doi.org/10.1016/0034-4257(85)90038-0.
22. Verstraeten, W.W., Veroustraete, F., van der Sande, C.J., Grootaers, I., and Feyen, J. (2006). Soil moisture retrieval using thermal inertia, determined with visible and thermal spaceborne data, validated for European forests. Remote Sens. Environ. *101*, 299–314 https://doi.org/10.1016/j.rse.2005.12.016.
23. Minacapilli, M., Cammalleri, C., Ciraolo, G., D'Asaro, F., Iovino, M., and Maltese, A. (2012). Thermal Inertia Modeling for Soil Surface Water Content Estimation: A Laboratory Experiment. SOIL. SCI. SOC. AM. J. *76*, 92–100 https://doi.org/10.2136/sssaj2011.0122.
24. Paruta, A., Nasta, P., Ciraolo, G., Capodici, F., Manfreda, S., Romano, N., Bendor, E., Zeng, Y., Maltese, A., Dal Sasso, S. F. and Zhuang, R. (2020). A geostatistical approach to map near-surface soil moisture through hyper-spatial resolution thermal inertia, IEEE Transactions on Geoscience and Remote Sensing, (doi: 10.1109/TGRS.2020.3019200).
25. Rahmani, A., Golian, S., and Brocca, L. (2016). Multiyear monitoring of soil moisture over Iran through satellite and reanalysis soil moisture products. Int. J. Appl. Earth. Obs. Geoinf. *48*, 85–95 https://doi.org/10.1016/j.jag.2015.06.009.
26. Fakharizadehshirazi, E., Sabziparvar, A.A., and Sodoudi, S. (2019). Long-term spatiotemporal variations in satellite-based soil moisture and vegetation indices over Iran. Environ. Earth Sci. *78* https://doi.org/10.1007/s12665-019-8347-4.
27. Gheybi, F., Paridad, P., Faridani, F., Farid, A., Pizarro, A., Fiorentino, M., and Manfreda, S. (2019). Soil Moisture Monitoring in Iran by Implementing Satellite Data into the Root-Zone SMAR Model. Hydrology *6*, 44 https://doi.org/10.3390/hydrology6020044.
28. Cheruy, F., Dufresne, J.L., Mesbah, S.A., Grandpeix, J.Y., and Wang, F. (2017). Role of Soil Thermal Inertia in Surface Temperature and Soil Moisture-Temperature Feedback. J. ADV. MODEL. EARTH. SY. *9*, 2906–2919 https://doi.org/10.1002/2017ms001036.
29. Kahle, A.B., Gillespie, A.R., and Goetz, A.F.H. (1976). Thermal inertia imaging: A new geologic mapping tool. Geophys. Res. Lett. *3*, 26–28 https://doi.org/10.1029/gl003i001p00026.
30. Yang, D. (2018). Gobi Vegetation Recognition Based on Low-Altitude Photogrammetry Images of UAV. IOP Conf. Ser.: Earth Environ. Sci. *186*, 012053 https://doi.org/10.1088/1755-1315/186/5/012053
31. Palombo, A., Pascucci, S., Loperte, A., Lettino, A., Castaldi, F., Muolo, M.R., and Santini, F. (2019). Soil Moisture Retrieval by Integrating TASI-600 Airborne Thermal Data, WorldView 2 Satellite Data and Field Measurements: Petacciato Case Study. Sensors (Basel) *19*, 1515 https://doi.org/10.3390/s19071515.
32. Cai, G., Xue, Y., Hu, Y., Wang, Y., Guo, J., Luo, Y., Wu, C., Zhong, S., and Qi, S. (2007). Soil moisture retrieval from MODIS data in Northern China Plain using thermal inertia model. Int. J. Remote Sens. *28*, 3567–3581 https://doi.org/10.1080/01431160601034886.

Chapter (3): Vegetation monitoring

3.1. Introduction

The well-known RS vegetation indicators range from spectral indices, such as the Normalized Difference Vegetation Index (NDVI); to biophysical variable estimates such as the Leaf Area Index (LAI), Fraction of Absorbed Photosynthetically Active Radiation (FAPAR) (absorbed by the photosynthesizing tissue in a canopy) and Fraction of green vegetation Cover (FCover) [1].
Many studies [3-5] suggested that Evapotranspiration (ET), in combination with other vegetation indices, is an important variable to monitor and estimate crop yield and biomass. ET is the process of transferring water vapor from the surface to the atmosphere through evaporation and plant transpiration from wet surfaces. ET plays an important role in the earth-atmosphere interactions, since it connects the energy, water and carbon cycles [4]. The potential and reference ET are influenced through prevailing weather conditions such as radiation, temperature, wind, and relative humidity [3]. The status of actual evapotranspiration (ETa), in comparison with the long historical records (e.g., the ETa anomaly for a given period), has the potential to identify vegetation stress in time and space [6], therefore, ETa is an essential element in the design, development, and monitoring of agricultural and environmental systems [4].
By advancing the remote sensing technologies, ET has been consistently estimated at multiple spatiotemporal scales using models that can be grouped into: (I) vegetation index (VI)-based models which rely on vegetation indices (e.g. leaf area index (LAI) or the Normalized Difference Vegetation Index (NDVI)) as well as meteorological inputs (mainly net radiation (Rn), air temperature (Tair) and vapor pressure deficit (VPD)) following the Penman-Monteith logic; and (II) land surface temperature (LST)-based models which rely on LST as an effective proxy for soil moisture following the surface energy balance (SEB) [7]. Some of the well-known VI-based models are the Priestley-Taylor Jet Propulsion Laboratory (PT-JPL) [8](Fisher et al., 2008), the Moderate Resolution Imaging Spectroradiometer (MODIS) Land Surface Evapotranspiration (MOD16) [9], and the Global Land-Surface Evaporation Amsterdam Methodology (GLEAM) [10]; whereas LST-based models are the Surface Energy Balance Algorithm for Land model (SEBAL) [11], Mapping Evapotranspiration at High Resolution with Internalized Calibration (METRIC) [12], and Surface Energy Balance System (SEBS) [13].
Another important means of quantifying drought in a spatially comparable way across different regions is the Palmer Drought Severity Index (PDSI) originally developed by [14]. Different studies showed that PDSI is very effective in determining long-term drought, considering the basic effect of global warming through potential evapotranspiration, and taking precedent (prior month) conditions into account [15-18]. For the calculation of the PDSI four inputs are needed: precipitation, temperature, latitude, and the soil available water capacity (AWC) of the study area, which is a constant also known as the field capacity [19]. The four inputs are used to compute a water balance for the study area, which then serves as the basis for the calculation of the PDSI. For a detailed explanation of the calculation of the PDSI [20].
The main goal of this part of the study was to evaluate the potential of Fisher-Shannon statistical method to explore any anomalies happening for the vegetation cover around big urban areas using soil-water-atmosphere-plant related satellite products available in the Google Earth Engine cloud database (i.e., LAI, NDVI, EVI, and ET from MODIS). Peri-urban parks were selected for our investigations as particularly significant areas because they play a key role not only in improving environmental quality and life but also in facing climatic change and mitigating climate change effects.

3.2. Methodology

3.2.1. The Singular Spectrum Analysis

There are several techniques for decomposing a time series into a certain number of independent components; among these the Singular Spectrum Analysis (SSA) [21] represent an efficient and well known decompositional method that is based on phase-lagged copies of the series. The independent components obtained by applying the SSA can be easily recognizable as slowly changing trend, oscillatory components and structureless noise [22].
Let's consider a time series y_i (i =1, .., N) and a lag M, then the Toeplitz lagged correlation matrix can be constructed:

$$c_j = \frac{1}{N-j}\sum_{i=1}^{N-j} y_i y_{i+j}, \; 0 \leq j \leq M \quad (1)$$

Sorting its eigenvalues λ_k in decreasing order, the corresponding eigenvectors $E_{k,j}$ where j and k vary from 1 to M, are used to calculate the k-th principal component i

$$a_{ik} = \sum_{j=1}^{M} y_{i+j} E_{jk}, \; 0 \leq i \leq N\text{-}M, \quad (2)$$

and the k-th reconstructed component of the time series:

$$R_k = \frac{1}{M}\sum_{j=1}^{M} a_{i-j,k} E_{jk}, \; M \leq i \leq N\text{-}M+1. \quad (3)$$

Since the eigenvalue λ_k represents the fraction of the total variance of the original series explained in k-th reconstructed component R_k, the decreasing order of the eigenvalues also reflects the decreasing order of the reconstructed components by the fraction of the total variance of the series [23]. SSA requires that the lag M is properly selected. Khan and Poskitt [24] calculated the maximum $M = (log\ N)^c$, $1.5 \leq c \leq 2.5$.

The minimum description length (MDL) criterion [25]

$$MDL(k) = -\log\left(\frac{\prod_{i=k+1}^{p} \lambda_i^{\frac{1}{p-k}}}{\frac{1}{p-k}\sum_{i=k+1}^{p}\lambda_i} \right)^{(p-k)N} + \frac{1}{2}k(2p-k)\log N \quad (4)$$

is used to separate the series into two parts that we can define as trend and detrended series; λ_k are the eigenvalues, p is the number of eigenvalues, identical to M, and N is the length of the original series. The separation occurs at the value of $k \in \{0, 1, 2, \ldots, p\text{-}1\}$ for which the MDL is minimized.

3.2.2. The Fisher-Shannon method

By the Fisher-Shannon the informational properties of a time series can be investigated, namely the Fisher Information Measure (FIM) and the Shannon entropy (SE), which in theory of information are used to quantify respectively the local and global smoothness of the distribution of a series. The FIM and SE can be employed to characterize the complexity of non-stationary time series described in terms of order and organization [26]. The FIM measures the order and organization of the series, and the SE its uncertainty or disorder [27]. The FIM and SE are defined by the following formulae:

$$\mathrm{FIM} = \int_{-\infty}^{+\infty} \left(\frac{\partial}{\partial x} f(x) \right)^2 \frac{dx}{f(x)}, \quad (5)$$

$$\mathrm{SE} = -\int_{-\infty}^{+\infty} f_X(x) \log f_X(x) dx, \quad (6)$$

where $f(x)$ is the distribution of the series x. Instead of SE, it is generally used the Shannon entropy power N_X

$$N_x = \frac{1}{2\pi e} e^{2SE}, \quad (7)$$

to avoid to deal with negative quantities. FIM and N_X are not independent of each other due to the isoperimetric inequality $\mathrm{FIM} \cdot N_X \geq D$ [28], where D is the dimension of the space, which for time series is 1.

FIM and N_X depend on $f(x)$, whose accurate estimation is crucial to obtain reliable values of informational quantities. For calculating FIM and N_X we applied the kernel-based approach that Telesca and Lovallo [29] demonstrated to be better than the discrete-based approach. Thus applying the kernel density estimator method for $f(x)$ [30, 31] as shown in the following formula:

$$\hat{f}_M(x) = \frac{1}{Mb}\sum_{i=1}^{M} K\left(\frac{x - x_i}{b} \right), \quad (8)$$

where M and b denote the length of the series and the bandwidth respectively, while $K(u)$ is the kernel that is a continuous, symmetric and non-negative function satisfying the two following constrains:

$K(u) \geq 0$ and $\int_{-\infty}^{+\infty} K(u)du = 1$, (9)

$f(x)$ is estimated by means of an optimized integrated procedure using the algorithms of Troudi et al. [32] and Raykar and Duraiswami [33], with a Gaussian kernel:

$$\hat{f}_M(x) = \frac{1}{M\sqrt{2\pi b^2}} \sum_{i=1}^{M} e^{-\frac{(x-x_i)^2}{2b^2}} \quad (10)$$

,

Due to the isoperimetric inequality, the Fisher-Shannon information plane (FSIP), which has the N_X as x-axis and FIM as y-axis, represents a very useful tool to investigate the time dynamics of signals [34]. For scalar signals, the curve FIM·N_X=1 separates the FSIP into two parts, and each signal can be represented by a point located only in the space FIM·N_X>1.

3.3. Study Areas

For the purpose of this part of the study, the following three study areas were selected in the center and south of Italy: Appia park and Castel Porziano in the center, and Castel Volturno in the south (Fig. 1). These areas were selected because they were representative of diverse vegetation covers, as detailed in the following sections 3.3.1. and 3.3.2.

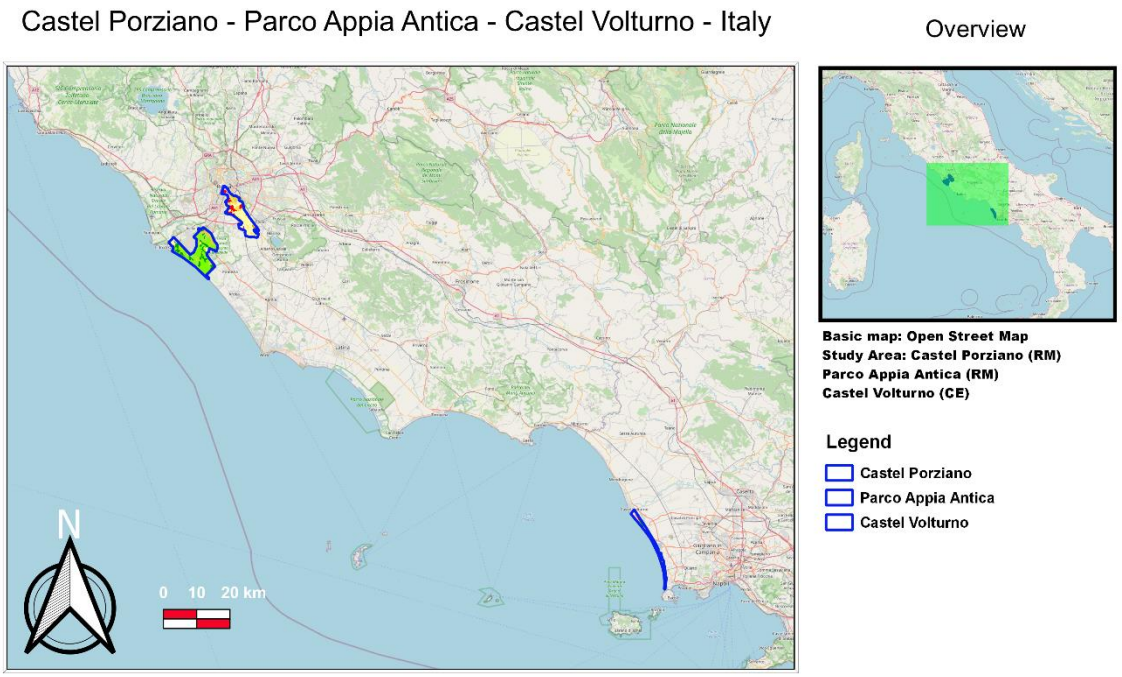

Figure 1. Location of the investigated areas.

The characteristics of the study areas (including Longitude, Latitude, Area, Annual precipitation, Annual mean temperature, Vegetation description, and Climate system) are presented in Table 1.

3.3.1. Castel Volturno

Castel Volturno is a natural reserve which occupies a total area of 268 hectares that extends along the sandy coast of the municipality of Castel Volturno (CE), in a strip between the mouth of the Regi Lagni to the north and the mouth of Lago Patria to the south. The site includes the protected area named ZSC IT8010021 “Pineta di Patria” and Regional Nature Reserve “Foce Volturno-Costa di Licola” made up of pines.

Table 1. Meteo-climatic and vegetational characteristics of the investigated sites

Study area	Castel Volturno	Castel Porziano	Appia park
Longitude	14°1'45"E	12°23'36"E	12°31'55"E
Latitude	40°56'1"N	41°42'35"N	41°49'40"N
Area [km^2]	19	85	96
Annual precipitation [mm]	1078	878	878
Annual mean temp. [C^o]	15.5	15.8	15.8
Climate system by the Köppen-Geiger	Hot-summer Mediterranean climate, Csa	Csa	Csa
Vegetation description	268 hectares The site is mainly characterized by the presence of woods holm oak, pine forests with Pinus pinea and a nucleus of retro-dunal hygrophilous vegetation.	2300 hectares The site is mainly characterized by the presence of holm oak (261 hectares), cork oak wood (460 hectares), and stone pine forest (750 hectares) The woods alternate with clearings and natural grasslands	4580 hectares : It is a mosaic of different environments: large spaces intended for cultivation and extensive grazing are interrupted by uncultivated areas, residual wooded strips, where agricultural exploitation has not arrived or has long since ceased, ditches with the presence of riparian vegetation and some wet areas

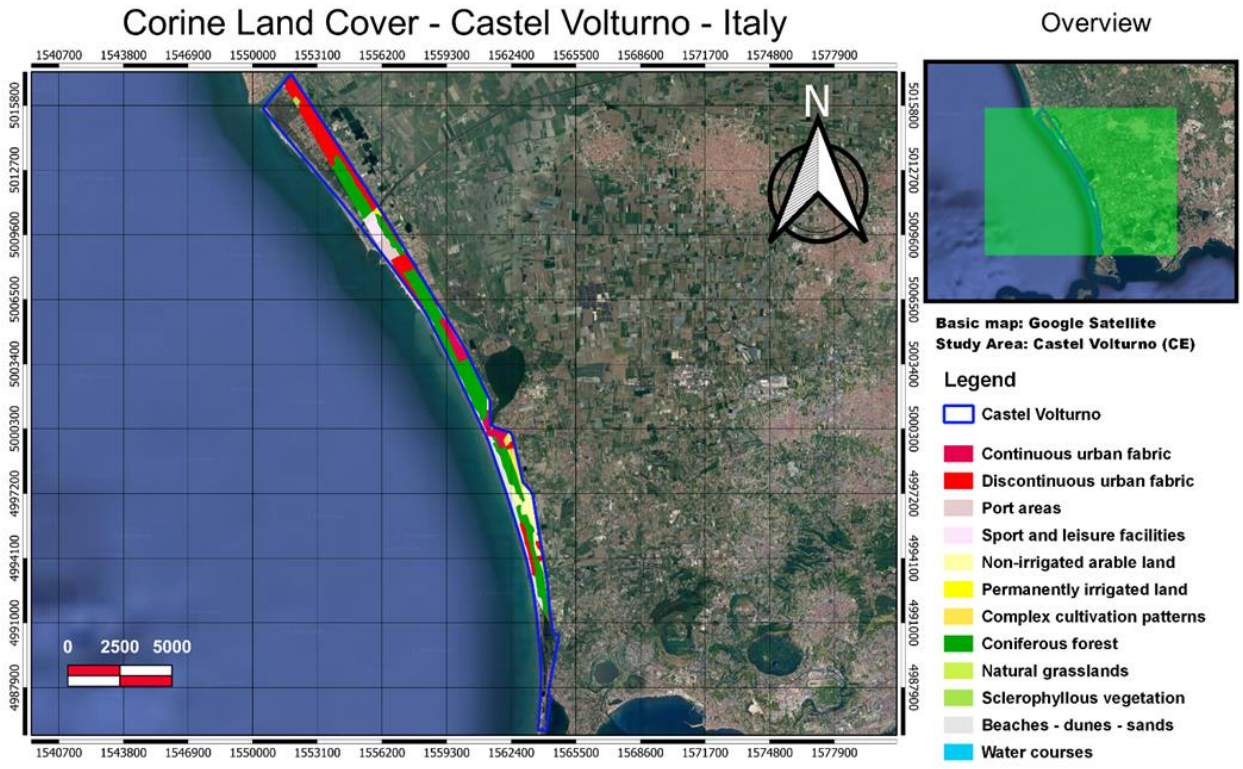

Figure 2. Castel Volturno Site occupies an area of around 268 hectares mainly characterized by the presence of woods holm oak, pine forests with Pinus pinea and a nucleus of retro-dunal hygrophilous vegetation. The Land use classes are from the Corine Land cover.

3.3.2. Castel Porziano

The Presidential Estate of Castel Porziano is about 25 km from the center of Rome and covers an area of 60 km2 (6039 hectares) consisting of humid areas behind the dunes and areas with low and high scrub with the typical evergreen and aromatic species. Most of the extension is occupied by the lowland hygrophilous wood (lowland wood linked to humid environments), characterized by the presence of evergreen and deciduous oaks and by more purely hygrophilous species, near the wetlands. The peculiarity of Castel Porziano is above all linked to the interpenetration of the oak grove typical of the Mediterranean climate and the oak grove typical of the continental climate. Among the evergreen oaks, the holm oak, the cork oak and the crenata oak, hybrid between turkey oak and cork oak, are widely diffused. Among the deciduous oaks we note the turkey oak, the English oak and the farnetto, while in the cooler wetlands we can find poplar, ossifillo ash, maple, hornbeam and oriental hornbeam typical of Mediterranean coastal environments. The wood (mixed plain), one of the most delicate ecosystems to be protected, extends for about 2300 hectares, the Mediterranean scrub environments, low and high, cover an area of about 500 hectares, the holm oak occupies an area of 261 hectares above all in the back dune area and the cork oak wood covers an area of about 460 hectares. The woods alternate with clearings and natural grasslands, forming plant associations of great environmental variety. The stone pine forests, created with artificial reforestation, extend for about 750 hectares with the purpose of consolidating the sandy dunes and protecting the rear dunes from sea winds,

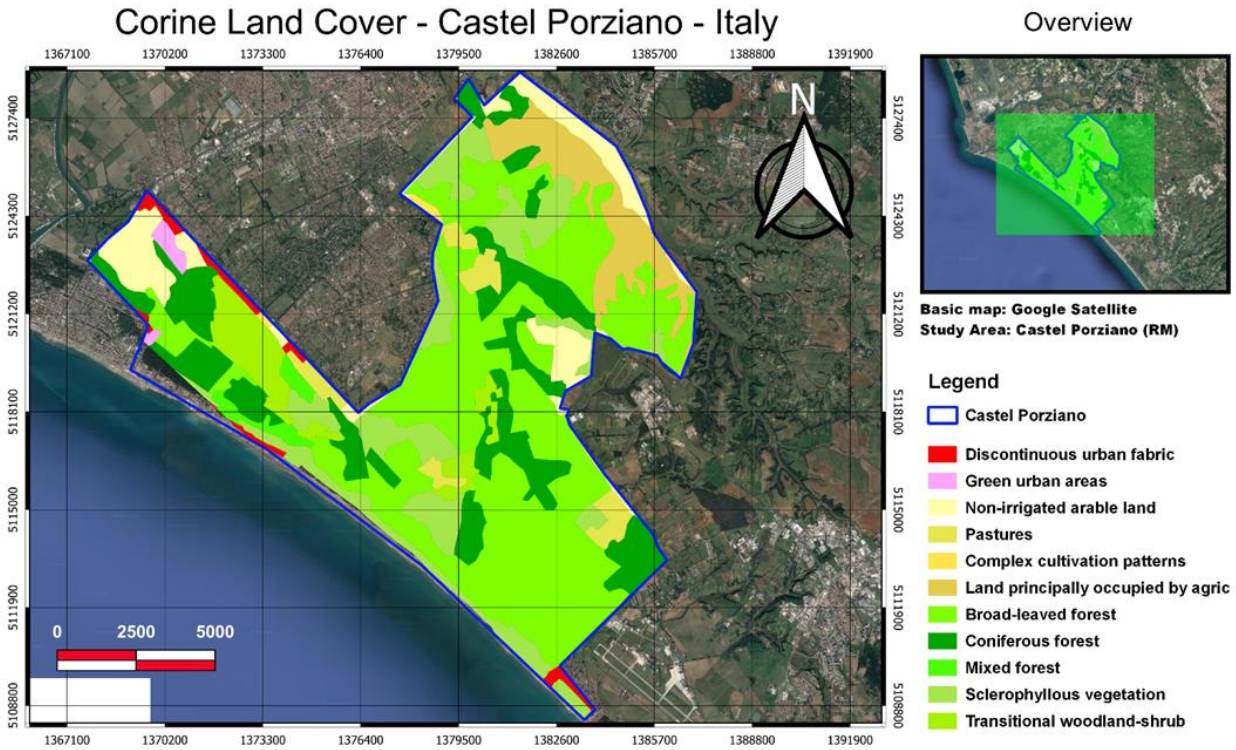

Figure 3. Castel Porziano site occupies an area of around 268 hectares mainly characterized by the presence of holm oak (261 hectares), cork oak wood (460 hectares), and stone pine forest (750 hectares) The woods alternate with clearings and natural grasslands. The land cover land use shown is from. The Land use classes are from the Corine Land cover

3.3.3. The Appia Antica Regional Park

The Appia Antica Regional Park with its 4,580 hectares is the largest urban protected area in Europe. A green wedge that runs from the city center towards the Castelli Romani. This green wedge, vast 4,580 hectares (following the last extension in October 2018) is characterized by different areas of interest: The Via Appia Antica and its adjacencies, the Caffarella Valley, the archaeological area of the Via Latina and of the Aqueducts, the Tenuta di Tormarancia, the Tenuta Farnesiana and then the areas of Divino Amore, Falcognana and Mugilla. The park is so vast that it affects three municipalities: that of Rome, Ciampino and Marino. The

Park today looks like a mosaic of different environments: large spaces intended for cultivation and extensive grazing are interrupted by uncultivated areas, residual wooded strips, where agricultural exploitation has not arrived or has long since ceased, ditches with the presence of riparian vegetation and some wet areas. These semi-natural environments and the agricultural context now represent the agro-ecosystem of the Roman countryside. A system of considerable naturalistic and scientific interest thanks to the presence of wildlife communities and plant associations, consistent with the ecological potential of the area. The Appia Antica Park is a substantial part of the Ecological Network of the city of Rome and is the most important protected peri-urban area of the Lazio Region.

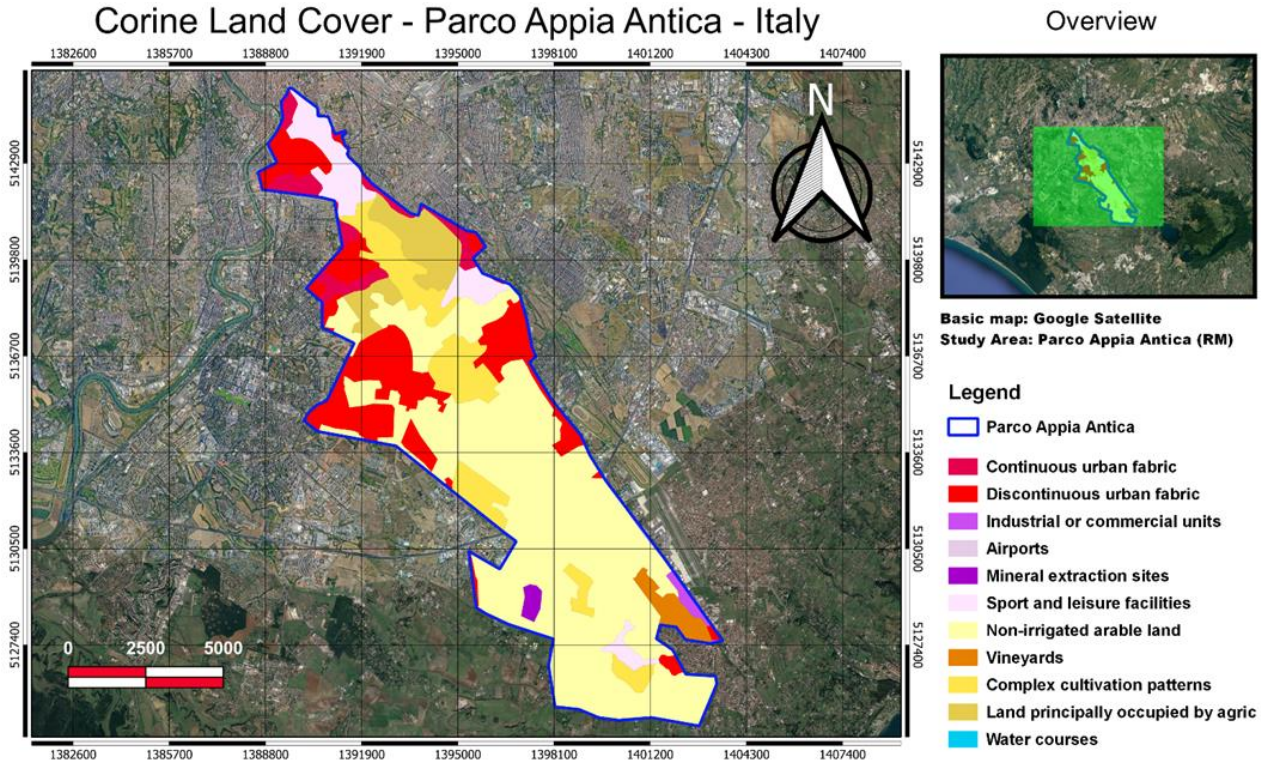

Figure 4. The Appia Park is around 4580 hectares. It is a mosaic of different environments: large spaces intended for cultivation and extensive grazing are interrupted by uncultivated areas, residual wooded strips, where agricultural exploitation has not arrived or has long since ceased, ditches with the presence of riparian vegetation and some wet areas. The Land use classes are from the Corine Land cover

3.4. Data

Four different satellite products available in the cloud storage of Google Earth Engine were selected because they are in a way related to the interactions between soil, water, atmosphere, and plants. For the purpose of this part of the study, MODIS products were chosen due to its global coverage and long duration of data acquisition. The description and characteristics of the studied datasets were mentioned below:

1. MOD16A2.006: Terra Net Evapotranspiration: It can be used to calculate regional water and energy balance, soil water status. With long-term ET data, the effects of changes in climate, land use, and ecosystems disturbances (e.g. wildfires and insect outbreaks) on regional water resources and land surface energy change can be quantified [Running et al., 2017]. MOD16 is a VI model based on the Penman-Monteith equation driven by MODIS data, and global meteorological reanalysis from the Modern-Era Retrospective analysis for Research and Applications (MERRA) [Mu et al., 2011]. ET can be estimated summing up soil evaporation (E_S), canopy evaporation (E_C), and canopy transpiration (T_C).

$$ET = E_S + E_C + T_C \quad (11)$$

The radiation arriving to the soil can be partitioned between canopy and soil surface using the fraction of photosynthetically active radiation (f_{PAR}) assuming that f_{PAR} and canopy cover (f_c) are equal. MOD16 also considers the pixel wet surface fraction (f_w), calculated as a function of relative humidity (RH; when RH is higher than 70%, $f_w = RH^4$), representing the fraction of vegetation and soil covered by water [Laipelt et al., 2021]. Estimations of E_S, E_C and T_S are given by Equations 12 to 14, respectively.

$$E_S = f_w \frac{\Delta A_s + \frac{(1-f_c)\rho_a C_P (e_S - e_a)}{r_a^s}}{\Delta + \gamma \frac{r_S^s}{r_a^s}} + RH^{\frac{(e_S - e_a)}{\beta_{sm}}} (1 - f_w) \frac{\Delta A_s + \frac{(1-f_c)\rho_a C_P (e_S - e_a)}{r_a^s}}{\Delta + \gamma \frac{r_S^s}{r_a^s}} \quad (12)$$

$$E_c = f_w \frac{\Delta A_s + \frac{f_c \rho_a C_P (e_S - e_a)}{r_a^{wc}}}{\Delta + \gamma \frac{r_S^s}{r_a^s}} \quad (13)$$

$$T_c = (1 - f_w) \frac{\Delta A_c + \frac{f_c \rho_a C_P (e_S - e_a)}{r_a^t}}{\Delta + \gamma (1 + \frac{r_S^t}{r_a^s})} \quad (14)$$

where Δ is the gradient of the saturation vapor pressure–temperature, As and Ac are the available energy to the soil and canopy, respectively, γ is the psychrometric constant, βsm is a parameter related to the soil moisture constraint, rss and rsa are the surface and aerodynamic resistance for the soil surface, rwcs and rwca are the surface and aerodynamic resistance for the wet canopy evaporation and rts and rta are the surface and aerodynamic resistance for the canopy transpiration (Laipelt et al., 2021).

2. MOD13Q1.006 Terra Vegetation Indices: MODIS vegetation indices are derived from atmospherically-corrected reflectance in the red, near-infrared, and blue wavebands; the normalized difference vegetation index (NDVI), and the enhanced vegetation index (EVI), which minimizes canopy-soil variations and improves sensitivity over dense vegetation conditions [Didan, 2015]:

$$NDVI = \frac{(\rho_{NIR} - \rho_{red})}{(\rho_{NIR} + \rho_{red})} \quad (15)$$

where ρ_{NIR}, ρ_{red} are the surface reflectance over the near-infrared (NIR) and red bands of MODIS. The NDVI is well correlated with vegetation cover, vegetation canopy, vegetation dynamics, biomass, and leaf area index and often considered as the vegetation proxy [Huete et al., 1999; Kumari et al., 2020; and Huete et al., 1993]. Similar to Normalized Difference Vegetation Index (NDVI), Landsat Enhanced Vegetation Index (EVI) can also quantify vegetation greenness in addition to correcting for some atmospheric conditions and canopy background noise (e.g. highly variable aerosol conditions, such as smoke from biomass burning) which makes it more sensitive in areas with dense vegetation [Kumari et al., 2021; and Huete et al., 1999]:

$$EVI = G(\frac{\rho_{NIR} - \rho_{red}}{\rho_{NIR} + C_1(\rho_{red}) - C_1(\rho_{blue}) + L}) \quad (16)$$

where G is a gain factor (G = 2.5), C1 = 6 and C2 = 7.5 are the aerosol coefficients. L adjustment factor to correct the effects induced by canopy background, and ρ values represents the surface reflectance which are atmospherically corrected.

3. MOD15A2H.006: Terra Leaf Area Index/FPAR: LAI is defined as the one-sided green leaf area per unit ground area and is used for calculating surface photosynthesis, evapotranspiration, and net primary production. It is calculated based on the fraction of photosynthetically active radiation absorbed by green vegetation [Myneni et al., 2015].

4. MOD11A2.006 Terra Land Surface Temperature and Emissivity: The Land Surface Temperature (LST) daily data are retrieved by the day/night algorithm where, daytime and nighttime LSTs and surface emissivities are retrieved from pairs of day and night MODIS observations in seven TIR bands [Wan et al., 2015].

Table 2. General description of datasets and bands used in this study available in the cloud storage of Google Earth Engine.

Collection Snippet	Dataset Availability	Bands						RESOLUTION	
		Name	Units	Min	Max	Scale	Description	Temporal [day]	Spatial [m]
ee.ImageCollection("MODIS/006/MOD16A2")	2001-2022	ET	kg/m^2/8day	-32767	32700	0.1	Total evapotranspiration	8	500
ee.ImageCollection("MODIS/006/MOD13Q1")	2000-2022	NDVI	[-]	-2000	10000	0.0001	Normalized Difference Vegetation Index	16	250
		EVI	[-]	-2000	10000	0.0001	Enhanced Vegetation Index	16	250
ee.ImageCollection("MODIS/006/MOD15A2H")	2000-2022	Lai_500m	sq. meter/ sq. meter	0	100	0.1	Leaf Area Index	8	500
ee.ImageCollection("MODIS/006/MOD11A2")	2000-2022	LST_Day_1km	Kelvin	7500	65535	0.02	Day land surface temperature	8	1000

The area-averaged time-series of studied parameters were extracted for the polygons representing the study regions (see figures 1) using the GEE JavaScript API for the study period of 2001-2020.

3.5. Results

We analyzed the 2000-2020 time variation of four vegetation indices: evapotranspiration (ET), normalized difference vegetation index (NDVI), leaf area index (LAI) and enhanced vegetation index (EVI).
First of all, the SSA was applied to each time series, and the value of the phase lag *M was selected* taking into account the sampling time of the series (8 days for ET and LAI; 16 days for EVI and NDVI). To detect at least the annual cycle, *M* was set as 45 for ET and LAI series, and as 24 for EVI and NDVI series, and, moreover, these values, well fit with the Khan and Poskitt's [24] criterion, varying the length of the data from 503 values (EVI and NDVI) to 965 (ET) and 1003 (LAI).
Figure 5 shows as an example, the application of the SSA to the ET time series of Appia. Before applying the SSA, the original time series was normalized. Figure 5a) shows the eigenvalue spectrum of the SSA decomposition; each eigenvalue corresponds to a reconstructed component and represents the fraction of the total variance of the original series explained by that component. Figure 5b) shows all the obtained reconstructed components, whose behaviour varies from oscillatory with amplitude modulation to apparently noisy.

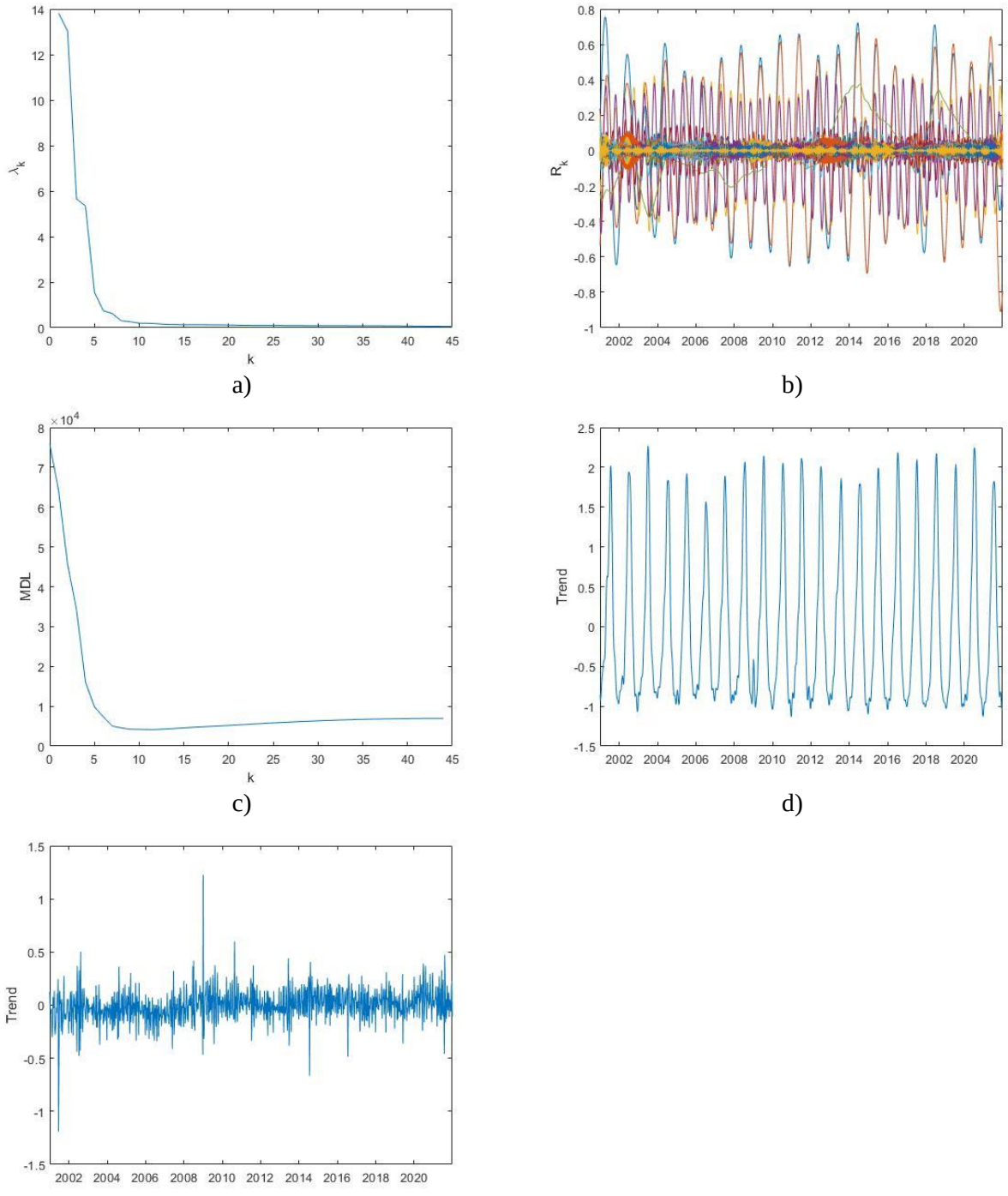

Figure 5. Application of the SSA to the ET series of Appia: a) eigenvalue spectrum; b) reconstructed components; c) MDL versus the number of components *k*; the minimum MDL is at k_{min}=11; d) trend; e) detrended series

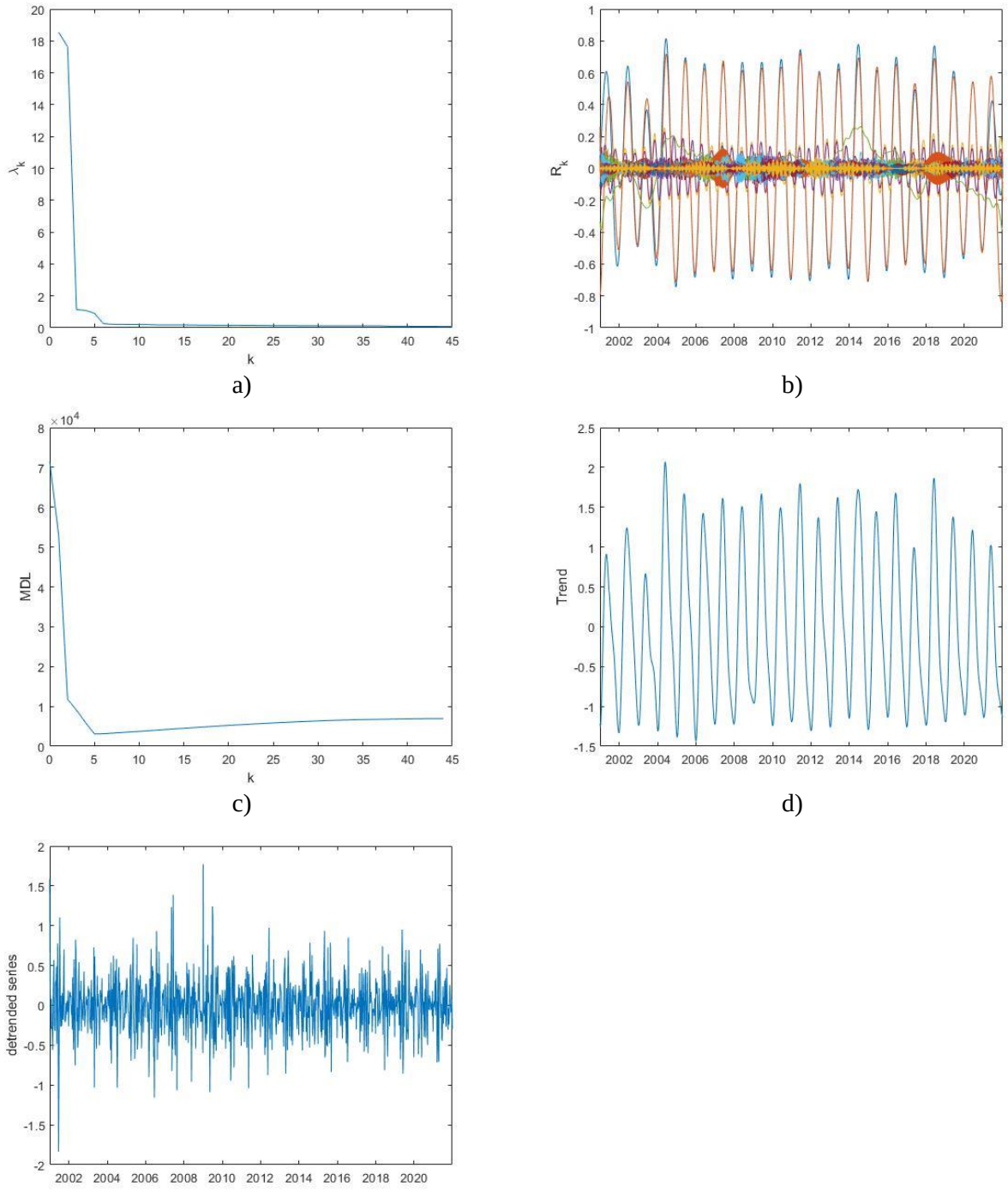

Figure 6. Application of the SSA to the ET series of Volturno: a) eigenvalue spectrum; b) reconstructed components; c) MDL versus the number of components *k*; the minimum MDL is at k_{min}=5; d) trend; e) de-trended series

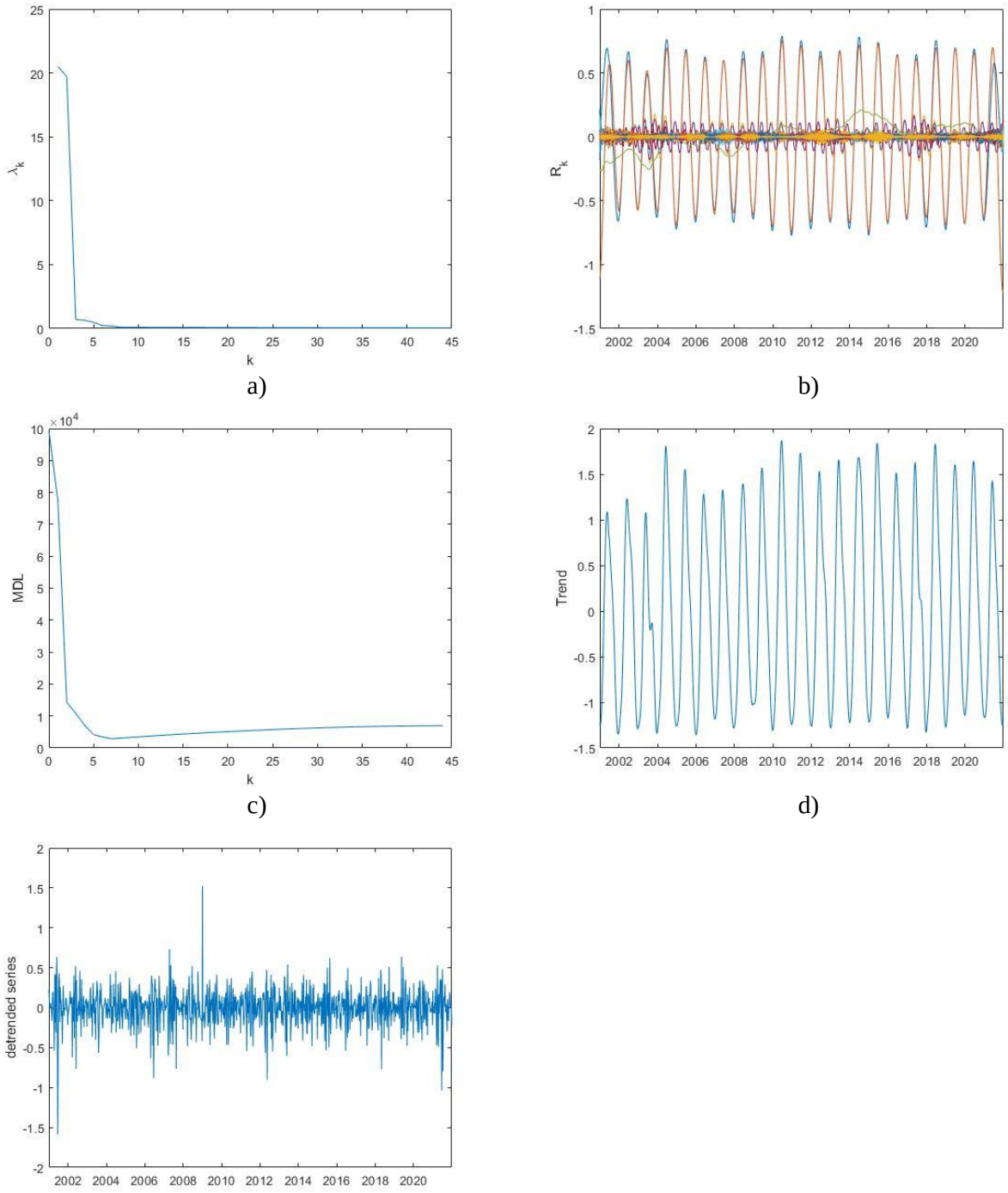

Figure 7. Application of the SSA to the ET series of Porziano: a) eigenvalue spectrum; b) reconstructed components; c) MDL versus the number of components *k*; the minimum MDL is at k_{min}=7; d) trend; e) de-trended series

Table 3. Values of minimum MDL.

	Castel Volturno	Castel Porziano	Appia
ET	5	7	11
EVI	5	10	10
LAI	5	7	9
NDVI	5	9	10

Applying the MDL criterion, the signal is separated into a trend and a de-trended series; the value of k_{min} corresponding to the minimum MDL represents the number of the first reconstructed components to sum up for obtaining the trend (Table 3). Applying this criterion to ET time series of Appia, the MDL curve is shown in Figure 5c), and the minimum MDL is at k_{min}=11; thus, the trend is obtained summing up the first 11 reconstructed components (Figure 5d) and the detrended series by subtracting the trend from the original normalized series (Figure 5e). Figure 6 and Figure 7 show, similarly to Figure 2, the application of SSA to the ET series of the other two sites, Castel Volturno and Castel Porziano.

The trend is characterized by an oscillatory behaviour that explains the seasonal cycles of the series, very likely linked with the meteo-climatic variability. The detrended series, although apparently noisy, would represent the inner time dynamics of the series that might be not influenced by external driving mechanisms. Table 3 shows for all the investigated indices the value of the minimum of MDL criterium.

Our aim is to characterize the time dynamics of inner vegetation of the investigated sites by using the Fisher-Shannon method. Thus, for each site we focused on the detrended series, since this represents the inner time variability of vegetation not influenced by external meteo-climatic factors.

Figure 8 shows the FSIP of ET (Figure 8a), EVI (Figure 8b), LAI (Figure 8c) and NDVI (Figure 8d). The FSIP indicates that Castel Volturno site is characterized by the highest Shannon entropy power and the lowest FIM that suggests a low level of order and organization of vegetation indices; Appia park, except for the ET, is characterized by the lowest Shannon entropy power and the lowest FIM that reveal a relative high level of order and organization of vegetation indices; Castel Porziano is generally characterized by an "intermediate" behaviour, since the vegetation indices, except ET, are located in the FSIP between Castel Volturno and Castel Porziano.

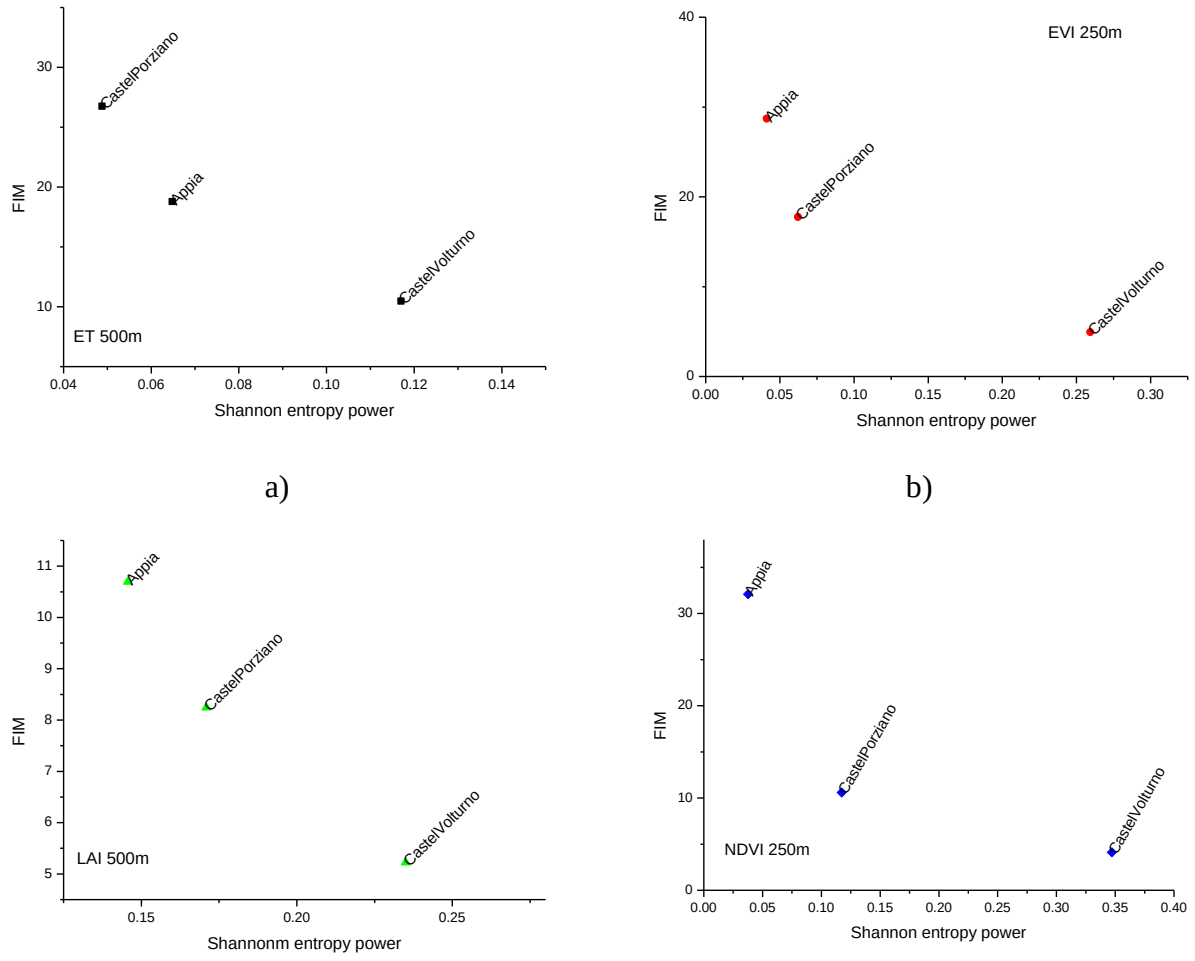

Figure 8. FSIP of ET (a), EVI (b), LAI (c) and NDVI (d).

3.6. Discussion

The potentiality of satellite systems for the monitoring of vegetation resources is widely recognized and nowadays the most recent ICT technological developments, the joint use of artificial intelligence and EO, along with the growing availability of information (and data also from free cloud as GEE) have opened new frontiers and application fields.
The use of EO-based indicators for the monitoring of vegetation is particularly relevant and recently the RS-derived data have been shown to be useful across many fields, but undoubtedly big earth observation data as satellite time series poses several challenges to face in order to transform data in useful and reliable information.
For the purpose of our investigation, the four vegetation indices (ET, NDVI, LAI and EVI) are different satellite products available in the cloud storage of Google Earth Engine and selected because they are related to the interactions between soil, water, atmosphere, and plants, while MODIS products were chosen due to its global coverage and long duration of data acquisition.
The analyses of satellite time series are generally quite complex and time consuming due to the amount of data, but they are expected to be suitable for the identification of both slow and fast changes as, for example, parasites or salinization, deforestation or wildfires, which adversely have been affecting CN during the last decades. Actually, the ability and effectiveness of change detection approaches and methods depends on the ability to account for the great variability exhibited by the seasonal variations (at seasonal and /or intra-annual scales) while identifying small multi-year trends and changes at diverse inter-annual time scales.
The methodological approach consisted of the following steps: decomposition of each satellite vegetation index through the SSA, detection of annual and seasonal cycles, separation between trend and de-trended series and application of the Fisher-Shannon method to the detrended series. In particular, this approach enabled us to perform the de-seasonality and, therefore, to split the stronger seasonal dynamics from the subtle inner time variability of the investigated signals. Identifying and extracting information related to the potential presence of small but significant trends or variations in vegetation is an important issue, and actually the effectiveness of change detection approaches depends on their ability to account for both the great variability exhibited by the seasonal variations but also the small multi-year changes that might be completely veiled by the seasonal dynamics.
Our study highlighted that the trend is characterized by an oscillatory behaviour that explains the seasonal cycles of the series, very likely linked with the meteo-climatic variability. Furthermore, the detrended series, whose variability our study has focused on, although apparently noisy, would represent the inner time dynamics of the series that might be not influenced by external driving mechanisms.
For Castel Volturno a low level of order and organization of the MODIS time series was observed during the whole investigated period. This behaviour denoted an anomalous vegetational dynamics that can be explained and attributable to the effect of attack by the parasite Toumeyella Parvicornis, which in the recent years adversely impacted the Pinus trees of the area dramatically damaging it.
The reliability of the analytical results obtained from the Fisher-Shannon approach was assessed by comparisons with field surveys and independent data analyses. In fact, the results obtained from the statistical analysis herein conducted, well fit with the results obtained from the processing of Sentinel 2 data jointly carried out by CNR and Carabinieri [35]) and shown in Figure 9; the grey pixels (in Figure 9d) indicate the areas affected by a decreasing trend (site degradation) as a resulting effect of the parasite attacking the pinus trees; the white pixels are related to areas involved in increasing trend, mainly linked to agricultural activities. Finally, Figure 9f and Figure 9g, acquired during the field survey, clearly provide evidence of the macroscopic effect of the Toumeyella Parvicornis on the pinus trees. An example of this behaviour, i.e. grey and white pixels, related to decreasing and increasing trends is shown in Figure 9e, where the blue and red lines depicted the maximum NDVI over time as obtained from Sentinel 2 data for the pixels indicated by the blue and red triangles respectively.

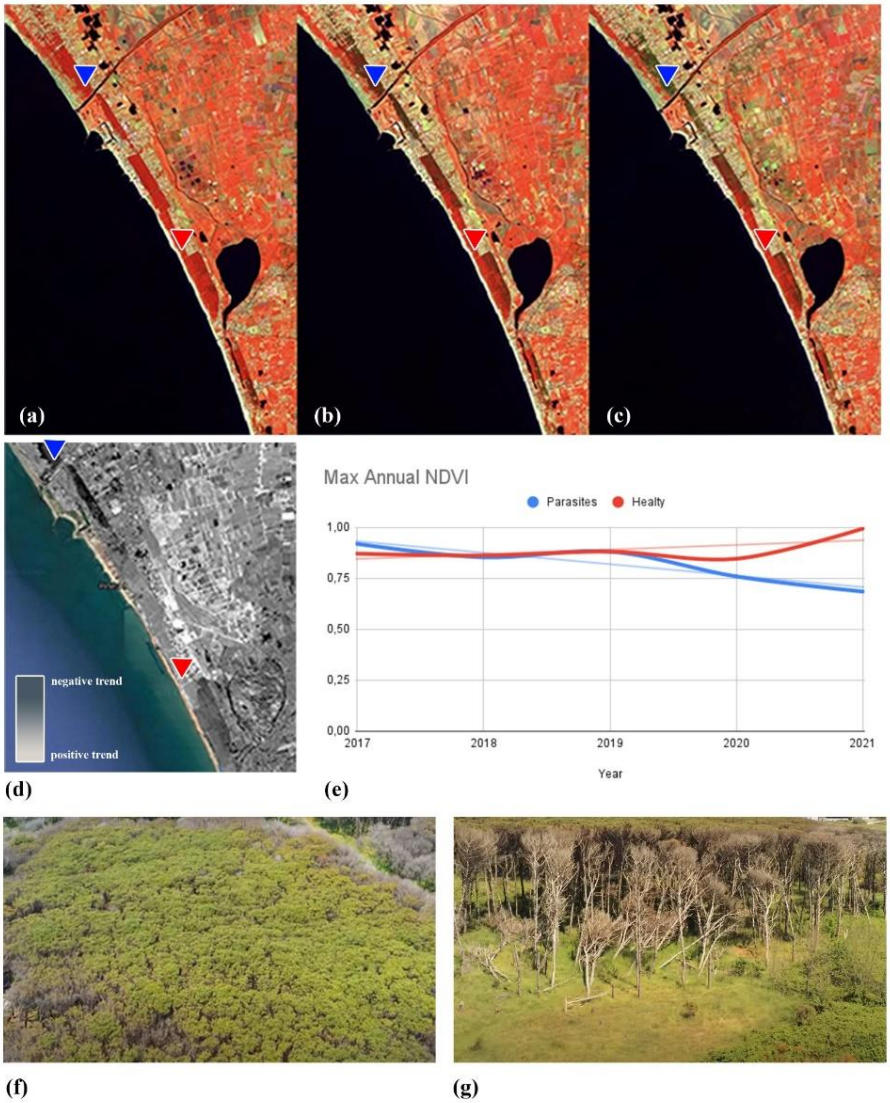

Figure 9. Outputs from the analysis jointly conducted by CNR and Carabinieri [35] based on Sentinel 2 NDVI time series. Details related to the results obtained by the independent analyses on Sentinel 2 (a,b,c) conducted by CNR and verified by Carabinieri by field surveys. The grey areas indicated the pixels affected by a decreasing trend (site degradation) for which an example is in Figure 6e. Field survey highlighted that this decreasing trend is mainly linked to the parasite attack which in the last 5 years strongly affected the pinus tree and dramatically damaged the area

The inner dynamic of vegetation of Appia Antica Park seems quite stable and this was confirmed by in-situ analysis. This site is mainly involved in and characterised by agricultural activities that were conducted systematically maintaining the same cultivation types for the whole period of our analysis [35]. The behaviour of the inner vegetation appears without anomalous dynamics, because the area was not involved in significant changes of vegetation status as well as of the land use and land cover as it can be seen from the Corine land cover updates (free available on line in the framework of the Copernicus initiative see for example, CORINE Land Cover — Copernicus Land Monitoring Service).

Castel Porziano, instead, presents FIM and Shannon Entropy values in the middle between those of Castel Volturno and Castel Porziano, except for the Evapotranspiration. Comparison with independent data sets [35] can confirm that from 2000 to 2020 the area was quite stable as it can be seen from Figure 10, where the Google Earth satellite pictures at higher resolution do not show particular changes in land cover.

Figure 10. Castel Porziano from GE high resolution images, which show that from 2000 to 2020 no significant changes occurred (Google Earth Pro courtesy)

3.7. Conclusion

The vegetation of three study areas from the Central (Appia ancient park and castel Porziano) to the Southern (Castel Volturno) part of Italy were analyzed. The study areas were peri-urban and specifically selected as key in improving environmental quality: in fact, they are rich in biodiversity and allow urban areas to be more sustainable, helping to combat climate change, and make cities more comfortable, as recently strongly emphasized by the pandemic emergency.

Thus, for each site we focused on the detrended series, since this represents the inner time variability of vegetation not influenced by external meteo-climatic factors.

Results of our analyses highlighted that the (i) trend is characterized by an oscillatory behaviour that explains the seasonal cycles of the series, very likely linked with the meteo-climatic variability, (ii) detrended series, although apparently noisy, would represent the inner time dynamics of the series that might be not influenced by external driving mechanisms

Among the sites investigated, Castel Volturno was characterized by the highest Shannon entropy power and the lowest FIM that indicate a low level of order and organization of the vegetation indices for this site. Independ analyses and field survey highlighted that Castel Volturno is strongly affected by a parasite, the Toumeyella Parvicornis, which has been provoking a dramatic damage to the Pinus trees in the last years.

Our results could contribute to the definition of methods suitable for an early diagnosis of deterioration trends, and create operational tools for multi-scale, multi-sensor, multi-temporal monitoring of bio-physical parameters relating to the state of vegetation.

3.8. References

1. Filipponi, F., Valentini, E., Nguyen Xuan, A., Guerra, C. A., Wolf, F., Andrzejak, M., & Taramelli, A. (2018). Global MODIS fraction of green vegetation cover for monitoring abrupt and gradual vegetation changes. Remote Sensing, 10(4), 653.
2. Bastiaanssen, W.G.M., Noordman, H., Pelgrum, G., Thoreson, B.P., Allen, R.G., 2005. SEBAL model with remotely sensed data to improve water resources management under actual field conditions. J. Irrig. Drain. Eng. 131, 85–93.
3. Senay, G.B., Budde, M.E., Verdin, J.P., 2011. Enhancing the simplified surface energy balance (SSEB) approach for estimating landscape ET: validation with the METRIC model. Agric. Water Manage. 98, 606–618.
4. Tadesse, T., Senay, G. B., Berhan, G., Regassa, T., & Beyene, S. (2015). Evaluating a satellite-based seasonal evapotranspiration product and identifying its relationship with other satellite-derived products and crop yield: A case study for Ethiopia. International Journal of Applied Earth Observation and Geoinformation, 40, 39-54.
5. Abbasi, N., Nouri, H., Didan, K., Barreto-Muñoz, A., Chavoshi Borujeni, S., Salemi, H., ... & Nagler, P. (2021). Estimating Actual Evapotranspiration over Croplands Using Vegetation Index Methods and Dynamic Harvested Area. Remote Sensing, 13(24), 5167.
6. Senay, G.B., Bohms, S., Singh, R.K., Gowda, P.H., Velpuri, N.M., Alemu, H., Verdin, J.P., 2013. Operational evapotranspiration mapping using remote sensing and weather datasets: a new parameterization for the SSEB approach. J. Am. Water Res. Assoc. 49 (3), 577–591, http://dx.doi.org/10.1111/jawr.12057.
7. Laipelt, L., Kayser, R. H. B., Fleischmann, A. S., Ruhoff, A., Bastiaanssen, W., Erickson, T. A., & Melton, F. (2021). Long-term monitoring of evapotranspiration using the SEBAL algorithm and Google Earth Engine cloud computing. ISPRS Journal of Photogrammetry and Remote Sensing, 178, 81-96.
8. Fisher, J. B., Tu, K. P., & Baldocchi, D. D. (2008). Global estimates of the land–atmosphere water flux based on monthly AVHRR and ISLSCP-II data, validated at 16 FLUXNET sites. Remote Sensing of Environment, 112(3), 901-919.
9. Mu, Q., Zhao, M., Running, S.W., 2011. Improvements to a MODIS global terrestrial evapotranspiration algorithm. Remote Sens. Environ. 115, 1781–1800 https://doi.org/https://doi.org/10.1016/j.rse.2011.02.019.
10. Martens, B., Miralles, D.G., Lievens, H., van der Schalie, R., de Jeu, R.A.M., Fern´andez-Prieto, D., Beck, H.E., Dorigo, W.A., Verhoest, N.E.C., 2017. GLEAM v3: satellitebased land evaporation and root-zone soil moisture. Geosci. Model Dev. 10, 1903–1925. https://doi.org/10.5194/gmd-10-1903-2017.
11. Bastiaanssen, W.G.M., Menenti, M., Feddes, R.A., Holtslag, A.A.M., 1998. A remote sensing surface energy balance algorithm for land (SEBAL): 1. Formulation. J. Hydrol. 212–213, 198–212. https://doi.org/10.1016/S0022-1694(98)00253-4.
12. Allen, R.G., Tasumi, M., Trezza, R., 2007. Satellite-based energy balance for mapping evapotranspiration with internalized calibration (METRIC)—model. J. Irrig. Drain. Eng. 133, 380–394. https://doi.org/10.1061/(ASCE)0733-9437(2007)133:4(380).
13. Su, B., 1988. The surface energy balance system (SEBS) for estimation of turbulent heat fluxes. Hydrol. Earth Syst. Sci. 6 https://doi.org/10.5194/hess-6-85-2002.
14. Palmer, W.C., 1965. Meteorological drought. In: US Weather Bureau Research Paper. 45.
15. Zhang, H., Song, J., Wang, G., Wu, X., & Li, J. (2021). Spatiotemporal characteristic and forecast of drought in northern Xinjiang, China. Ecological Indicators, 127, 107712.
16. Aghelpour, P., Mohammadi, B., Mehdizadeh, S. et al. A novel hybrid dragonfly optimization algorithm for agricultural drought prediction. Stoch Environ Res Risk Assess 35, 2459–2477 (2021). https://doi.org/10.1007/s00477-021-02011-2
17. Liu, Y., Zhang, X., Song, H., Cai, Q., Li, Q., Zhao, B., ... & Mei, R. (2017). Tree-ring-width-based PDSI reconstruction for central Inner Mongolia, China over the past 333 years. Climate Dynamics, 48(3), 867-879.
18. Zhang, B., Wu, P., Zhao, X., Wang, Y., Gao, X., & Cao, X. (2013). A drought hazard assessment index based on the VIC–PDSI model and its application on the Loess Plateau, China. Theoretical and applied climatology, 114(1), 125-138.
19. Jacobi, J., Perrone, D., Duncan, L. L., & Hornberger, G. (2013). A tool for calculating the Palmer drought indices. Water Resources Research, 49(9), 6086-6089.
20. Alley, W. M. (1984). The Palmer drought severity index: limitations and assumptions. Journal of Applied Meteorology and Climatology, 23(7), 1100-1109.
21. Vautard R, Ghil M (1989) Singular spectrum analysis in nonlinear dynamics, with applications to paleoclimatic time series. Physica D 35:395–424
22. Hassani H (2007) Singular Spectrum Analysis: Methodology and Comparison. Journal of Data Science 5:239-257
23. Schoellhamer D (2001) Singular spectrum analysis for time series with missing data. Geophysical Research Letters 28:3187-3190
24. Khan M., Poskitt DS (2010) Description Length Based Signal Detection in singular Spectrum Analysis. Monash Econometrics and Business Statistics Working Papers 13/10, Monash University, Department of Econometrics and Business Statistics
25. Wax M, Kailath T (1985), Detection of signals by information theoretic criteria. IEEE Transactions on Acoustics Speech and Signal Processing, vol. ASSP-33, 387-392
26. Fisher, R.A. Theory of Statistical Estimation. Math. Proc. Camb. Philos. Soc. 1925, 22, 700–725, doi:10.1017/S0305004100009580.

27. Shannon, C.E. A Mathematical Theory of Communication. Bell Syst. Tech. J. 1948, 27, 379–423, doi:10.1002/j.1538-7305.1948.tb01338.x.
28. Sen, K.D.; Antolín, J.; Angulo, J.C. Fisher-Shannon Analysis of Ionization Processes and Isoelectronic Series. Phys. Rev. A 2007, 76, 032502, doi:10.1103/PhysRevA.76.032502.
29. Telesca, L.; Lovallo, M. Fisher-Shannon Analysis of Wind Records. Int. J. Energy Stat. 2013, 01, 281–290, doi:10.1142/S2335680413500208.
30. Janicki, A.; Weron, A. Simulation and Chaotic Behavior of Alpha-Stable Stochastic Processes; Chapman & Hall/CRC Pure and Applied Mathematics; CRC Press, 1993; ISBN 978-0-8247-8882-7.
31. Devroye, L. A Course in Density Estimation; Progress in Probability; Birkhäuser Boston Inc.: Cambridge, MA, USA, 1987; ISBN 978-0-8176-3365-3.
32. Troudi, M.; Alimi, A.M.; Saoudi, S. Analytical Plug-In Method for Kernel Density Estimator Applied to Genetic Neutrality Study. EURASIP J. Adv. Signal Process. 2008, 2008, 739082, doi:10.1155/2008/739082.
33. Raykar, V.C.; Duraiswami, R. Fast optimal bandwidth selection for kernel density estimation. In Proceedings of the 2006 SIAM International Conference on Data Mining; Proceedings; Society for Industrial and Applied Mathematics, 2006; pp. 524–528 ISBN 978-0-89871-611-5.
34. Vignat, C.; Bercher, J.-F. Analysis of Signals in the Fisher–Shannon Information Plane. Phys. Lett. A 2003, 312, 27–33, doi:10.1016/S0375-9601(03)00570-X.
35. Lasaponara R., Abate N., Fattore C., Aromando A., Cardettini G., Project report 2021 -0002058/2021 del 15/12/2021 [Accordo di collaborazione tra il CUFA e il CNR –IMAA per attività di supporto alla progettazione, realizzazione e gestione del Programma SMART FOREST MONITORING - Monitoraggio delle anomalie multi spettrali delle foreste italiane tramite remote sensing da piattaforme satellitari nell'ambito del "green New Deal e Transizione ecologica del Paese" relativamente alle attività di mon nitoraggio forestale e ambientale

List of publications

International Journals

---

1. Telesca, L., Aromando, A., **Faridani, F.,** Lovallo, M., Cardettini, G., Abate, N., ... & Lasaponara, R. (**2022**). Exploring Long-Term Anomalies in the Vegetation Cover of Peri-Urban Parks Using the Fisher-Shannon Method. Entropy, 24(12), 1784.
2. Paridad, P., Dal Sasso, S.F., Pizarro, A., Mita, L., Fiorentino, M., Margiotta, M.R., **Faridani, F.,** Farid, A. and Manfreda, S. (**2022**). Estimation of soil moisture from UAS platforms using RGB and thermal imaging sensors in arid and semi-arid regions. Acta Hortic. 1335, 339-348.DOI: 10.17660/ActaHortic.2022.1335.42
3. Farokhi, M., **Faridani, F.,** Lasaponara, R., Ansari, H., & Faridhosseini, A. (**2021**). Enhanced Estimation of Root Zone Soil Moisture at 1 km Resolution Using SMAR Model and MODIS-Based Downscaled AMSR2 Soil Moisture Data. Sensors, 21(15), 5211.
4. Fattore, C., Abate, N., **Faridani, F.,** Masini, N., & Lasaponara, R. (**2021**). Google earth engine as multi-sensor open-source tool for supporting the preservation of archaeological areas: the case study of flood and fire mapping in Metaponto, Italy. Sensors, 21(5), 1791.
5. **Faridani, F.,** Bakhtiari, S., Faridhosseini, A., Gibson, M. J., Farmani, R., & Lasaponara, R. (**2020**). Estimating Flood Characteristics Using Geomorphologic Flood Index with Regards to Rainfall Intensity-Duration-Frequency-Area Curves and CADDIES-2D Model in Three Iranian Basins. Sustainability, 12(18), 7371.

International Conferences/Workshops with Peer Review

---

1. Telesca, L., Lasaponara, R., **Faridani, F.,** Abate, N., & Lovallo, M. (2023). Informational Analysis of MODIS Satellite Evapotranspiration Data of Vegetation Cover: A Method to Reveal the Presence of Plant Diseases. The Eighth International Conference on Advances in Signal, Image and Video Processing (SIGNAL 2023), 13-17 March 2023, Barcelona, Spain.

Abstract

Global warming, as the biggest manifestation of climate change, has changed the distribution of water in the hydrological cycle by increasing the evapotranspiration rate resulting in anthropogenic and natural hazards adversely affecting modern and past human properties and heritage in different parts of the world. The comprehension of environmental issues is critical for ensuring our existence on Earth and environmental sustainability. Environmental modeling can be described as a simplified form of a real system that enhances our knowledge of how a system operates. Such models represent the functioning of various processes of the environment, such as processes related to the atmosphere, hydrology, land surface, and vegetation. The environmental models can be applied on a wide range of spatiotemporal scales (i.e. from local to global and from daily to decadal levels); and they can employ various types of models (e.g. process-driven, empirical or data-driven, deterministic, stochastic, etc.). Satellite remote sensing and Earth Observation techniques can be utilized as a powerful tool for flood mapping and monitoring. By increasing the number of satellites orbiting around the Earth, the spatial and temporal coverage of environmental phenomenon on the planet has in-creased. However, handling such a massive amount of data was a challenge for researchers in terms of data curation and pre-processing as well as required computational power. The advent of cloud computing platforms has eliminated such steps and created a great opportunity for rapid response to environmental crises. The purpose of this study was to gather state-of-the-art remote sensing and/or earth observation techniques and to further the knowledge concerned with any aspect of the use of remote sensing and/or big data in the field of geospatial analysis. In order to achieve the goals of this study, some of the water-related climate-change phenomena were studied via different mathematical, statistical, geomorphological and physical models using different satellite and in-situ data on different centralized and decentralized computational platforms. The structure of this study was divided into three chapters with their own materials, methodologies and results including: (1) flood monitoring; (2) soil water balance modeling; and (3) vegetation monitoring. The results of this part of the study can be summarize in: 1) presenting innovative procedures for fast and semi-automatic flood mapping and monitoring based on geomorphic methods, change detection techniques and remote sensing data; 2) modeling soil moisture and water balance components in the root zone layer using in-situ, drone and satellite data; incorporating downscaling techniques; 3) combining statistical methods with the remote sensing data for detecting inner anomalies in the vegetation covers such as pest emergence; 4) stablishing and disseminating the use of cloud computation platforms such as Google Earth Engine in order to eliminate the unnecessary steps for data curation and pre-processing as well as required computational power to handle the massive amount of RS data. As a conclusion, this study resulted in provision of useful information and methodologies for setting up strategies to mitigate damage and support the preservation of areas and landscape rich in cultural and natural heritage.

Keywords: Remote sensing, Earth observation, Environmental modeling, Cloud computation, hazard monitoring.

UNIVERSITÀ DEGLI STUDI DELLA BASILICATA
MATERA

Dottorato di Ricerca
In

"Cities and Landscapes: Architecture, Archeology, Cultural Heritage, History and Resources"

Ciclo XXXV

TITOLO DELLA TESI

"Novel Satellite-Based Methodologies for Multi-Sensor and Multi-Scale Environmental Monitoring to Preseve Natural Capital"

Settore Scientifico Disciplinare: "*ICAR/03"*

Coordinatore del dottorato
Prof.ssa Antonella Guida

Dottorato
Dott. Farid Faridani Bardaskan

Tutor
Prof.ssa Rosa Lasaponara

A.A. 2022/2023